COMPARISON OF OPTICAL AND MICROWAVE SPACE BORNE SENSORS FOR MAPPING OF TROPICAL FOREST FRAGMENTATION IN BOLIVIA

Thesis submitted by

Abhishek Dhungel

(BE, Kathmandu University)

October 2018

For the degree of Master of Science in GIS

In the College of Science and Engineering, Faculty of Science and Engineering

Flinders University, Adelaide, South Australia

i

DECLARATION

I certify that this thesis does not incorporate without acknowledgment any material previously submitted for a degree or diploma in any university; and that to the best of my knowledge and belief, does not contain any material previously published or written by another person except where due reference is made in the text.

Signature Abhishek Digitally signed by Abhishek
Date: 2018.10.21 09:53:06
+10'30'   **Date**____ 15th October, 2018

ABSTRACT

This research was performed to answer the research question: Which sensors, optical and RADAR, provide better accuracy in mapping tropical forest fragmentation? The potential significance of this research was to understand the capabilities and importance of satellite remote sensors for monitoring forest clearance in Bolivia. Over large areas satellite remote sensing potentially provides a cost-effective solution for this mapping. However, remote sensing using optical (visible and infrared) imagery in tropical regions, such as Bolivia, is often hampered by the existence of clouds. This research focuses on mapping deforestation in the low land tropical area of Bolivia using satellite RADAR, which penetrates cloud, and compares results with those from optical remote sensing, to provide information for analysis of tropical forest fragmentation.

The primary data acquired was the ALOS-1 PALSAR imagery from 2007 obtained from Alaskan Satellite Facility and Landsat 5 TM imagery from 2007 from USGS Earth Explorer. The obtained Landsat imagery was initially subjected to haze removal where maximum amount of haze was reduced. The obtained raw RADAR data was a single look complex (SLC) image with dual polarization (HH + HV). The data were complex data on the slant range coordinate which was later converted to ground range using ortho-rectification where the geometry of SLC image was corrected. Once the geometry of image was corrected, it was subjected to speckle suppression while attempting to preserve the radiometric and spatial resolution of the initial image. Geometric correction was further performed to geo-correct the RADAR imagery.

Classification of both optical and RADAR imagery was performed using pixel based classification via maximum likelihood classifier and object oriented classification via machine learning. Post classification operations were performed on both the classified images for further smoothing. Accuracy assessment was later performed using the ground truth collected during field work which resulted in the overall accuracy of 78.4% for optical and 67.98% for RADAR imagery.

DEDICATION

I wish to dedicate this work to my parents without whom I would not be here today. They have dedicated their life to give me a platform where I can stand in front of everyone and make them proud for believing me all these years.

ACKNOWLEDGEMENT

I would first like to thank my thesis supervisors Professor Andrew Millington and Professor David Bruce of the College of Science and Engineering at Flinders University. The door to their office was always open whenever I ran into a trouble spot or had a question about my research or writing. They consistently allowed this paper to be my own work but steered me in the right direction whenever they thought I needed it.

I would also like to thank Mr Rob Keane for his tremendous help with GIS processing whenever I felt lost within my work with GIS.

I would also like to acknowledge my colleagues Er. Sameep Bimal Chhetri, Mr. Dorji Tashi and Er. Shashwat Kafle for their constant motivation and their unmeasurable help throughout my thesis.

Finally, I must express my very profound gratitude to my parents and to my girlfriend for providing me with unfailing support and continuous encouragement throughout my years of study and through the process of researching and writing this thesis. This accomplishment would not have been possible without them. Thank you.

Author

Abhishek Dhungel

ACRONYMS AND ABBREVIATIONS

AGB   Above Ground Biomass

ALOS   Advanced Land Observation Satellite

AOI   Area of Interest

ASF   Alaskan Satellite Facility

DEM   Digital Elevation Model

DN   Digital Number

DOS   Dark Object Subtraction

EE   Earth Explorer

EOSAT   Earth Observation Satellite Company

ERDAS   Earth Resource Development Assessment System

ERTS   Earth Resources Technology Satellite

ETM+   Enhanced Thematic Mapper

FBS   Fine Beam Single polarization

FBD   Fine Beam Double polarization

FLS   Full Lambda Schedule

GEC   Geocoded Ellipsoid Corrected

GFW   Global Forest Watch

GIS   Geographic Information System

GPS   Global Positioning System

GRD   Ground Range Detected

GSD	Ground Sampling Distance
HH	Horizontal-Horizontal
HV	Horizontal-Vertical
IPCC	Intergovernmental Panel on Climate Change
JAXA	Japan Aerospace Exploration Agency
JM	Jefferies-Matusita
MAP	Maximum a Posterior
ML	Machine Learning
MLC	Maximum Likelihood Classification
MODIS	Moderate Resolution Imaging Spectroradiometer
MSS	Multispectral Scanner
NIR	Near-Infrared
NB	Naïve Bayes
OOC	Object Oriented Classification
OLI	Operational Land Imager
OOC	Object Oriented Classification
PALSAR	Phased Array type L-Band Synthetic Aperture Radar
QA	Quality Assurance
RADAR	Radio Detection and Ranging
RBV	Return Beam Vidicon
RF	Random Forest
RMS	Root Mean Square
RS	Remote Sensing

SAR	Synthetic Aperture Radar
SLC	Single Look Complex
SLAR	Side Looking Airborne Radar
SVM	Support Vector Machine
TM	Thematic Mapper
TOA	Top of Atmosphere
TCT	Tasselled Cap Transformation
USGS	United Sates Geological Survey
UTM	Universal Transverse Mercator
VV	Vertical-Vertical
VH	Vertical-Horizontal
WWF	World Wildlife Federation

TABLE OF CONTENTS

LIST OF FIGURES

LIST OF TABLES

CHAPTER ONE

INTRODUCTION

1.1 Overview

Deforestation is a major environment problem which has not been addressed effectively (Fearnside, 2005). In order to meet the demands and the needs of growing populations, the majority of the forest have been exploited throughout the world. Bolivia is no exception, with the migration of people from the highlands to the low land tropics and the international demand for cash crops, it is also one of the major regions in the world that is facing deforestation at a larger scale (Pacheco, 2002). Deforestation in the tropical and temperate region is an ongoing occurrence throughout history and present times (Tucker and Richards, 1983). Global estimates for the rate of tropical deforestation ranges from 69,000 km^2 in the 1980 (Lanly, 1981) to 100,000 to 165,000km^2 in the late 1980s. Such high rates of tropical deforestation are a major contributor to the carbon cycle as well as has profound impacts on the biological diversity both on a local as well as global scale (Fearnside, 2005).

The deforestation in the area studied, the Bolivian Chapare, started in the vicinity of Chipiriri and Tunari-Chimore in 1950s with the migration of people from the Andes to the lowland tropics to fulfil the demands of an embryonic agro-industrial sector (Skole and Tucker, 1993). This movement led to clearance of many types of tropical forest for agriculture. As the population increased so too did the demand for the development of roads which, in turn, gave rise to more forest removal and subsequent fragmentation (Pacheco, 2006). Mapping this forest clearance is an important part of understanding this type of environmental change and how it is affected by both government policy and human needs (Laurance and Bierregaard, 1997). Over large areas satellite remote sensing potentially provides a cost-effective solution for this type of mapping (Goetz et al., 2009). However, remote sensing using optical (visible and infrared) imagery in tropical regions such as Bolivia is often hampered by the existence of clouds (Pohl and Van Genderen, 1998). This research focuses on mapping deforestation in lowland tropical Bolivia using satellite RADAR, which penetrates cloud, and compares results with those from optical remote sensing, to provide a comparison of different types of information for analysis of tropical forest fragmentation.

Numerous research studies have been conducted focusing on the fragmentation on the tropical regions using various techniques and algorithms (Lambin, 1999, Pacheco, 2002, Roy et al., 2014, Steininger et al., 2001). The use and application of GIS and remote sensing have been reviewed by Millington, Velez-Liendo et al., (2003) to quantify and map the forest fragmentation in the tropical low lands of Bolivia where the examination of the relationship between various spatial resolutions of satellite images and landscape metrics was undertaken. Similarly, (Margono et al., 2012) mapped and monitored the pattern of deforestation and degradation in Sumatra (Indonesia) using multi-temporal Landsat data from years 1990 to 2010 and highlighted that the use of GIS and remote sensing can deliver significant information with high quality output. Satellite multi-temporal datasets have been found to be widely used for tropical deforestation quantification in the spatial context (Skole and Tucker, 1993, Taubert et al., 2018). Space borne remote sensing has proved its usefulness when monitoring the dynamic features in the environment and making it a lot easier to assess the changes in the shapes and sizes of the fragmenting forests (Jha et al., 2005).

1.2 Overview of Bolivia
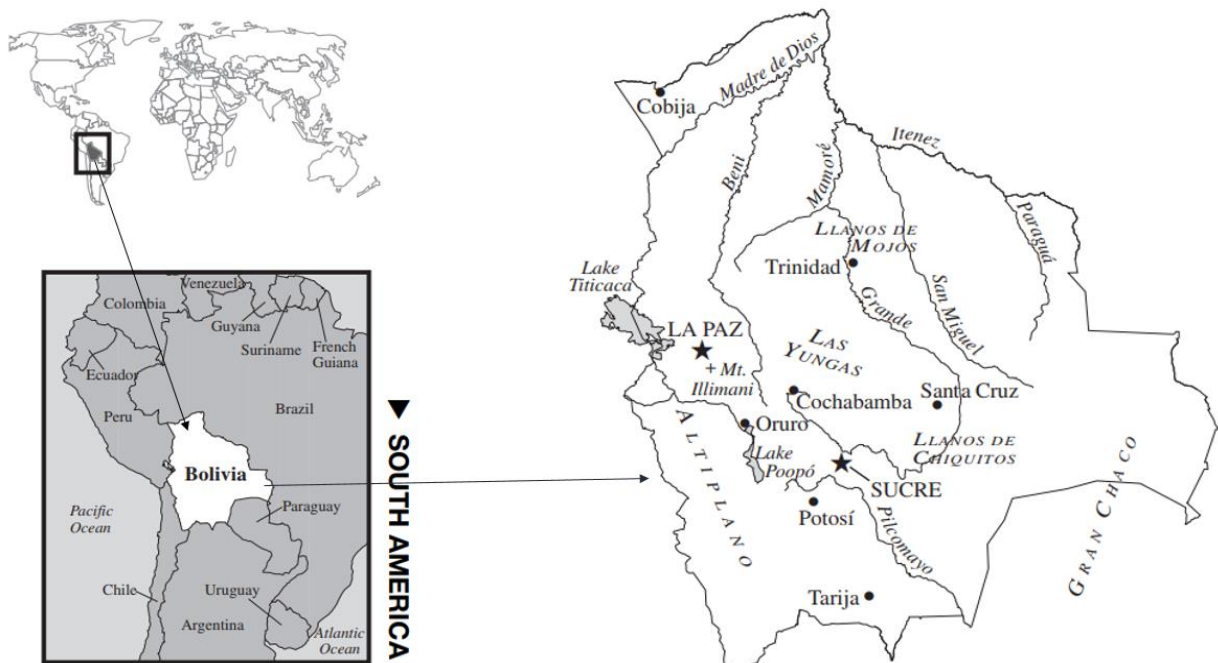
Figure 1: Geographical Location of Bolivia
(Source: http://www.uvm.edu/~iwd/Bolivia.pdf)

2

Bolivia is a land-locked country that occupies a total area of 1,098,000 km^2 in the centre of South America (Myers et al., 2000). It covers five different geographical regions (Figure 1): the Altiplano, which lies in the south-west part of Bolivia and it is the high rimmed mountain that is dominated by cold and dry climate; the Yungas, which lies in the western part of Bolivia and are valleys at medium elevation; La Paz and Cochabamba are the heart of Bolivia which lie in the central part of the country and comprise of agriculturally-dominated highland valleys; the Gran Chaco is a huge subtropical lowland that shares the boundary with Argentina and Paraguay in the southern region of Bolivia; and the Llanos is the lowland tropical ecoregion in the eastern and north-east region of Bolivia (Fearnside, 2005, Pacheco, 2006). The Llanos has a high potential for cattle ranching since grassland is abundant in these areas (Stearman, 1985). There are about 500,000 km^2 of forest and woodlands in Bolivia, of which about 400,000 km^2 is lowland tropical forest (Steininger et al., 2001).

Bolivia has two main seasons. Summer which extends from November until April is the rainy season, and winter which starts in June and lasts until September is dry (Steininger et al., 2001). The annual rainfall varies from 3000 to around 6000 mm, the latter totals occur in central Chapare (Fearnside, 2005, Tejada et al., 2016).

Bolivia has two different capital cities: La Paz and Sucre (Steininger et al., 2001). La Paz is considered to be the major capital since it has presidential residency and is the commercial capital, whereas Sucre holds the highest courts of Bolivia (Fearnside, 2005, Pacheco, 2006). The average annual temperature in La Paz is 18°C. There are 8.7 million residents in Bolivia among which the majority of people living in the areas of Andean valleys and Altiplano (Steininger et al., 2001). It has a population growth rate of 1.6 percent annually, with about a third residing in rural areas (Tejada et al., 2016).

1.3 Study Area
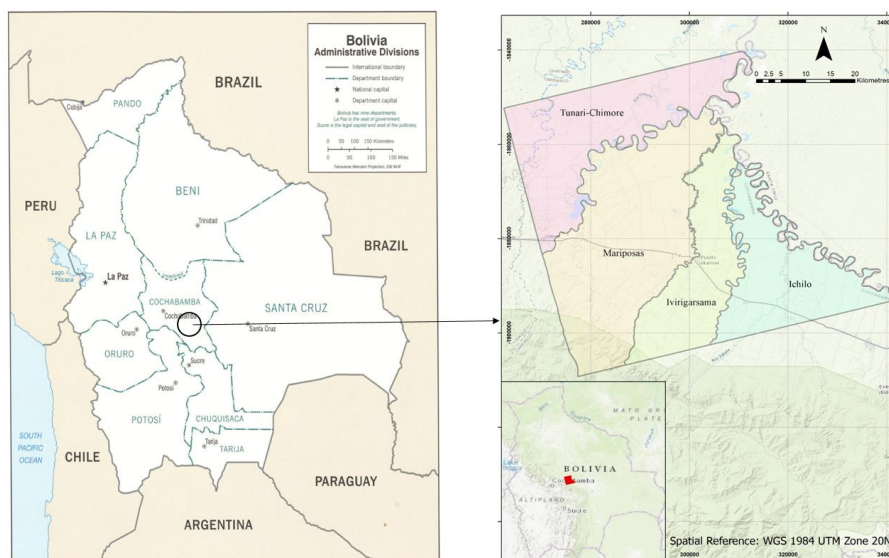
Figure 2: Administrative Map of Bolivia (left) and Map of the study area overlaid on a Topographic basemap (right)

(Source: https://legacy.lib.utexas.edu/maps/americas/bolivia_admin_2006.jpg)

The area of study focuses on Chapare in central Cochabamba Department (Figure 2). Among the nine departments of Bolivia, Cochabamba is well known for its food production (Stearman, 1985). The Cochabamba valleys are considered as one of the country's major sources of agricultural products because of its favourable climate and fertile, productive soils (Steininger et al., 2001). With the area of 55,631 km2 and the population of 1,758,143, Cochabamba is also a major transportation hub that joins the two biggest cities of Bolivia: La Paz and Santa Cruz (Millington et al., 2003). The department shares borders with Chuquisaca and Potosi Departments towards the south, the Departments of Oruro and La Paz in the western part, Beni to the north and Santa Cruz to the east (Figure 2) (Fearnside, 2005, Tejada et al., 2016). The borders between the departments are often created by rivers. There are 16 provinces in Cochabamba Department and the study area is in Carrasco Province and is spread over four municipalities: Entre Ríos, Chimore, Puerto Villarroel and Totora in Bolivia (Olivera and Lewis, 2004).

Carrasco Province has an area of 12,469 km^2 among which 2,918 km^2 is covered by the area of study (Olivera and Lewis, 2004). According to the 2012 census the estimated 135,097 people reside in the Carrasco Province. The extent of the study area lies between 64° 28' W to 65° 13' W and 16° 38' S to 17° 15' S (Morales and Nationalism, 2015).

1.4 Aims and Objectives

Insights on the increasing trend of tropical forest fragmentation as well as the need to adopt remote sensing for its monitoring and quantification have been provided in the previous section. The overall aim of the research in this thesis is to map deforestation in the lowland tropical Bolivia using satellite RADAR, which penetrates cloud and to compare the results with those from optical remote sensing, to provide information for analysis of tropical forest fragmentation. This will be achieved by examining statistically classified images obtained from optical and RADAR sensors. This research will help to answer following research question: *Which sensors, optical or RADAR, provide better accuracy in mapping tropical forest fragmentation?*

The following objectives are proposed to achieve the research aim:
   a. Highlighting issues and complexity in using optical remote sensing for tropical forest fragmentation monitoring.
   b. Reviewing the feasibility of RADAR operations in tropical domains.
   c. Performing image classification on both optical and RADAR imagery and comparing the classification accuracies between RADAR and optical classified imagery

1.5 Potential significance of the research

The potential significance of this research is to understand the capabilities and importance of satellite remote sensors for monitoring forest clearance in the tropical nations, which in time will provide a certain level of understanding that can help ecologists to monitor these forests better. This research will also benefit governments of tropical nations in accomplishing better planning without inflicting greater damage to the nation's tropical forests.

1.6 Organisation of the thesis

This thesis is organized into 6 chapters. Chapter 1 includes an introduction to the research as well as the aim and objectives followed by the research objectives. Chapter 2 explores literature related to deforestation in global, tropical and in Bolivian contexts. This chapter also incorporates the mapping of deforestation and the use of different remote sensing sensors and technologies in order to monitor forest fragmentation in the tropical domain. Chapter 3 specifies the overall framework of methods

used to address the research objectives carried out in this research. It also gives insight to the detail study of methods that was used for mapping forest fragmentation using both optical and RADAR remote sensing. Chapter 4 includes all the results that were obtained throughout the research. Chapter 5 presents a discussion of results and examines some key issues relating to the methods and results. Finally, chapter 6 provides the conclusions and some recommendations to this research.

CHAPTER TWO

LITERATURE REVIEW

2.1 Global Deforestation

Deforestation is considered as a major event when looking at the history of earth's transformation (Williams, 2000). It refers to the clearing of a forest when land is made accessible for other uses. Forest has been estimated to cover about 30% of the global land (Keenan et al., 2015); but every year around 72,843 km^2 of forest land are lost to deforestation (Kauppi et al., 2006). There are several causes for deforestation, some of the major ones are timber harvesting for the purposes of building construction, sold as charcoal or timber, and land used for agricultural farming and cattle grazing (Calymca, 2018).

In the present context, forests are being cleared on a massive scale which has deteriorated the quality of the land (Lambin, 1999). This phenomenon has been occurring throughout the world particularly targeting tropical rainforests. According to National Geographic (2018), the rainforests around the world will be in the verge of extinction in about 100 years if the current deforestation rate continues if no regeneration is taken into account. The trend of deforestation can be traced back hundreds of years where forests used to be cleared out for settlement and agricultural purpose.

Tropical regions around the world have been a major target of deforestation since 1950, but it is said to have started when the earth was first occupied by the humans where people used fire intentionally for deforestation about half a million years ago (Williams, 2000). Forests have been used as a shelter for people and wildlife (Kauppi et al., 2006). Deforestation is considered as a major cause for the loss of life of endangered species living inside the forests (Lambin, 1999). Deforestation has both direct and indirect impacts on humans and the environment since millions of people have been relying on forests for shelter, food, clothing and freshwater (Kauppi et al., 2006). According to WWF (2018), the loss of forest in the Amazon Basin was recorded to be around 17% in the time frame of the last 50 years. Deforestation is done not only for the domestic and commercial purposes, but they have been found to be used during the time of war (Kauppi et al., 2006). During war of 1846, the American soldiers used these forests as a crucial force to deprive the Mexican soldiers of their essential resources and to blow their cover (Williams, 2000).

Deforestation is induced by both human and nature and is a serious ongoing issue. Human activities such as mining, expansion of agricultural land, and urbanization, logging and natural phenomenon such as bush fires and forest wildfires are the causes of deforestation (Keenan et al., 2015). As a part of his research Williams (2000) verified that the total forest clearance around the world was found to be around 2.3 million square kilometres in the years between 2000 and 2012. A study in deforestation conducted by University of Maryland concluded on the global deforestation reaching 29.7 million hectares in 2016 and the trend has continued since (Calymca, 2018).

The deforestation patterns differ around the world. The regions with the largest impact of deforestation are the tropical regions of Africa and South America (Williams, 2000). The loss of forest is continuous in Europe, but the rate has slowed compared to previous years while the regions of North America and Central America exhibits no change in total forest areas (Calymca, 2018). Deforestation rate in South East Asia is estimated to be 1% (Miettinen et al., 2011). According to WWF (2018), around the estimated value of 15% of greenhouse gas emission originate from clearing of forests which in point leads to increasing global warning, greenhouse gases andclimate change.

The level of intensity of deforestation varies depending on the location of tropical rainforest. The equatorial region hosts the tropical rainforest which averages an annual precipitation of about 1680 millimetres (Kauppi et al., 2006). These rainforests are found between 10° north and south of the Equator (Houghton, 1991).. The Intergovernmental Panel on Climate Change (IPCC) stated that estimates regarding the deforestation in tropical countries may have and error of around 50% (Calymca 2018). Tropical forest is the largest terrestrial component of the global carbon budget (Bonan, 2008). They account for 50% of the carbon stored in global vegetation (Houghton et al., 2009, Houghton, 1991). The tropical forest region deserves attention due to economic, demographic and socio-economic conditions that still exert pressure on the forest condition in the region, and the fact that the majority of world's biodiversity resides in these areas (FAO 2007).

However, rapid clearing of tropical forests for the sole purpose of expansion and improvement in the livelihood of the society surrounding such areas is still prevalent which result as a major source for emission of greenhouse gases resulting in global warming (Houghton, 1991). Such clearance gives rise to forest fragmentation which in turn affects the leftovers of forest as well. Forest within 100m of edges of fragments were assumed to lose 10.6% of above ground biomass (8.8% from tree mortality and 1.8% from tree damage) (Laurance and Bierregaard, 1997, Laurance et al., 1998).

2.2 Forest Fragmentation

Forest fragmentation is regarded as a major contributor to the loss and detriment of species diversity globally (Noss and Cooperrider, 1994). A key process in forest fragmentation is the clearing portions of forest into smaller patches, mostly separated by either man-made features such as roads, settlements, agriculture or by the natural corridors (Collingham and Huntley, 2000, Fahrig, 2003, Wilcove et al., 1986). Forest fragmentation has been considered to be a source of isolation of forests and natural forest degradation.

Fragmentation has the tendency to occur usually in an incremental fashion starting with the patches being cleared appearing randomly (Freeman and Fox, 1994). Once the process of fragmentation is initiated, more and more amount of non-forest patches tend to occur and eventually multiplying and expanding until the forest area is either reduced to scatter creating numerous disconnected forest islands or completely turning into something else than its original land-cover status (Margono et al., 2012). With the increment of numerous non-forest land covers will eventually have the serious effect on the functionality, health status and the natural value of the remaining patch of forest (Noss and Cooperrider, 1994).

A forest can be affected whenever there occur any disturbances in any large-scale canopy. It is always crucial to differentiate the cause of fragmentation which either involves the human infrastructure development or the variation on the canopy closure between forests of mixed ages represented by the after effect of a proper forest management system (Laurance et al., 1998). The effect of forest fragmentation is much more dangerous in a former stage than in the latter stage (Jha et al., 2005). The effects can range from permanent negative impacts such as deteriorating the habitat quality as well as health of the forest to minor temporary change (Jha et al., 2005). These sorts of changes and effects have been experienced globally.

Many researchers (Fahrig, 2003, Haila, 2002, Lindenmayer and Franklin, 2002) have focused their study on the concept of distinction between forest fragmentation and habitat loss primarily taking the impact factor on diversity into account. Numerous landscape experts have considered both these phenomena to be inseparably related thus suggesting the fact that habitat loss can be considered as a vital component of forest fragmentation (Yaacobi et al., 2007).

With the disturbance and degradation in the natural habitat results in the biodiversity being lost with increment in the population of invasive pathogens, plants and pests as well as loss of quality of water

9

(Jha et al., 2005). As the isolation of forest occurs, it eventually restricts in the breeding and genetical flow in plants and animals since it forbids their movements (Laurance and Bierregaard, 1997). This will result in the declination of population in a long- term scale. Forest habitat can be taken as one of the major aspects for adaptation and response towards climate change and forest fragmentation stands as a threat towards the natural resilience of the forest ecosystem (Myers et al., 2000).

2.3 Bolivian Deforestation and Fragmentation

According to (Stearman, 1985), the clearance of forest areas in Bolivia occurred with the rise of migration of people from the highlands to low lands, construction of road networks, high amount of foreign investment, the prices of the land being very low in low land tropics, high demands of agriculture etc.

The lowlands of Bolivia are listed among the high degree of conservation urgencies in the world (Myers et al., 2000). Due to the loss of forest from year 2000 to 2010, Bolivia is registered as one of the highest net forest loss territory in the world despite having 50% of their region occupied by lowland forests (Tejada et al., 2016).

The study by (Pacheco, 2006) stated that the trend of forest fragmentation in Bolivia started due to the huge migration of farmers from Andean region to the low land tropics around 1950s to 1970s creating various colonies all around low lands of Bolivia. This movement of people was a program conducted by the central government of Bolivia so as to fulfil the requirement of cheap labours for up growing agro-industry and to extend the range of agriculture (Pacheco, 2006).

Another event that led to massive deforestation took place during the mid-1980s where 75 % of the south-western tropical forest were cleared out by agro-industrial corporations by converting them into agricultural lands (Tejada et al., 2016). With the trend of deforestation rising, around the year of 1990s, majority of tropical forests were cleared out for the construction of highways, infrastructures and silos (Pacheco, 2006). This was possible with the financial aid of World Bank.

With the increase in population in low land, deforestation rate reached the top and around 2000s, the bloom in the sector of mechanized agricultural predominantly soybean revolutionized both local and international market which became the sole reason of deforestation in that period of time (Müller et

al., 2011). In the present context, the major driving force of forest fragmentation in Bolivia is the never ending high demand for agricultural goods (Tejada et al., 2016).

2.4 Mapping Deforestation in a tropical context

Looking at the past two to three decades, the rate of change in tropical forest areas to agricultural lands has been seen to rapidly increase. Massive deforestation has always brought greater costs such as increasing instability in global climate, rise in atmospheric carbon level and major loss in the genetic legacy of Earth. Research by (Freeman and Fox, 1994) stated that on a global context, deforestation in tropical forests can only be monitored and mapped with the help of GIS tools and remotely sensed images which is achieved by plotting and calculating the various outputs obtained from image analysis.

Since 1973, most of the deforestation on tropical regions of the world are mapped with the imagery obtained from NASA's Landsat satellites (Irons et al., 2012). With the analysis of satellite images and other correlated data, various mappings have been done throughout the years providing information relating to the pattern of deforestation, and rate in change of forest areas to other uses in tropical regions (Malingreau, 1991). As there were higher expectations from the early satellite images, they could not meet the demands of the analysts that required outputs with greater accuracies (Irons et al., 2012). Later, around the 1980s, the availability of higher spatial resolution images was made possible.

At that period, all the tropical nations were trying their best to slow down the rate of deforestation (Houghton, 1991). The tropical deforestation became the world's leading issue when the global climate change came to primary focus in the international consensus (Laurance and Bierregaard, 1997). Meanwhile, the field of spatial science has been growing at a fast pace with gradually increasing in the use of GIS and remote sensing technologies for global forest mapping and tropical forest fragmentation monitoring (Lambin, 1999, Margono et al., 2012, Sánchez-Azofeifa et al., 2001).

As remote sensing technology improves so does the accuracy of the remote sensing data (Almeida-Filho et al., 2005). As of now, accuracy depends on how fine the spatial resolution is and what type of electromagnetic spectra are being sensed (Freeman and Fox, 1994). From the year 1973 to now, the size of the pixel has drastically reduced from 80 metres used in Landsat MSS sensor to sub-metre (Congalton, 1991a, Donoghue, 2000). The development of high-resolution optical sensors and RADAR sensors now have revolutionized the field of remote sensing in mapping forest degradation (Evans et al., 2010, Hansen et al., 2008). The capability of RADAR sensor to penetrate cloud with its long

11

wavelengths has been accepted by most researchers as a fundamental substitute to optical sensor while monitoring rainforests (Dong et al., 2014, Evans et al., 2010, Hyde et al., 2006, Saatchi et al., 1997).

In order to map tropical forest degradation, researchers must have a clear synoptic and repetitive coverage of the region and remote sensing generally fits perfectly in satisfying these requirements (Rees and Pellika, 2010, Richards, 2013). In the last 20 years, the evolution of satellites has made monitoring of the world dynamic features and its environments possible (Moraniec, 2011). Tropical forest deforestation mapping has become a global subject and it's just the beginning to variety of solutions (Taubert et al., 2018). The vast investments in global climate change created a pathway for using space borne technology to map fragmenting forests (Evans et al., 2010).

The studies and assessments on tropical forests deforestation have been made possible through the use of various maps, sources and years and years of observations (Jha et al., 2005). The results of these studies have statistically proven for tropical forest degradation to reach the estimate from 15.5 million hectares per year on a lower scale to 20.4 million hectares per year on a higher scale (Taubert et al., 2018).

2.5. Remote Sensing of deforestation in a tropical context

Mapping tropical fragmentation at a global scale using satellite sensor platform is always a challenge but the rapid advancement in technology has always been the backbone for these studies (Donoghue, 2000). The improvement in a specific technical field leads to massive change in another field such as the increase in the sensor's resolution and the image classification being automatic in nature affects the capabilities of hardware and software necessities in a computer (Joseph 2005, Liu and Henrik 2018). With these technologies exerting dynamic relationship between each other, detecting the tropical forest change and mapping of tropical forest fragmentation has been relatively easier as the innovation in the area of mapping methods are continuous (Margono et al., 2012). Such ease has given rise to initiatives such as the Global Forest Watch (GFW). The GFW was launched in 1997 as to provide transparency and accountability in the decision-making processes on how to manage the forests and for whom to manage it for (Watch, 2002). It is an international mapping network storing data that takes knowledge from the ground with the help of digital technology in order to provide information about the different forests of the world (Watch, 2002).

In order to map tropical forest fragmentation, a set of indicators are necessary that can elaborate the biological and physical characteristics of the surface, type of spatial pattern in a finer scale and their seasonal occurrence (Lillesand et al., 2014). There are three distinctive sources that provide the detailed information relating to the above requirements in remote sensing. With the integration of those three different resolutions i.e. spatial, spectral and temporal, mapping and monitoring of tropical deforestation is made possible with a better understanding of the complex ecological phenomena (Lambin, 1999).

Large scale data acquisition is required for analysing events such as deforestation and remote sensing has proven to be advantageous over typical field-based data collection (Hyde et al., 2006). Remotely sensed data enables the quantification of forest cover and changes to it by providing information on how fast forest land cover changes are taking place (Hansen et al., 2008, Jha et al., 2005). Various remote sensing methods have already been prototyped within this field of study. Landsat thematic mapper images have proven to provide sufficient spectral and spatial resolution for determining the extent of tropical deforestation (Lambin, 1999). Analysis of such images and visual interpretation of such images has produced quantitative results similar to processing the data digitally of full resolution (Siegert and Hoffmann, 2000). Skole and Tucker (1993) used channel five of Landsat thematic mapper and performed digitization of the deforested areas with visual deforestation interpretation and other standard GIS techniques resulting in the finding the deforestation rate of the Amazonian tropical forest.

Similarly, Hansen et al. (2008) used MODIS images of daily images at a global scale in order to acquire the best cloud free observations. However, accurate changes in area could not be estimated based on MODIS alone as some changes took place in sub pixel class of MODIS (Gao et al., 2015). Hence, LANDSAT higher spatial resolution imagery was used to measure forest area change. However, factors such as frequent cloud cover and cost of data (in the past) has proven LANDSAT imagery to be precluded in biome scale mapping (Moraniec, 2011). Classification schemes are used in order to classify the different land covers present in the satellite imageries (Jha et al., 2005, Lu and Weng, 2007).

Classification schemes regardless of the data type helps identify closed forest, non- forest area, water bodies, urban areas, clouds and cloud shadows as well as helps classify the different vegetation cover present on the surface of the land (Congalton, 1991a). In the research in this thesis, the main classification scheme to help identify deforestation and quantify the findings is the use of two main classification schemes which is detecting the change of land cover from forest to non-forest and

13

mapping the fragmenting forest. However, errors still exist in classification schemes. (Sánchez-Azofeifa et al., 2001) came across an error of 10 percent while quantifying the deforestation in Costa Rica using Remote sensing Imagery with an expected accuracy of 85 percent.

Apart from optical imagery microwave sensors have also proven to be effective in change detection in tropical forest scenarios (Dong et al., 2014). L band SAR has proven to be sensitive towards the structure of vegetation and can also be acquired consistently on a repetitive basic regardless of different weather conditions, can be used to complement the areas where optical data is missing (Almeida-Filho et al., 2005). Almeida-Filho et al., (2005) concluded that use of SAR helps differentiate between actual areas of complete deforestation and areas with branches and stems lying on the ground based on reading of the backscatter. The research by Hyde et al., (2006) concluded that the sensitivity of L-band SAR to such vegetation structure and its capacity to penetrate cloud and haze makes it complement optical systems in monitoring programs. However, the application of single-polarized radar data seems to be limited in detecting areas in areas where there was only initial phase of deforestation was detected (Cornforth et al., 2013).

The study by Freeman and Fox (1994) suggested how use of a cross-polarized channel and use of polarimetry Phased Array L-band Synthetic Aperture Radar (PALSAR) instruments would help overcome this shortcoming and assist in differentiating between forested and recently deforested area. Particular improvement of ALOS PALSAR noticed over SAR was the low noise floor for dark target distinction and also the accuracy of subpixel geolocation (Shimada et al., 2009). Also, ALOS PALSAR has multiple image modes in comparison to SAR and has a higher data flow rates as well (Rauste et al., 2007, Shimada et al., 2009, Sumantyo and Amini, 2008). All these facts helps to conclude on the emphasis on use of PALSAR in order to monitor not just the deforestation, but also the stage of deforestation was made (Freeman and Fox, 1994).

2.6 Remote Sensing Sensors

The history of digital sateliite remote sensors started in July 23, 1972 when Landsat-1 was launched with the goal of acquiring the information of Earth with remote sensing techniques. Landsat-1 had two sensors: Return Beam Vidicon (RBV) and Multispectral Scanner (MSS) with 4 number of bands (Rees and Pellika, 2010). After Landsat-1, with the launch of Seasat-1 becoming the first RADAR satellite, in 1978, the new domain of remote sensing was introduced (Roy et al., 2017). After these events, the field of remote sensing flourished like never before. The world experienced new optical and RADAR

sensors with higher spatial resolution and with the development of hyperspectral sensors accuracy of the real world data became the upmost priority.(Donoghue, 2000). The presence of variability in sensors helped in providing different level of information throughout the surface of the Earth (Donoghue, 2000, Joseph, 2005). Sensor provides information by measuring the electromagnetic radiation. The amount of information extracted from electromagnetic radiation depends upon various factors: wavelength, polarization, direction and intensity (Liu and Henrik, 2018). These sensors are categorized into two modes (Figure 3): Active and Passive according to their primary source of energy, operating level in electromagnetic spectrum and interaction between them and the Earth's surface (Figure 3) (Rees and Pellika, 2010).
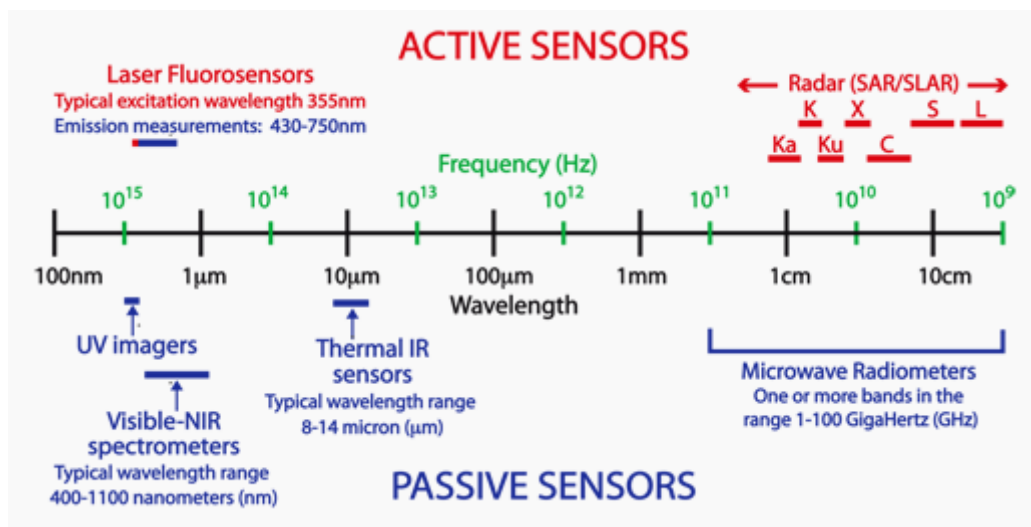
Figure 3: Remote Sensing Sensors

(Source: http://lms.seos-project.eu/learning_modules/marinepollution/marinepollution-c01-s02-p01.html)

2.6.1 Active Remote Sensors

Active remote sensors have their own source of energy from which they measure the observations by illuminating the objects (Liu and Henrik, 2018) These sensors function in the wavelength range of visible light (700nm-400nm) and near infrared (780nm-2500nm) and radar waves (Table 1) in the electromagnetic spectrum (Joseph, 2005). A laser rangefinder is an active sensor that operates in the wavelength range of visible light and near infrared, where Synthetic Aperture Radar (SAR) operates in the wavelength of microwaves (Joseph, 2005). Basic mechanism behind a laser rangefinder is that, in order to calculate the distance of an object from sensor, it uses laser beam as a source of energy (Rees and Pellika, 2010). It is mostly used for terrestrial or airborne laser scanning while microwaves are used by SAR for object illumination where it measures and records the backscatter from the object as well as records the time taken by the backscatter after reflecting from the objects along the side-looking

geometry (Liu and Henrik, 2018) In order to generate a SAR image, initially successive number of radio waves pulses are transmitted for target illumination (Rosenqvist et al., 2007). Then, the backscatter of each of the transmitted pulses are recorded using single beam-forming antenna (Rosenqvist et al., 2007, Evans et al., 2010, Liu and Henrik 2018). Since SAR device in mounted on the satellite or on the aircraft, there occurs the movement of sensor platform with time. Due to this movement, the relative location of the antenna facing towards the target changes and the antenna records all successive backscatter from the target along the multiple antenna positions during signal processing (Rosenqvist et al., 2007). From this process, Synthetic Antenna Aperture is formed which allows the generation of SAR images with higher resolution (Rees and Pellika, 2010).

SAR sensors can be categorized on the basis of:

a. Polarization Modes

Polarization characteristics is shown by radar waves. It refers to the process where any radiation have a restriction in direction of vibration (Joseph, 2005). It is used for identifying the pattern of scattering behaviour shown by object after its contact with electromagnetic wave (Rosenqvist et al., 2007). Different objects give out different intensities while reflecting radar waves and some can even convert one polarization onto completely different polarization (Rees and Pellika, 2010).

i. Single Polarization (VV or VH or HV)

Here, VV indicates vertical transmission of radar waves and vertical receive,

VH indicates vertical transmission and horizontal receive and,

HV indicates horizontal transmission and vertical receive

ii. Multiple Polarization (combination of two or more polarization modes)

b. Combination of frequency bands.

i. Single Frequency (for example L-band or C-band or X-band)

P-band indicates the longest wavelength band among all SAR bands with the wavelength ranging between 130-30 centimetres and has the greatest penetrating power (Table 1). After P band, L-band is the second longest band with the wavelength of 30-15 centimetres. Similarly, after L band are S, C, X, Ku and K bands respectively (Table 1).

ii. Multiple Frequency (combination of two or more frequency bands)

16

Table 1: SAR Radar Frequency Bands

SAR RADAR Band	Frequency Range (GHz)	Corresponding Wavelength Range(centimetres)
P	0.230 -1	130 - 30
L	1-2	30 - 15
S	2-4	15 - 7.5
C	4-8	7.5 - 3.75
X	8-12.5	3.75 - 2.40
Ku	12.5-18	2.40 - 1.67
K	18 -26.5	1.67 - 1.13
Ka	26.5- 40	1.13 - 0.75

Source: https://lta.cr.usgs.gov/SAR

In using SAR sensors for mapping forest degradation or estimating AGB (Above Ground Biomass), SAR sensors appear to be very sensitive towards the various components of forest (Goetz et al., 2009). That sensitivity of SAR sensors is a measure of wavelength of the sensor. Band-X and Band-C are the bands with shorter wavelengths so there are sensitive towards the leaves and branches while Band-L and Band-P are sensitive towards the bigger branches and stems because of their longer wavelengths (Table 1, Figure 4) (Goetz et al., 2009, Hyde et al., 2006). As active remote sensors have their own source of illumination, they have benefitted remote sensing society by being able to capture image throughout day and night (Joseph, 2005). Having longer wavelength, active remote sensors are able to record information regardless the weather condition or cloud coverage which has proven to be a greater advantage over passive remote sensors (Malingreau, 1991, Rees and Pellika, 2010, Skole and Tucker, 1993).
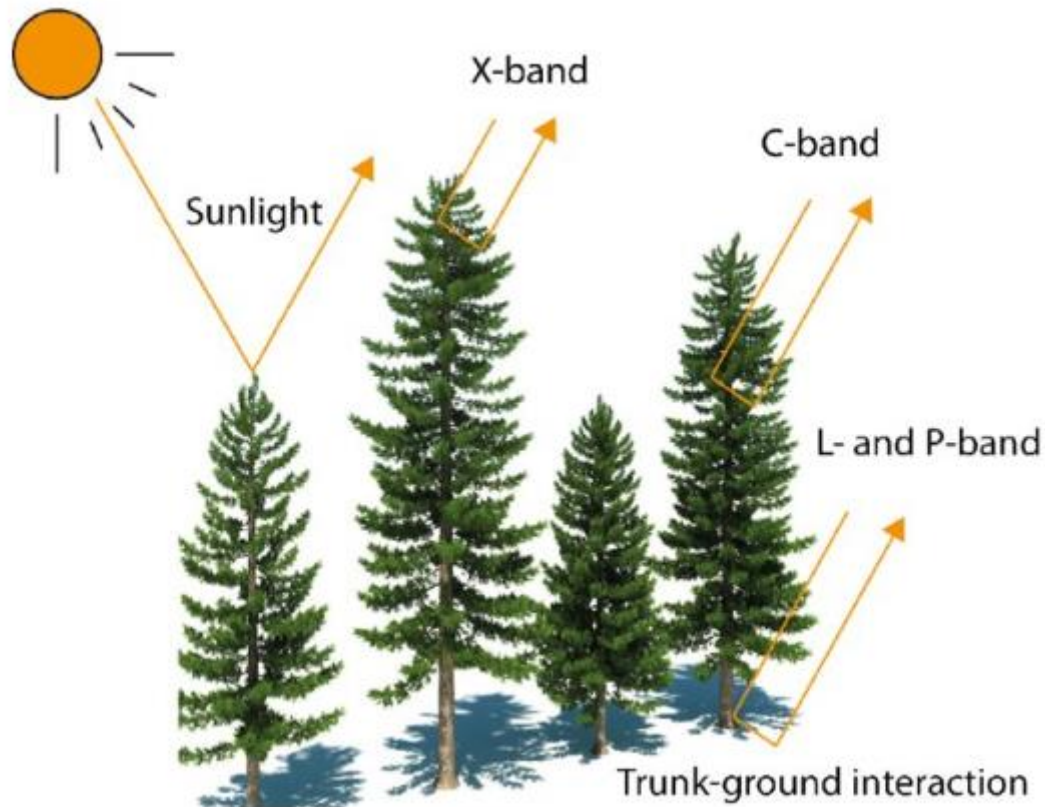
Figure 4: Illustration of the scattering (penetration) in a forest canopy with common remote sensing radar bands. Optical sensors using sunlight are included for comparison.

(Source:

https://www.researchgate.net/publication/269575726_Estimation_of_Forest_Parameters_Using_3D_Satellite

_Data_Stereogrammetry_radargrammetry_and_interferometry/figures?lo=1)

2.6.2 Passive Remote Sensors

Passive remote sensors don't have their own source of energy so they utilize solar radiation to detect the amount of energy reflected by illuminating the surface of the Earth (Liu and Henrik 2018). These sensors function in the wavelength range of visible (430-720 nm) and near-infrared (NIR) (750-950nm) light (Figure 3) (Liu and Henrik, 2018). Some of the sensors can even go beyond this limit and acquire images for e.g. SPOT 5 is designed to work in the electromagnetic wavelength of 1580-1750nm i.e. in the middle-infrared (MIR) wavelengths (Joseph, 2005). The power of passive sensors depends on the physical characteristics, surface roughness, surface composition and physical temperature of the Earth (Joseph, 2995, Liu and Henrik 2018). Some examples of passive remote sensors are: GeoEye, Pleiades and Landsat satellites.

Optical sensors are considered as a foundation of world's current mapping (Moraniec, 2011). With their wide range of application, Optical sensors have been found to be widely used in the area of mapping forest deforestation and degradation. Optical sensors appear to exhibit sensitivity towards variation of canopy chemical composition (Hyde et al., 2006). An optical sensor such as Landsat has a temporal resolution of 16 days which means there are possibilities of 23 data acquisitions in a year with a sensor resolution of 30 metre (Loveland and Dwyer, 2012). With the current atmospheric condition and the characteristics of Landsat orbit, the minimum time of 3 years is needed in order to achieve the Landsat scene with low cloud coverage (Kong et al., 2011, Makarau et al., 2014, Moro and Halounova, 2007). Sentinel 2 (A and B) have a revisit time of 5 days with around 73 acquisition per year, but the biggest drawback is the assumption of having a cloud free condition (Drusch et al., 2012). These sensors have the high potential for mapping earth surface, but they have been restricted by the wavelength they operate on (Kong et al., 2011, Lambin, 1999). Since these sensors are fully dependent on the illumination of the sun on the target, the presence of cloud during data acquisition is not something everybody should be surprised about (Kong et al., 2011, Moraniec, 2011, Moro and Halounova, 2007) . The major drawback of optical sensors are their inconsistency over large areas due to the change in the surface conditions occurring much faster than their revisit cycle of cloud-free observation (Roy et al., 2017, Skole and Tucker, 1993).

2.6.3 Microwave sensors over Optical sensors

This drawback of optical sensors can be overcome using microwave sensors with longer wavelength having greater penetrating strength (Shen et al., 2014). Cloud and haze are not an issue anymore when working with microwave sensors, but the temporal resolution of these sensors might be something worth considering. Microwave sensor like Sentinel 1a has a revisit time of 12 days resulting in nearly 22 number of acquisition per year (Drusch et al., 2012). It operates on C band which is enough to penetrate the atmospheric hindrances but can be restricted for the deeper study of forest degradation. As with Sentinel 1a, Radarsat also works on C band but the temporal resolution of 24 days which limits the data acquisition to only 15 (Jezek, 1999). However, a microwave sensor like ALOS is perfect for mapping forest degradation as it works on a L-Band frequency that can penetrate almost everything but there are only about 8-9 number of acquisition per year due to its temporal resolution being 46 days for ALOS 1 (Rosenqvist et al., 2007). However, for ALOS 2 has a temporal resolution of 14 days (Beck et al., 2000).

2.7 Summary

Forest fragmentation is an uprising issue in the world where tropical regions being the primary victim (Pacheco, 2002). The clearing of forest contributes to the massive carbon emission in the air escalating the effects of global warming (Lindenmayer and Franklin, 2002). This issue needs to be resolved by reducing the rate of deforestation. The initial approach is to find appropriate set of methods that best suits to tackle the problem and throughout the years, the mapping of forest fragmentation using remote sensing has always been the solution in managing and monitoring this issue (Liu and Henrik, 2018, Rees and Pellika, 2010). Different optical sensors with varying spatial resolutions have been used to map forest fragmentation in tropical regions for many years and there has always been one obstacle – a high probability of presence of cloud in the scene during data acquisition (Moro and Halounova, 2007, Steininger et al., 2001, Taubert et al., 2018). Due to this specific reason, the usable resources (Images) for optical sensors are very limited. But, there is always another alternative and in this case are microwave sensors. Microwave sensors overcome the limitation of optical sensors as microwave sensors work on wavelengths that are much longer than optical. These longer wavelength have higher penetrating strength which can easily pass through anything before striking the earth surface (Rauste et al., 2007). Specially the use of L band wavelengths has proved their worth for mapping forest fragmentation with greater accuracy (Dong et al., 2014).

Addressing the drawback of optical sensor and believing on the fact that microwave sensors can be an ideal replacement for optical sensors in mapping tropical forest fragmentation, this research plans to use both optical and microwave sensor to map tropical forest fragmentation and conclude on which sensor can provide better result/accuracy in mapping tropical forest fragmentation.

CHAPTER THREE

METHODS

Various remote sensing and GIS tools have been used in the mapping of forest fragmentation in both optical and microwave domain. This chapter highlights and describes the overall process that were used to achieve the targeted objectives for this research. Figure 5 gives insight to the overall methods used achieve the aim of this research.
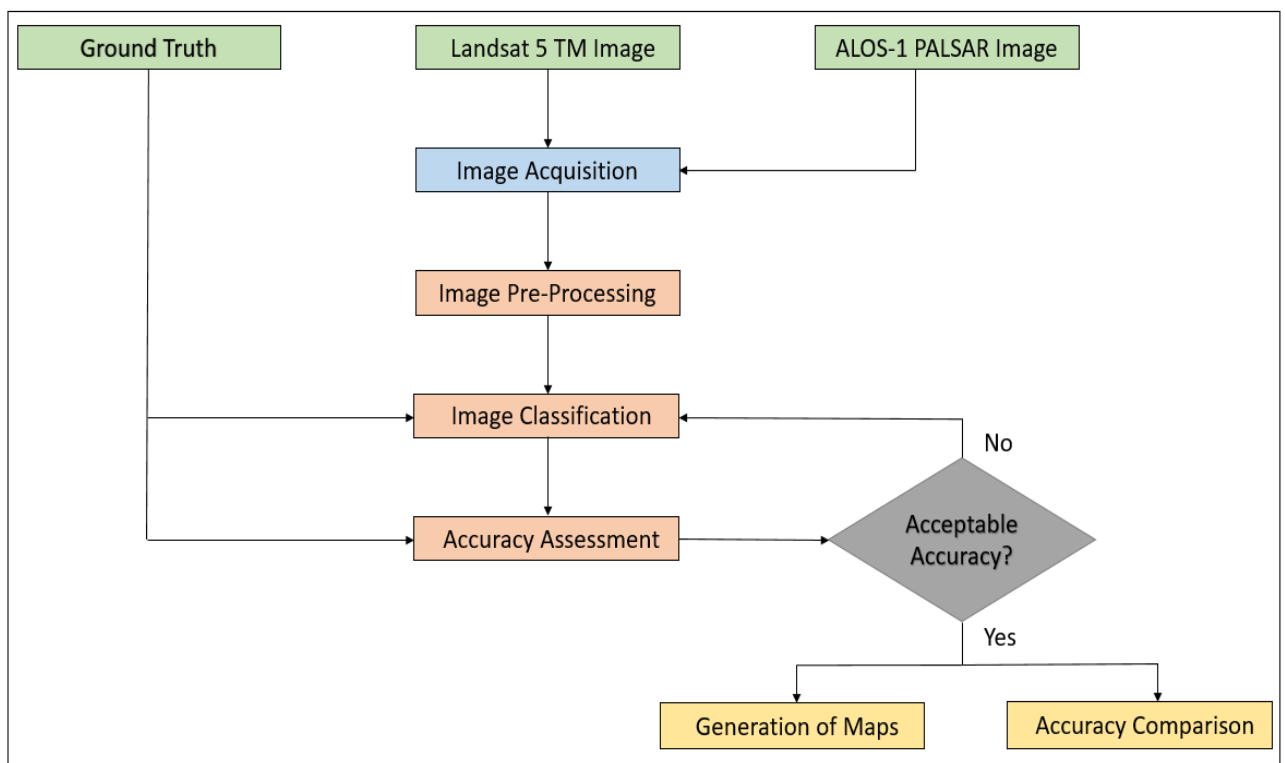
Figure 5: Overall workflow of this research

3.1 Data collection

The data used in this research ranges from vector point data to multiple raster images in different spectral regions. Due to the unavailability of the L-band RADAR sensor for year 2015 (initially proposed date of study) due to cost, the research had to be shifted to year 2007. The various data used in this research include:

a. Geo-referenced ground observations of land use collected in the dry seasons (Between August and September) in 2003, 2007 and 2015 (source: Professor Andrew Millington)

b. ALOS-1 PALSAR imagery of year 2007 (source: Alaskan Satellite Facility)

c. Landsat-5 TM imagery of year 2007 (source: United States Geological Survey)

d. Sentinel 2a imagery of year 2016 (source: Copernicus Open Access Hub)

3.1.1 Geo-referenced ground observations

Ground truth was collected by Professor Andrew Millington using a hand-held GPS along different transects of study area. These series of points were recorded in the dry season (Between August and September) which incorporates the data relating to the land use of the study area along the ground observation points. There were in total 161 points collected from the field work which were later used for geometric correction of ALOS-1 PALSAR imagery and for accuracy assessment of both Landsat 5 TM and ALOS-1 PALSAR classified raster. Along with the ground observation points, there was also the availability of field maps which was used as a primary source of information while performing image classification. These field maps provided the detail information of the land use of the study area along the East, West, North and South direction of the ground truth. The ground truth for accuracy assessment were manually created with reference to the field maps. The ground observation points were first downloaded from the handheld GPS and exported in a text format (.txt). The text file was then opened in Excel spreadsheet which was then converted to tab delimited format using the tool text to column which helped stored the data in a managed tabular structure. Once the Excel sheet was created, the ground points were manually entered on Google Earth via add placemark tool and later exported in a .kmz format. The .kmz file was then converted into a shapefile (.shp) in ArcMAP using the conversion tool kml to layer.

3.1.2 ALOS-1 PALSAR imagery from Alaskan Satellite Facility (ASF)

The Alaskan Satellite Facility was previously known as Alaskan Synthetic Aperture Radar (SAR) facility since it started as a single-purpose receiving station (Oliver and Quegan, 2004). After the success of Seasat-1 mission in 1978, new domain of remote sensing was started which foresaw the potential of space-borne SAR in the field of mapping (Bamler, 2000). ASF now serves as a gateway through which SAR data can be accessed.

Phased Array L-band Synthetic Aperture Radar (PALSAR) is classified as a microwave sensor that is mounted on Advance Land Observing Satellite (ALOS) (Almeida-Filho et al., 2005, Evans et al., 2010). The PALSAR uses L-band frequency (centre frequency 1.27 GHz) for its operation along with co-polarisation HH and VV

polarizations with cross-polarisations HV and VH as its optional data (Shimada et al., 2009). ALOS 1 was launched into a sun-synchronous sub-Recurrent orbit on 24th of January, 2006 with an angle of 98.16 degrees at the altitude of 691.65 kilometres (Joseph, 2005, Liu and Henrik, 2018). The main spacecraft operations control centres are Japan Aerospace Exploration Agency (JAXA) and JAROS. The PALSAR was designed to have a life of 3-5 years where it successfully completed its mission and was deactivated on 12th of May, 2011 after serving for 5 years, 3 months and 18 days (Liu and Henrik, 2018). From its lunch till the very last day, ALOS PALSAR generated continuous data despite of any weather restrictions or Day-Night effects (Bamler, 2000) . This sensor was initially developed to potentially support the mapping field, help in precise observation of regional land-cover, and contribute in disaster monitoring and resource surveying (Evans et al., 2010). There are 3 different beam modes for PALSAR with respective chirp bandwidth, polarization, range resolution, spatial resolution and observation swath which can be seen in Table 2.

If available, ALOS-1 PALSAR data can be obtained in various modes and in different processing levels. The raw data are generally represented by processing Level 0 and the Single Look Complex (SLC) data are represented by processing Level 1.1 (Table 2).

Table 2: Information regarding the instrument mode, product type, processing level of ALOS-1 PALSAR

Instrument mode	Product type	Processing Level description	JAXA processing level equivalent
Fine Beam Single polarization	FBS_RAW_0P	Raw data generated by every downlink segment and every band. Divided into an equivalent size to one scene.	1.0
	FBS_GDH_1P	Ground range Detected, Normal resolution product	1.5
	FBS_GEC_1P	Geocoded product	1.5
	FBS_SLC_1P	Slant range single look complex product	1.1
Fine Beam Double polarization	FBD_RAW_0P	Raw data generated by every downlink segment and every band. Divided into an equivalent size to one scene.	1.0
	FBD_GDH_1P	Ground range Detected, Normal resolution product	1.5

	FBD_GEC_1P	Geocoded product	1.5
	FBD_SLC_1P	Slant range single look complex product	1.1
Polarimetry mode (4 polarization)	PLR_RAW_0P	Raw data generated by every downlink segment and every band. Divided into an equivalent size to one scene.	1.0
	PLR_GDH_1P	Ground range Detected, Normal resolution product	1.5
	PLR_GEC_1P	Geocoded product	1.5
	PLR_SLC_1P	Slant range single look complex product	1.1

Source: http://www.ga.gov.au/__data/assets/pdf_file/0019/11719/GA10287.pdf

Table 3: PALSAR Beam Modes

	Fine Resolution		ScanSAR	Polarimetric
Beam Mode	FBS	FDS	WB1 WB2	PLR
Centre Frequency	L-Band (1.27 GHz)			
Polarization	HH or VV	HH+HV or VV+VH	HH or VV	HH+HV+VV+VH
Spatial Resolution	10m	20m	100m	30m
Range Resolution	7 to 44m	14 to 88m	100m (multi look)	24 to 89m
Swath Width	70 km	70 km	250-350 km	30 km
Off-Nadir Angle	34.3 degrees (default)		27.1 degrees (default)	21.5 degrees (default)

Source: http://www.ga.gov.au/__data/assets/pdf_file/0019/11719/GA10287.pdf
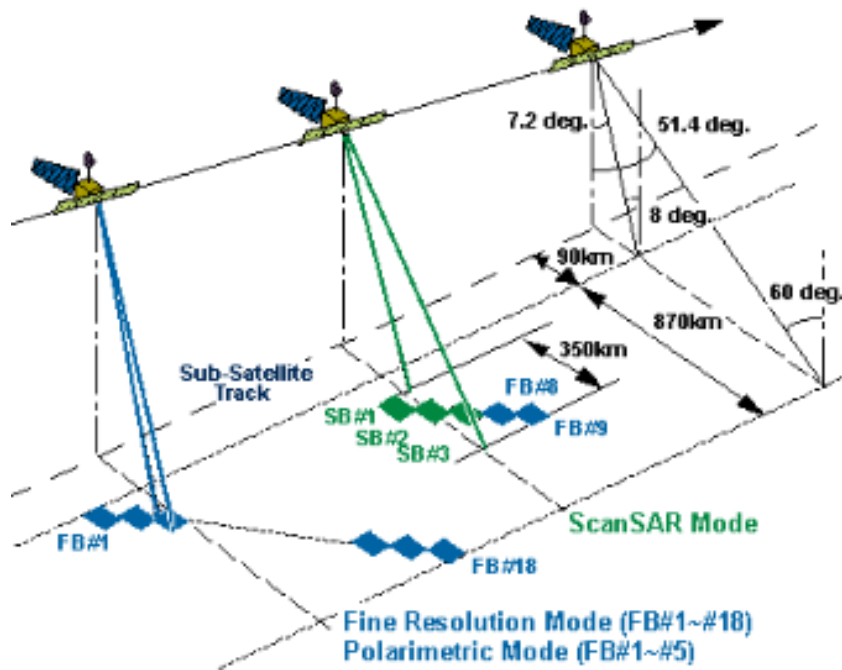
Figure 6: Graphical Representation of PALSAR Beam Modes

Source: http://www.alos-restec.jp

The selection of image for the study area was based on the availability of the ALOS-1 PALSAR image for year 2007. The image was downloaded through ASF portal. The raw image was a Single Look Complex (SLC) image with dual polarization (HH +HV). The range compression and 1 look compression had already been performed. The raw data was in complex form in slant range coordinates. Usually processing Level 0 data refers to the raw telemetry data that are attained from Atmospheric Imaging Assembly (AIA) instrument. After obtaining raw telemetry data, the data undergoes editing where orbit information is added which changes the processing level to Level 1.0. And finally, SLC image (Processing Level 1.1) is obtained when SAR processing is rendered to the product of Level 1.0.

Table 3: Scene Information of ALOS-1 PALSAR imagery

ALOS PALSAR Scene ID	Product Format	Number of Pixels	Number of Lines	Date of acquisition
ALPSRP088696840	CEOS	4640	18432	2007-09-24

3.1.3 Landsat-5 TM imagery of year 2007 from United States Geological Survey
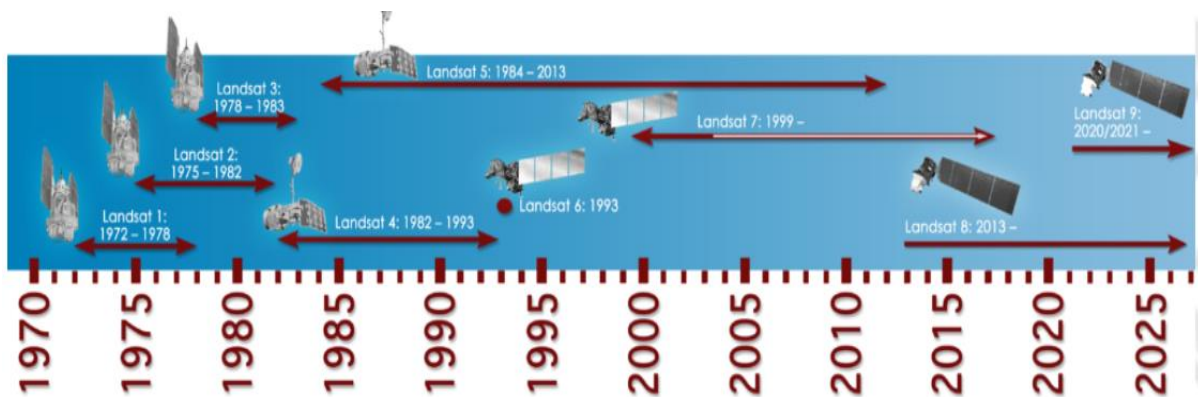
Figure 7: A Landsat Timeline

Source: https://landsat.gsfc.nasa.gov/a-landsat-timeline/

Numerous users have been relying on Landsat data for historical study of changes in the land surface of Earth (Short, 1976, Williams et al., 2006). USGS on 1982, took the initiative of producing much more high-level Landsat data focusing on the study of land surface change which was later named Landsat surface reflectance. The products of Landsat surface reflectance are free of atmospheric, illumination and geometric effects since it approximates the measurement as if the data has been captured from just above the ground surface (Figure 8) (Liu and Henrik, 2018). These products have proven to be more consistent than other Landsat products.

Figure 8: Subsets of a Landsat scene of Mount Vesuvius near Naples, Italy, display A, natural color composite; B, top-of-atmosphere reflectance and C, surface reflectance processing

Source: https://pubs.usgs.gov/fs/2015/3034/pdf/fs2015-3034.pdf

As year 2007 was selected for the overall analysis in this research, there were choices between Landsat 5 TM and Landsat 7 ETM+ (Figure 7). The problem with the Landsat 7 ETM+ is that there exists gaps in the data of all the Landsat ETM+ products acquired after May 31st, 2003 due to the failure in the Scan Line Corrector. Without functional Scan Line Corrector, there is approximately 22% of missing data in Landsat 7 ETM+ products which lead to discarding of the choice of Landsat 7 ETM+ (Irons et al., 2012, Loveland and Dwyer, 2012, Short, 1976, Williams et al., 2006). With the availability of Landsat 5 TM image for 2007 over study area (Table 5) with acceptable cloud coverage, Landsat 5 TM was selected as the optical sensor for this research.

The Landsat 5 TM images was searched initially in the United States Geological Survey Earth Explorer (EE) portal. Since the revisit time of Landsat 5 TM is 16 days, there were around 22- 23 potential images for year 2007 (Irons et al., 2012). The images were narrowed down to match the data acquisition time frame with ground observations. After filtering, only 1 image was found to have a small of cloud coverage. Even that specific Landsat image had considerate amount of haze in it. Once the image was selected, an order was placed in Earth Explorer portal for Landsat TM land surface reflectance Level-2 data. The obtained image was already subjected to atmospheric correction and geometric correction. Thus, obtained Landsat 5 TM image contained 6 spectral bands with 30 metres spatial resolution (Table 3) with Thermal band in exception and 4 quality assurance (QA) bands— Atmosphere opacity, Radiometric Saturation, Cloud and Pixel QA band. Table 4 shows the scene information of Landsat 5 TM.

Table 4: Designated Bands of Landsat 5 TM Surface Reflectance Level-2

Landsat 5 Thematic Mapper (TM)	Bands	Wavelength (micrometers)	Resolution (meters)
	Band 1 - Blue	0.45-0.52	30
	Band 2 - Green	0.52-0.60	30
	Band 3 - Red	0.63-0.69	30
	Band 4 - Near Infrared (NIR)	0.76-0.90	30
	Band 5 - Shortwave Infrared (SWIR) 1	1.55-1.75	30
	Band 7 - Shortwave Infrared (SWIR) 2	2.08-2.35	30

Table 5: Scene Information (Path 232, Row 072)

Landsat-5 TM Scene ID	Sun Azimuth	Sun Elevation	Date of acquisition	Cloud Cover
LT05_L1TP_232072	64.79º	57.74º	2007-09-28	7%

3.1.4 Sentinel 2a imagery of year 2016 from Copernicus Open Access Hub

Sentinels Scientific Data Hub now known as Copernicus Open Access Hub provides open access to all the user products of Sentinel-1, Sentinel-2 and Sentinel-3 satellites (Liu and Henrik, Roy et al., 2017). These data are completely free of cost. With Sentinel-1 being a radar sensor, Sentinel-2 being a multi-spectral optical mission and Sentinel-3 being a multi-instrumental mission, Copernicus Open Access Hub provides wide variety of data with higher resolution (Liu and Henrik). This service is governed by European Copernicus project.

The date of acquisition of the Sentinel 2a imagery is 2016-09-28 with the processing Level of 1C which indicates the presence of cloud masks as well as Top Of Atmosphere (TOA) reflectance. The products of processing level 1C have been resampled with Ground Sampling Distance (GSD) of 10, 20 and 60m which depends on the built-in resolution of various spectral bands. Sentinel 2a imagery was only used for geometric correction of ALOS-1 PALSAR imagery.

The different bands of Sentinel 2a imagery are shown in Figure 9, 10 and 11.
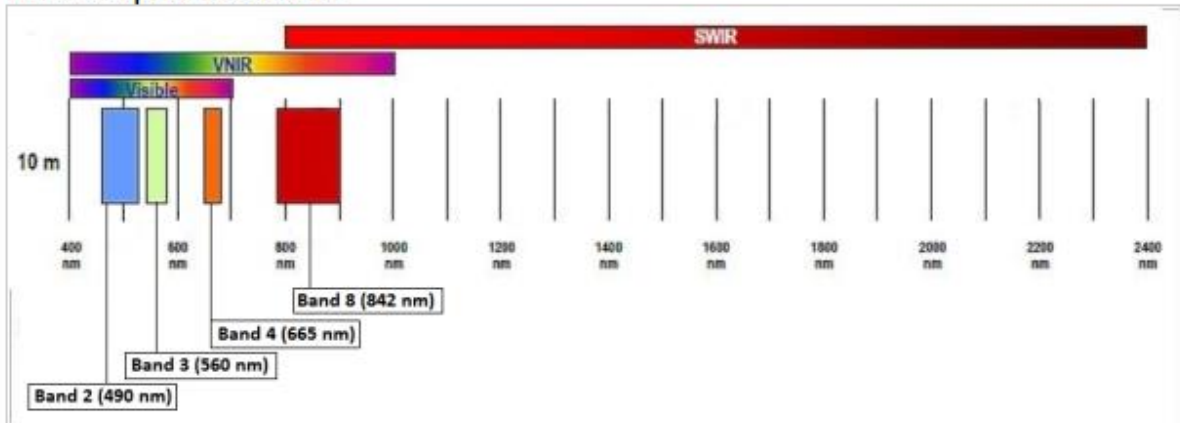
Figure 9: SENTINEL-2 10 m spatial resolution bands: B2 (490 nm), B3 (560 nm), B4 (665 nm) and B8 (842 nm)

Source: https://earth.esa.int/web/sentinel/user-guides/sentinel-2-msi/resolutions/spatial
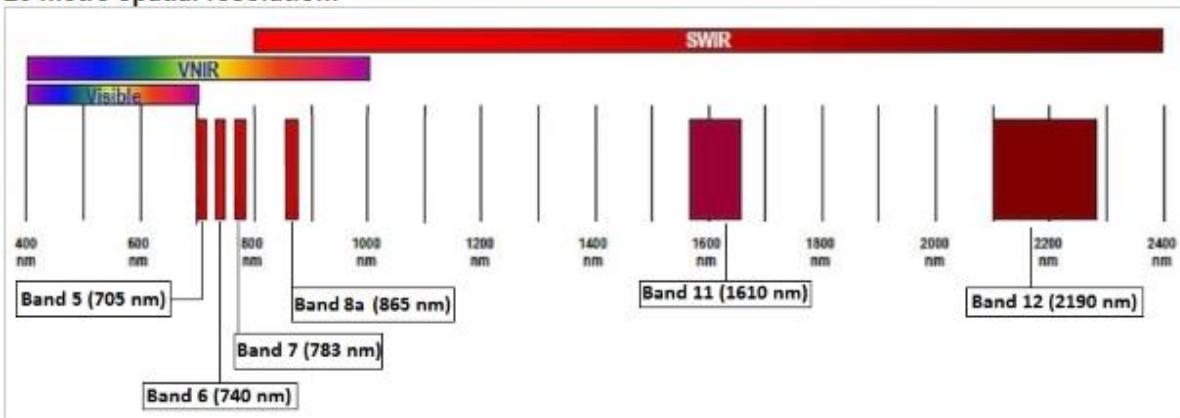
Figure 10: SENTINEL-2 20 m spatial resolution bands: B5 (705 nm), B6 (740 nm), B7 (783 nm), B8a (865 nm), B11 (1610 nm) and B12 (2190 nm)

Source: https://earth.esa.int/web/sentinel/user-guides/sentinel-2-msi/resolutions/spatial
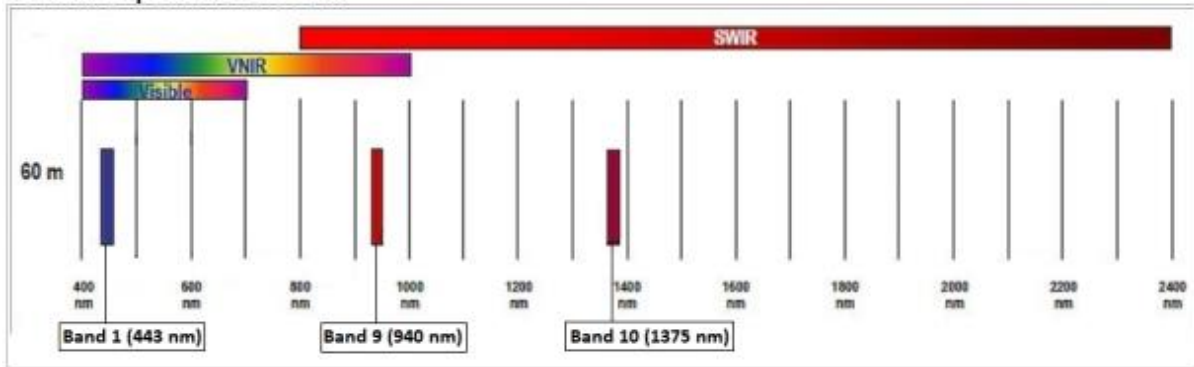
Figure 11: SENTINEL-2 60 m spatial resolution bands: B1 (443 nm), B9 (940 nm) and B10 (1375 nm)

Source: https://earth.esa.int/web/sentinel/user-guides/sentinel-2-msi/resolutions/spatial

3.2 Software Used

Different software that came in use within the time frame of this research with their respective uses are stated below:

a. Google Earth Pro:

Initially, this software was used for visualization of study area. Later, it was used to create a series of ground truth points for accuracy assessment with reference to the field maps.

b. ArcGIS Version 10.6

This software proved to be of vital importance when performing object-oriented classification via machine learning and for generation of series of maps. Most importantly, this software was used to provide training samples to the Full Lambda Schedule (FLS) image segmentation for further classification.

c. Earth Resources Data Analysis System (ERDAS) Imagine 2015 and 2018

The overall processing of the images as well as their correction, accuracy assessment and majority of machine learning was performed using this software. For image classification of Landsat 5 TM imagery, ERDAS Imagine 2015 was used since 2018 kept crashing while working with signature editor. ERDAS Imagine 2018 was used for classifying ALOS-1 PALSAR imagery using machine learning since machine learning operators are only available on ERDAS Imagine 2018.

3.3 Creating Area of Interest (AOI)

AOI can be referred to as the region within the image that defines user's extent of study. After acquiring and carefully observing both Landsat and ALOS images, a certain area was selected as the study area for this research. Using create feature tool in ArcMap, a polygon was drawn on top of ALOS image that represented the boundary of area of study and saved in a form of shapefile (Figure 2). After that, the polygon shapefile was introduced on ERDAS Imagine where was later converted to an AOI.

3.4 Image Sub-setting

Normally, sub-setting can be considered as the process which helps to retrieve only the specified area of interest form a larger file (Almeida-Filho et al., 2005, Irons et al., 2012, Margono et al., 2012). Image sub-setting was done on both Landsat and ALOS image since it contained larger volume of extraneous data. The importance of sub-setting an image is that it also increases the processing speed for the image because of smaller amount of data (Irons et al., 2012). The same images for both Landsat and ALOS obtained after sub-setting was used in all operations throughout the research.

3.5 Image Pre-processing for Landsat 5 TM

Once the image was viewed in ERDAS Imagine, some cloud like feature with white tone was seen dominating the majority area of the image. It was quite interesting because even after atmospheric correction, the presence of cloud could be seen in the image. Cloud QA band was taken as a reference to confirm the presence of cloud. After visualizing and analysing the cloud QA band, it was confirmed that the white toned feature was in fact the haze (aerosols) not cloud.

3.5.1 Haze Reduction

Haze and cloud are the major problems in optical remote sensing (Kaufman and Sendra, 1988). They not only cover the objects that are being sensed but also, they create alteration on the spectral signature. So, reducing these features is a major priority. As the optical thickness of haze is not that high, the features under the haze are still recognizable.

Many techniques have been devised over the years in an attempt to remove haze (Crist and Cicone, 1984, Kaufman and Sendra, 1988, Kauth and Thomas, 1976, Liang et al., 2001, Makarau et al., 2014).

31

There are three major categories under which all the derived methods are contained- dark object subtraction (DOS) (Kaufman and Sendra, 1988, Makarau et al., 2014), frequency filtering (Du et al., 2002, Shen et al., 2014) and transformation based approaches (Moro and Halounova, 2007, Shen et al., 2014, Zhang et al., 2002).

DOS is basically performed on the images with higher spatial resolution since DOS requires relatively large number of dark pixels without having any conflict with brighter targets (Kaufman and Sendra, 1988). The disadvantage of DOS is that it is not feasible to apply this algorithm on the image that has larger areas of brighter surfaces (Makarau et al., 2014).

Frequency filtering works on spatial frequency domain certainly not on spatial domain (Du et al., 2002). It operates on the principle which assumes that the area occupied by haze has a relatively lower frequency while comparing with the ground reflectance pattern (Kauth and Thomas, 1976). There are two approaches- wavelet decomposition and homomorphic filter for haze removal. The major problem with frequency filtering is to find the cut-off frequency (Moro and Halounova, 2007). In order to find the cut-off frequency, Du et al., (2002) tried using a reference image with no haze for the same hazy area and tried separating the frequencies between haze and ground surfaces. Nevertheless, the requirement of reference image limited the application of wavelet decomposition. Another study by Shen et al., (2004) suggests using an image having clear-sky for cut-off frequency determination. Both the strategies by Du et al., (2002) and Shen et al., (2004) failed to understand and clarify the confusion that is created in between land surface with lower frequency (water, forest) and spatial frequencies of haze.

With the reference that the fourth component of TCT contains the majority of haze information, this became the foundation for development of Transformation based approaches for haze diagnostic (Kauth and Thomas, 1976). Initially, the digital number (DN) of Landsat TM image is simulated which then reveals the atmospheric conditions and derives the 4th parameter of TCT. The 4th parameter of TCT is calculated by the combining all 6 reflective Landsat 4 or 5 TM bands.

For Landsat 5 TM, the equation for haze reduction is:

$$\text{TM}_{\text{Dehaze}} = \begin{bmatrix} TM1 \\ TM2 \\ TM3 \\ TM4 \\ TM5 \\ TM7 \end{bmatrix} - \begin{bmatrix} 1.88 \\ 0.89 \\ 1.02 \\ 0.85 \\ 1.40 \\ 0.71 \end{bmatrix} * \text{TC}_4 \qquad \text{Equation (1)}$$

$$= \text{Matrix}_A - (\text{Matrix}_B * \text{TC}_4) \qquad \text{Equation (2)}$$

In equation (2), Matrix$_A$ is the average wavelength values of all the bands respectively, Matrix$_B$ is the value of coefficients of TCT in each spectral bands and TC$_4$ is the value of 4th component of TCT which is calculated through equation (3):

$$TC4 = 0.846 * TM1 - 0.073 * TM2 - 0.46 * TM3 - 0.0032 * TM4 - 0.049 * TM5 + 0.0119 * TM7 + 0.7879 \qquad \textbf{Equation (3)}$$

According to Kong et al., (2011), the relationship between the haze and the Landsat TM data is always linear and is revealed by the scatter plot between values of Digital Number in each of the spectral bands and corresponding value of 4th component of TCT.

Using Haze Reduction tool on ERDAS Imagine, Landsat 5 TM image was dehazed. This tool uses Tasseled Cap Transformation for haze removal (Equation 1). The inbuilt model of TM Dehaze was edited so as to change the input selection to Landsat 5. The result of haze reduction showed some promising outcome yet failed to fully remove all the haze from the entire scene. Guindon and Zhang (2002) concluded that majority of algorithms (pixel-based classifiers) that classify images don't need absolute radiometric calibration therefore there is flexibility in the result of haze reduction. Figure 12 illustrates the model that was used to dehaze the Landsat image.
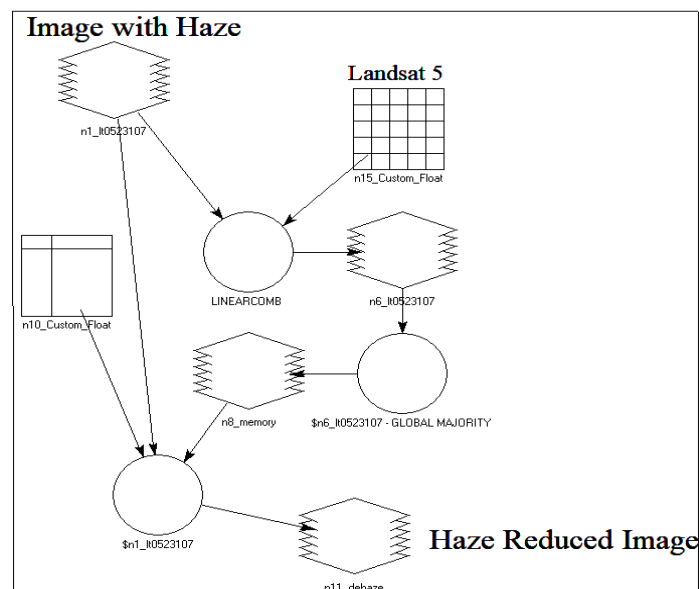
Figure 12: Model used for Haze Reduction

33

3.6 Image Pre-processing for ALOS-1 PALSAR

The ALOS-1 PALSAR data when obtained was in SLC data format in slant range geometry and had not been multi-looked. Range and azimuth were also compressed. The raw data had no map projection, no image direction, no geodetic coordinate, unknown pixel spacing, distorted geometry and scene shift of -5 to 4 pixels (Dong et al., 2014). Since it was raw data, conversion was required to convert it into an image file. The tool Import Data was used while selecting the data format to ALOS PalsAR-2 (JAXA CEOS) (Direct Read). Input raw file had an extension of *.1_a which was converted into an .img file. The metadata of ALOS imagery is shown in figure 13.


```
SAR metadata parameters for original SAR image:

sensor type:                    SAR (Synthetic Aperture Radar)
orbit direction:                Ascending
data type:                      Complex (Magnitude, Phase)
acquisition mode:               Stripmap
coordinate system type:         Fixed Body or Earth Rotating Frame
year:                           2007
month:                          9
day:                            24
day of year:                    267
number of samples:              4640 samples
number of lines:                18432 lines
first point time:               11852.085000 seconds
original first point time:      11852.085000 seconds
time interval:                  9.921000 seconds
original time interval:         9.921000 seconds
image start time:               11852.085000 seconds
image end time:                 11871.927000 seconds
image duration:                 19.842000 seconds
spheroid semi major axis:       6378137.000000 meters
spheroid semi minor axis:       6356752.314100 meters
target height:                  0.000000 meters
look side:                      90.000000 degrees
local incidence angle:          38.876000 degrees
wavelength:                     0.236057 meters
range sampling frequency:       16000000.000000 Hz
azimuth sampling frequency:     2141.327623 Hz
```

Figure 13: Metadata of ALOS-1 PALSAR imagery

3.6.1 Image Ortho-rectification

One of the most important processes of SAR image pre-processing is Geometric Correction (Toutin, 2004). As side-looking image mode has been adopted by SAR, it tends to have much bigger side-looking angle when compared with optical image. Due to this mode, there exists greater amount of geometric distortion in the SAR image (Evans et al., 2010). So, it is very important to remove or reduce the degree of distortion caused by geometry on SAR and create an ortho-image. Image ortho-rectification in case of SAR is done by assigning all the pixels to their respective location (geodetic latitude and geodetic longitude) with reference to the surface of the earth (Huang et al., 2004, Toutin, 2004). Ortho-rectification treats the slant-range geometry of the radar imagery by converting it into a true ground range geometry which creates a planimetrically correct image with a fixed scale (Evans et

al., 2010, Shimada et al., 2009). Figure 14 shows characteristics of Side looking Airborne Radar (SLAR) and iFigure 15 provides an insight to actual relation between slant range and ground range geometry. Since ALOS PALSAR data is an SLC product, no geo-location data was available for automatic geometric correction.

Ortho-rectification to radar image was applied in ERDAS Imagine using the tool Ortho Radar Classic. The algorithm that performs ortho-correction to SAR Image requires a Digital Elevation Model (DEM) to perform height correction. In this case, the inbuilt elevation library of ERDAS was used to provide the height data to the algorithm. Orthorectify SAR Image was used as the rectification parameters. Once the general information was provided, new map projection was given to the data as per the study area where projection type was set to UTM Zone 20 South with spheroid and datum specified as WGS 84. After the projection was defined, the values for sparse map parameters- range sampling factor and azimuth sampling factor was set so that the grid calculated would be tighter resulting in a lesser amount of error (Rauste et al., 2007). The value of sparse map parameters tends to alter the pure information about the density of pixels hence sometimes taking a default value might also be an ideal choice (Huang et al., 2004, Rauste et al., 2007, Shimada et al., 2009). The default sampling factor is normally used since the resampling process executes faster as the exact solution for all the pixels need not be calculated by the model. (Evans et al., 2010, Rauste et al., 2007). Nearest Neighbor algorithm was used as a sampling algorithm to preserve DN values from the original image.
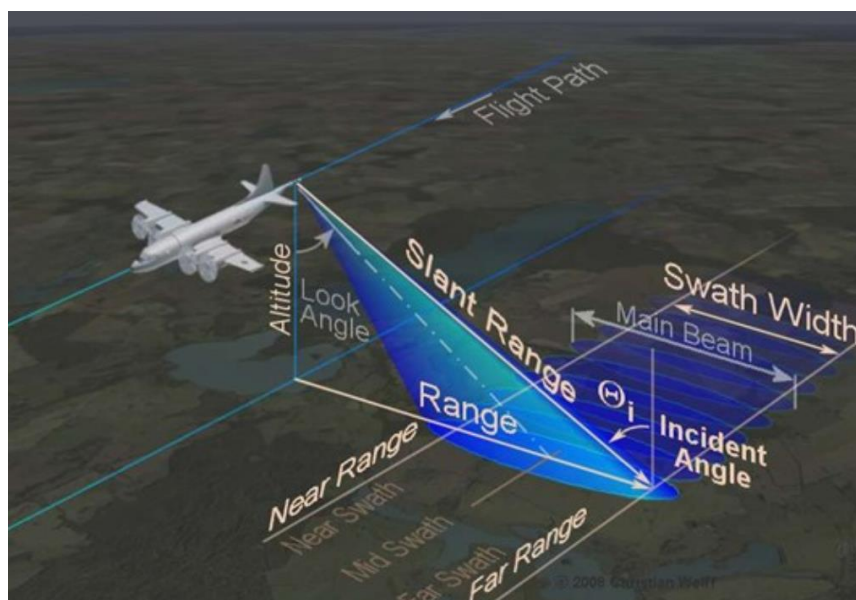
Figure 14: Side Looking Airborne Radar

(Source: https://slideplayer.com/slide/4682402/)
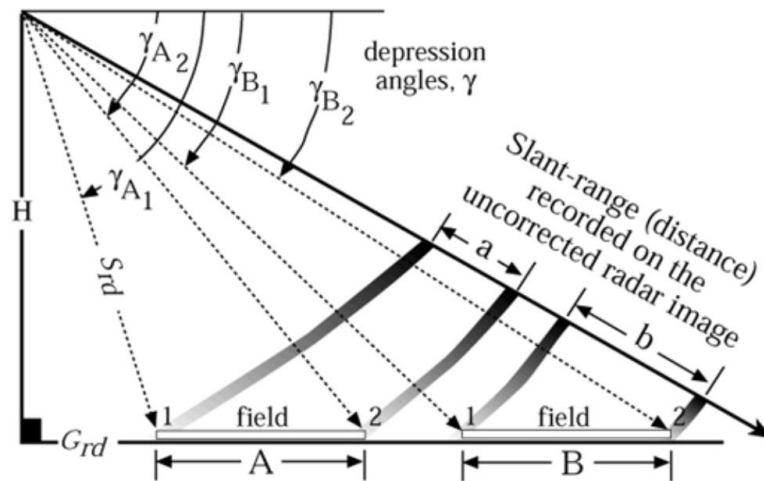
Figure 15: Slant range and Ground range display

(Source: https://slideplayer.com/slide/4682402/)

3.6.2 Speckle Removal

Speckle generally referred as speckle noise is very common for all the imaging systems which uses a coherent mechanism for image acquiring and to all the SAR images without any exception (Bamler, 2000). Speckle is induced by the fluctuations in the phase of returning electromagnetic signals (Saevarsson et al., 2004). The nature of speckle is multiplicative which induces changes in the intensity values of all the features residing in a scene (Domg and Milne, 2001). As the pixels are not fully developed in case of point scatters or few scatters being covered by pixels, the multiplicative model is not relevant to eliminate the speckle (Lopes et al., 1990b). SAR has always been utilized as one of the most efficient data in the fields of remote sensing however the presence of speckle has often reduced this potential by degrading the appearance as well as the quality of SAR data (Ali et al., 2008, Lee and Pottier, 2009). For this vary reason, speckle removal now has become an important operation in radar remote sensing.

A series of adaptive filters have been developed in order to reduce speckle while preserving the radiometric and textural information of the SAR image (Bamler, 2000). The adaptive filters that are based on the spatial domain rather than frequency domain filters are widely popular for speckle removal (Sumantyo and Amini, 2008). Some of the popular adaptive filters for speckle removal include Gamma-Map, Frost, Lee-sigma and Lee filters (Sumantyo and Amini, 2008).

Gamma-map filter was developed by Lopes et al. (1990a; 1990b) which is an adapted version of maximum a posterior (MAP). It supresses the speckle by assuming that the speckle follows a gamma distribution. Frost and Lee filters are built on the basis of multiplicative speckle model. They tend to follow local statistics for effective edges and features preservation (Frost et al., 1982, Lee, 1980). Lee-sigma filter is rather very simple in concept rather very effective for replacing Lee filter that relies on the sigma probability of the image noise having a Gaussian distribution (Lee, 1980). Frost, Lee and Lee-sigma filters suppresses the speckle by assuming that the speckle follows a Gaussian distribution (Lopes et al., 1990a, Lopes et al., 1990b). Sumantyo and Amini (2008) performed a quantitative and qualitative operation on Gamma-Map, Frost, Lee-sigma and Lee filters for ALOS PALSAR and concluded that Gamma-Map was found to be more effective in speckle suppression which also preserved the texture as well as spatial resolution of the SAR image.

Speckle was removed using Radar Speckle Suppression tool under RADAR utilities in ERDAS Imagine. Initially, keeping all the parameters to default, the coefficient of variation was calculated which was achieved to have a value of 0.349263. After achieving the value for coefficient of variation, speckle reduction was performed using Gamma-Map as the suppression filter with moving window of 5*5.

3.6.3 Layer Sub-setting

Image sub-setting is the same that has been described in section 3.4 but instead of breaking the larger area of a scene into smaller file using AOI, spectral sub-setting is performed on a scene where breakage occurs on the spectral level that creates another scene with similar spatial extent but with a smaller number of spectral bands. As the ALOS imagery was in fact a SLC data with dual polarization, there were 4 layers in the image where Layer 1 was the magnitude value of HH polarization, Layer 2 was the phase data of HH polarization, Layer 3 was the magnitude value of HV polarization and Layer 4 was the phase data of HV polarization. Since there was no processing of data relating to interferometry, the phase information was dropped out from the ALOS image. The layer sub-setting was performed by keeping only the magnitude information for HH and HV polarization.

3.6.4 Geometric Correction

The outcome of Image ortho-rectification still resulted in some distortion of the geometry of the ALOS image. SAR Geocoded Ellipsoid Corrected (GEC) imagery is the imagery that is a result of geometric correction i.e. the ground-range corrected imagery (Bamler, 2000, Shimada et al., 2009). This means

that the SAR GEC image even after being corrected in a constant ellipsoid height, results in a rough geocoded reference for those users that are interested in the use of accurate absolute localization programs like DEM generation and 'ortho-image' creation (Bamler, 2000). This has decreased the usefulness of SAR GEC image. Zhang et al., (2013), believed that the capacity or the usefulness of the SAR GEC imagery can be maintained by performing geometric correction to the image using corresponding geometric model.

Further geometric correction was thus applied to the ALOS imagery using multipoint geometric correction tool. The tool opens a set of options for selection of geometric model. Polynomial model was selected as the geometric model. The geometric distorted image was loaded as an input file and sentinel 2a imagery of year 2016 was used as a reference image because of its availability and spatial resolution being higher than that of Landsat. To perform geometric correction certain amount of ground data was necessary so 39 points were selected on the ALOS image and the reference location for those points were marked on input image. After checking each point, some of the points needed to be discarded so finally 28 number of ground points were used for geometric correction.
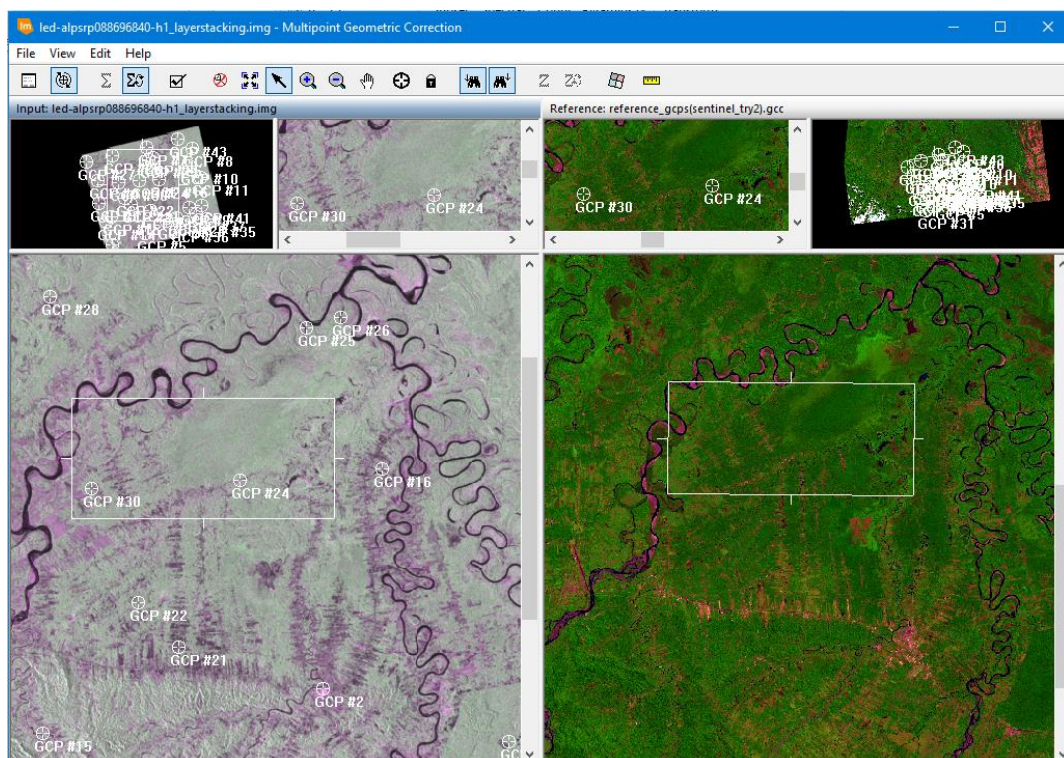
Figure 16: Geometric correction of ALOS image (left) with Sentinel 2a as a reference image (right)

3.7 Digital Image Processing of Landsat 5 TM

Classification on a remotely sensed data is always a challenge as wide range of factors should be taken into consideration (Richards, 2013). The result of image classification solely depends on the accuracy of training samples, feature extraction method and appropriate image classification algorithm (Lu and Weng, 2007). These all factors are twinned according to user's choice of study area and the skill of an analyst.

As the imagery was pre-processed, it was ready to undergo image classification. The training samples were taken only on the area where there was no presence of haze and separate training samples were taken for the haze inflicting area. Supervised classification using Maximum Classification classifier is used for Landsat since this same technique has been used for classification Landsat images in this study area for long period of time and this research is based on the accuracy comparison between the Landsat (following previous trend of classification) and RADAR.

3.7.1 Supervised Image Classification

Supervised Image classification is one of the crucial approach towards the feature extraction information in a remotely sensed data (Richards, 2013). It is the most common image classification technique which is dependent upon the samples of the information classes of the interest in the image (Pacheco, 2002). These samples are known as training samples. After the completion of gathering the training samples, these samples are then used by the classified to attach labels on all the pixels of the images.

One of the mostly used supervised classifier is maximum likelihood classifier (MLC) which assumes that multivariate normal distribution can define each spectral class in the image (Malingreau, 1991, Rees and Pellika, 2010, Richards, 2013). To assign pixels to their respective classes, MLC uses the mean image vector and multivariate spread values of each classes (Steininger et al., 2001). In case of classifying the overlapping signatures, MLC uses a statistical decision criterion which ensures that these pixels are be assigned to that classes having the high probability value (Rees and Pellika, 2010). It is also considered to be a more accurate classifier than parallelepiped, but lacks in the speed for classification (Richards, 2013). Parallelepiped is much faster since it does not classify all the pixels of image rather only those pixels that matches the spectral value of the provided samples. The accuracy of MLC classifier is the measure of correct estimation of the mean vector and the covariance matrix in

each spectral classes which assumes that the input data and the signature selected tend to follow the Gaussian distribution (Joseph, 2005, Richards, 2013, Donoghue, 2000).

Once the image was loaded on ERDAS Imagine, Region Grow properties tool was used to capture the signatures from the training samples by adjusting the spectral Euclidian distance. The signatures were not taken in a random manner but using inquire cursor, by selecting a single pixel within the training area. Signature editor tool was used to record and manage the training samples for all the designated classes. As MLC is a parametric classifier, the theory of Lillesand, Kiefer and Chipman (2004) suggests that the minimum number of pixels per signature should at least be 'a + 1' where a stands for number of spectral bands. As the Landsat 5 TM had 6 bands (Table 4) the minimum number of pixels per signature was maintained by having at least 7 pixels. After the collection of training samples, these samples were then refined by viewing the effects of collected samples on the image using image alarm tool which gave the clear idea of either to add new signatures to the unoccupied features or to remove the overlapping signatures. This was a visual process. After visual correction, the confirmation to the refinement process could only be made if proven using statistics. Jefferies Matusita (JM) distance (described in section 3.9.2) was calculated between samples of classes to check the separability between signatures which indicated whether the selected samples could combine with each other or treated as different classes. Once the process of refining was completed, classification was commenced.

Two different supervised classifications were performed - 1. By taking all the classes in account and 2. By focusing only on Old Forest features. The list of classes that were used in this classifications are presented in Table 6 and 7.

Table 6: Classes used for extraction of spectral signatures (1st classification)

Class Name	Class Number
Regrowth	1
Banana	2
Bare Land	3
Bare Land and Grass	4
Pasture	5
Old Forest	6
Water	7

Table 7: Classes used for extraction of spectral signatures (2nd classification)

Class Name	Class Number
Old Forest	1
Others	2

Once the classification is completed, there exists the case of misclassification and no classification. Misclassification is that where pixels of one class is basically assigned to another and no classification is the condition which occurs when there is relatively lesser training sample for any specific feature in the image. Along with the classification, a Chi Square distance file was also created which is a gray scale image representing Chi Square distance. It is a measure of accuracy of classified image where least accurately classified pixels are given a brighter tone and accurately classified pixels are given a darker tone.

After visually assessing the classification output, a conclusion was drawn stating that the classification from supervised classification needed refining. It was accomplished by discovering the pixels that had a probability of being classified incorrectly in the new thematic layer. This process screened out those pixels that had been misclassified by setting a chi-square distance threshold.

3.8 Image Post-processing

3.8.1 Recode

After supervised classification, the output image was represented by 130 different signatures which had not been merged for classification. Recode tool was used which allowed to specify new class number to the disbanded signatures (Donoghue, 2000, Congalton, 1991a). The class number was assigned for all the signatures correspondence to their respective classes (Table 6, Table 7). It helped by combining all the signatures which resulted in a new image having only 6 distinct feature classes.

3.8.2 Majority Filter

It is very likely for a classifier to result in the classification of mixed pixels. These mixed pixels are generally caused by the variability in spectral values over small spatial areas. Majority filtering is a process of smoothing a classified result by replacing the value of the center pixel of a neighborhood

window by the majority value within the neighborhood window (Dong et al., 2014, Jha et al., 2005). Bigger the size of neighborhood windows results in much smoother image. In this research, neighborhood functions were used with function definition selected as Majority. All neighborhood definition 3 * 3, 5 * 5 and 7 * 7 were used to see the change in the classified image. At last, the output from using 3 * 3 was accepted as the final image since the output of 5 * 5 and 7 * 7 were overly smooth.

3.8.3 Clump and Sieve

Clump and Sieve are also smoothing operations and are widely used for classified images. Clump operation was applied to the output raster from majority filtering. This operation initially converted the class values of a certain theme in a raster into the polygon that represented the contiguous group of pixels (Joseph, 2005, Richards, 2013). Then, sieve operation used the output of clump and removed those contiguous groups of pixels which were below the user defined tolerance (Richards, 2013). The value of tolerance was 2 pixels, so sieve removed all the clumps below the minimum size.

3.9 Digital Image Processing of ALOS-1 PALSAR

3.9.1 Supervised Image Classification

Supervised Image Classification has already been discussed on section 3.4.1. Since, ALOS-1 PALSAR is a single wavelength SAR, there are only 2 bands representing the scene- magnitude of HH and magnitude of HV. All the process involved during supervised classification are same as Landsat, the only difference being the classifier. For RADAR, non- parametric rule, parallelepiped classifier was used for image classification since there was no guarantee that pixel-based classifier could be the ideal solution for classifying RADAR image.. Parallelepiped classification was chosen because it is faster than MLC and it only classifies the pixel for which spectral classes have been specified. If the parallelepiped classifier had shown some promising result for classifying the RADAR imagery, MLC algorithm would have been selected as the supervised image classification algorithm. Two classification were performed – one with only water and clear-cut class and another with water, clear-cut and 4 different objects that represented forest. As the RADAR imagery is composed of backscatter pulses rather than spectral value, the components or pixel representing the features have been referred as objects.

3.9.2 Separability Calculation using Jefferies-Matusita (JM) Distance

Signature separability is a measure of separability between the training samples which is based on the value of statistical distance between training samples (Donoghue, 2000). It indicates how similar or different the spectral signatures of the samples are from one another. It can be measured for any grouping of signatures which are selected for classification. It provides the option to discard the signature which are not that important in classification. The distance value is used to distinguish the signatures from one another. Basically, there are four distance measurement techniques – 1. Euclidean 2. Divergence 3. Transformed Divergence and 4. Jefferies-Matusita Distance. In their research, Kavzonglu and Mather (2000), compared the different feature classification techniques – divergence, JM distance, transformed divergence and Bhattarcharyya distance and concluded that JM distance yielded the best result among all other techniques with overall accuracy of 91.20 % followed by divergence with the overall accuracy of 90.43%.

Mathematically, JM distance is measured using equation 4.

$$JM = sqrt(2\left(1 - e^{-\text{alpha}}\right))\qquad\qquad \text{Equation 4}$$

Here, alpha is the bhattacharya distance. The upper bound and lower bound of JM distance are 1.414 (square root 2) and 0 respectively.

After calculating JM Distance for all the signatures taken, an analysis was done that led to the conclusion that there was low potential of pixel-based classification being effective in classifying RADAR imagery.

3.9.3   Object Oriented Classification via Machine Learning

Object-oriented classification (OOC) techniques are very common and preferred while working with images having higher resolution (Blaschke and sensing, 2010). These techniques are based on image segmentation. OOC are useful even for extracting various thematic information from the image (Benz et al., 2004). OOC is very different from pixel-based approaches since OOC are solely dependent upon the segments of the objects, not single pixel (Haila, 2002). Objects are way powerful than pixels since objects can define the corresponding physical features of all the objects inside the imagery with respect to their radiometric properties (Shape, Size, Spectral and Texture).

The overall computation using OOC is done in two major steps –

1. Segmentation of the image where vector polygons are created from raster image by using the radiometric information of the image (spectral, texture, shape and size).
2. Assigning the objects to their specified classes according to the attribute values assigned while creating training samples.

Once the segmentation was done, the output was a raster. The output raster was then converted to vector format (vector polygons) using raster to shapefile tool in ERDAS that resulted in 77,700 polygons. The training data was created from the segmented vector polygons in ArcMap. Two new fields - class number and class name were added to the raster data. The new fields were manually filled according to the features represented by the training samples which was identical to the values in Table 6. Then, 2 new set of attributes – mean and standard deviation were calculated for training samples by creating a model in ERDAS Imagine. These set of attributes were later used during classification for assigning the objects to their respective classes. Same set of attributes were calculated for the segmented vector polygons as well.

There were 5 supervised machine learning algorithms under OOC in ERDAS – 1. Initialize CART 2. Initialize K-Nearest Neighbors 3. Initialize Naïve Bayes (NB) 4. Initialize Random Forest (RF) 5. Initialize SVM. Blaschke and Sensing (2010) performed object-based classification using various algorithm and shared his results showing the usefulness of each algorithms and drew the conclusion that RF classification has a higher average predictive accuracy than other classifier despite having comparative slower training speed (Table 8). Novack et al., (2011) compared machine learning approaches for the classification of urban land cover which resulted in RF with highest overall accuracy of 95% over other classifiers. Amongst the five available supervised machine learning algorithms, Initialize RF was selected as the main classifier in this research.

Table 8: The table of comparison between different classification approaches created by Blaschke and sensing (2010)

Algorithm	Problem Type	Results interpretable by you?	Easy to explain algorithm to others?	Average predictive accuracy	Training speed
KNN	Either	Yes	Yes	Lower	Fast
Linear regression	Regression	Yes	Yes	Lower	Fast

Logistic regression	Classification	Somewhat	Somewhat	Lower	Fast
Naive Bayes	Classification	Somewhat	Somewhat	Lower	Fast (excluding feature extraction)
Decision trees	Either	Somewhat	Somewhat	Lower	Fast
Random Forests	Either	A little	No	Higher	Slow
AdaBoost	Either	A little	No	Higher	Slow
Neural networks	Either	No	No	Higher	Slow

RF is one of the easiest and flexible machine learning algorithms which most of the time produces promising result (Blaschke and sensing, 2010). The major reason behind the popularity of RF classifier is its simplicity and dual functionality – preferable for both regression analysis and image classification (Benz et al., 2004, Haila, 2002). So, as the classification algorithm was selected for this study, RF algorithm was then trained using the training samples. This process was also performed by creating a model. The result of training the classifier is known as machine intellect which is basically a trained machine learning algorithm. With machine intellect being created, final step of actual classification was performed to the unclassified vector polygon that were created by segmentation process. The result of classification was a vector layer where all the polygons were assigned to their respective class number.

The model used for assigning the attributes (mean and standard deviation) to the unclassified segments and training sample is shown in Figure 17.
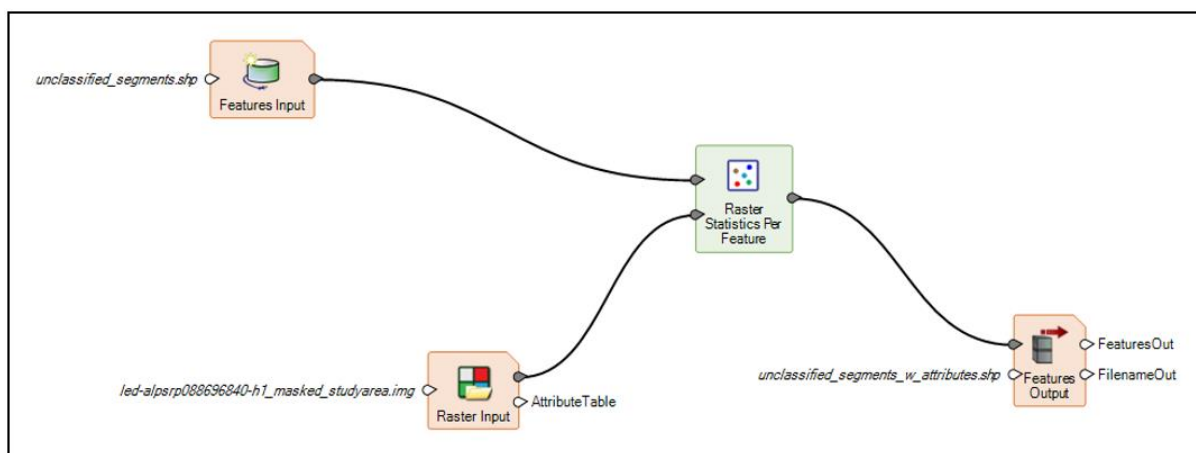
Figure 17: Model used for assigning attributes to training samples and unclassified segments

The model used for training the machine learning algorithm is shown in Figure 18.
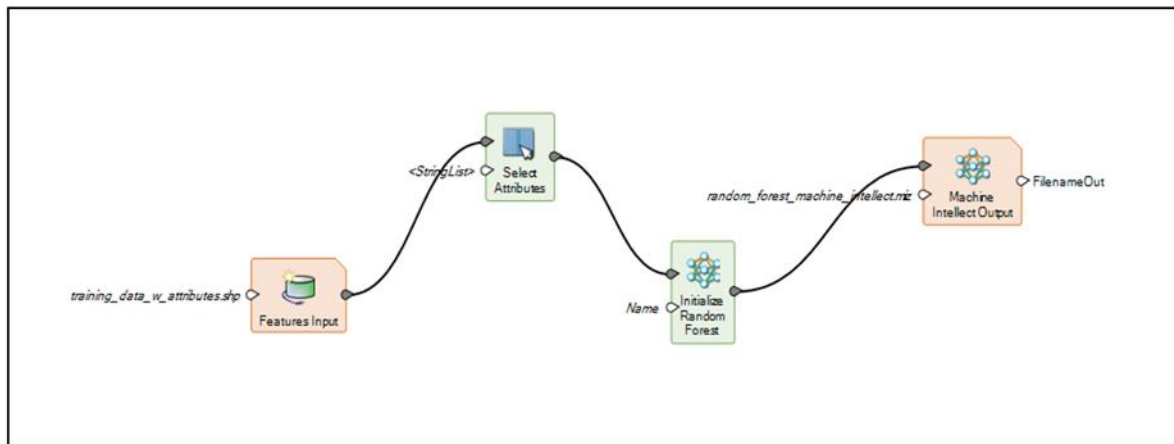
Figure 18: Model used for training supervised machine learning algorithm (Initialize Random Forest)

The model used for actual classification using machine intellect is shown in Figure 19.
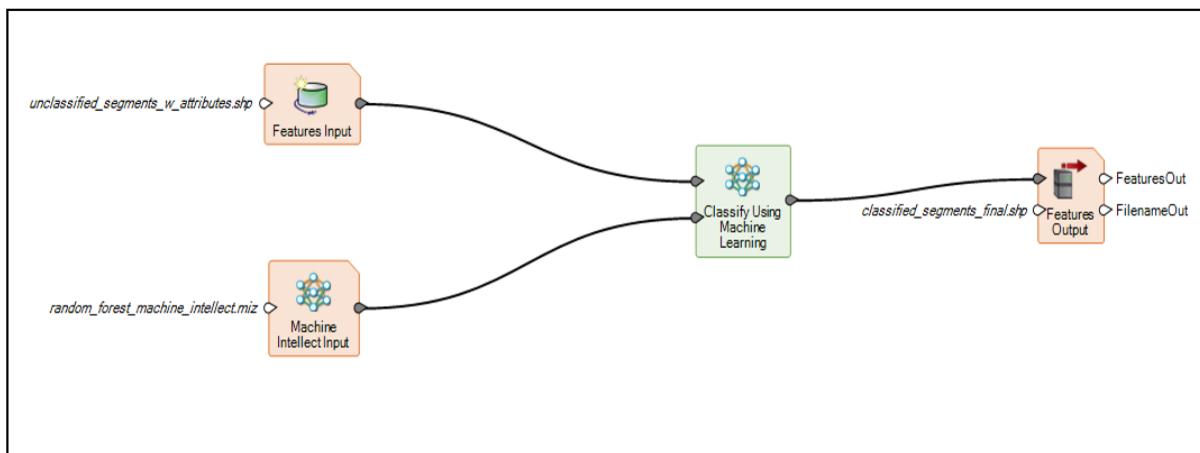
Figure 19: Model used for classifying unclassified segments using classify operator.

3.10   Post-Classification Smoothing

After the classification of ALOS-1 PALSAR data using OOC, the presence of scattered objects was seen all round the scene. To refine the classified dataset, removal of those objects was the primary concern. Since OOC classification was a vector dataset, the process of Clump and Sieve was not applicable in this scenario. But there existed some operations which corresponds the

use of Clump and Sieve for vector file and they were – 1. Eliminate 2. Dissolve. Both the post-classification smoothing operations were performed in ArcMap.

3.10.1 Eliminate

Eliminate tool helps remove the objects that are below the threshold value as per the user's requirement (Walter and sensing, 2004). In this tool, a threshold value is assigned on a basis of attributes of a polygon. For this research, initially a new field was added to the classified field name 'area' where the area for all the polygons were calculated in hectare. By using select by attribute tool, the polygons with area less than 1 hectare were selected. Eliminate does two things- 1. It merges the user selected polygons with the polygon that share the largest border or area, 2. It removes those polygons that are introduced during executing buffering or overlay operation (Novack et al., 2011). Using this threshold value of 1 hectare, eliminate tool was executed which deleted all the selected objects that resulted in a more unified and smoother classification.

3.10.2 Dissolve

After eliminate operation was performed, the resulting image was still complex, so dissolve operation was performed on the eliminate output to create more simplified coverage. The operation behind Dissolve is that it merges the adjacent features that share the same class value (Novack et al., 2011). The result of Dissolve operation was a smoother polygon file (Appendix C).

3.11 Accuracy Assessment

Accuracy assessment is a method used in order to quantify the reliability of any classified image (Congalton, 1991b, Congalton and Green, 2008). The standard procedure to conduct accuracy assessment is to construct an "error matrix" (Jensen and Lulla, 1987). The rows and columns of the errors matrix which is square in nature represents different classes of land cover from the given classified image (Donoghue, 2000, Joseph, 2005). The rows and columns correspond to the number of classes present in the classified image. In our case there are 7 classes which resulted in an error matric with 7 rows and 7 columns. The counts taken from a sample are filled into the error matrix. The "ground truth" and the classification of the sample matrix should be known. In this case "ground truth "was extracted from Google Earth with reference to the field work conducted by Professor Andrew

Millington. A total of 662 ground truth points was used for accuracy assessment for both Landsat and ALOS PALSAR. All the points were created to match the land use of year 2007 as the fieldwork was also conducted in the same year.

Omission error is defined as a measure of loss of pixels from a class to other class in classification (Congalton, 1991a, Congalton and Green, 2008). Commission is defined as a measure of gain of pixels from another class to the host class (Jensen and Lulla, 1987). Overall Classification Accuracy is the measure of accuracy of the entire classification process and calculated by dividing the sum of number of pure classified pixels for each class by the sum of total number of pixels for each class (Blaschke and sensing, 2010, Congalton, 1991a).

An example of accuracy assessment in shown in Figure 20. The percentage of error of omission is calculated by the percentage ratio of total sample loss in a class to total number of samples during accuracy assessment and similarly, the percentage of error of commission is calculated by the percentage ratio of total sample gain from other classes to total number of samples during accuracy assessment (Figure 20) (Jensen and Lulla, 1987) .

Landsat Accuracy Assessment

Photo/Ground Classes	Landsat Classes				Total Possible	Omissions	Commissions	Mapping Accuracy*
	Corn	Soybeans	Forest	Other				
Corn	25	5	10	3	43	$\frac{18}{43}=42\%$	$\frac{7}{43}=16\%$	$\frac{25}{25+18+7}=50\%$
Soybeans	2	50	6	5	63	$\frac{13}{63}=21\%$	$\frac{11}{63}=17\%$	$\frac{50}{50+13+11}=68\%$
Forest	3	4	60	5	72	$\frac{12}{72}=17\%$	$\frac{18}{72}=25\%$	$\frac{60}{60+12+18}=67\%$
Other	2	2	2	100	106	$\frac{6}{106}=6\%$	$\frac{13}{106}=12\%$	$\frac{100}{100+6+13}=84\%$
Total	32	61	78	113	284			

$$\text{Overall Landsat Classification Accuracy} = \frac{25+50+60+100}{284}=83\%$$

*Mapping Accuracy (MA) for any Class X:

$$MA = \frac{\text{Pixels of } X_{correct}}{\text{Pixels of } X_{correct} + \text{Pixels of } X_{omission} + \text{Pixels of } X_{commission}}$$

Pixels of $X_{omission}$ = All other classes in X Row

Pixels of $X_{commission}$ = All other pixels in X Column

Figure 20: Example of Accuracy Assessment

Source: http://leefoxadvremote.blogspot.com/2014/10/classification-accuracy-assessment.html

Accuracy assessment tool for ERDAS IMAGINE 2015 was used. Firstly, the classified image of Landsat was loaded on to the accuracy assessment tool. Then the ground truth was imported through the user

defined points tool under the edit menu. A text file with respect to the input layout of the accuracy assessment tool was prepared based on the X and Y coordinates and reference class number. This text file was loaded on the accuracy assessment platform. Then using the report tool in the accuracy assessment workspace, an accuracy assessment report was generated which is based on the numerical expression for overall accuracy, producer's accuracy, consumer's accuracy as well as kappa coefficient for each of the classes.

Similarly, for classified image of the ALOS PALSAR, the same procedure was followed. The accuracy assessment report for both of these images were further analysed. The overall accuracy generated through this method gave a brief estimate on how accurate the pixel- based classification for Landsat and Object based classification for ALOS PALSAR were.

CHAPTER FOUR

RESULTS

This chapter incorporates all the results of each method and processes dealt in CHAPTER THREE.

4.1.1 Geo-referenced ground observations

The ground truth that was initially acquired from field work was later converted into a shapefile. In Figure 21, the features represented by the yellow pins are the ground truth and the red polygon is the boundary of the study area which are overlaid on Google Earth.
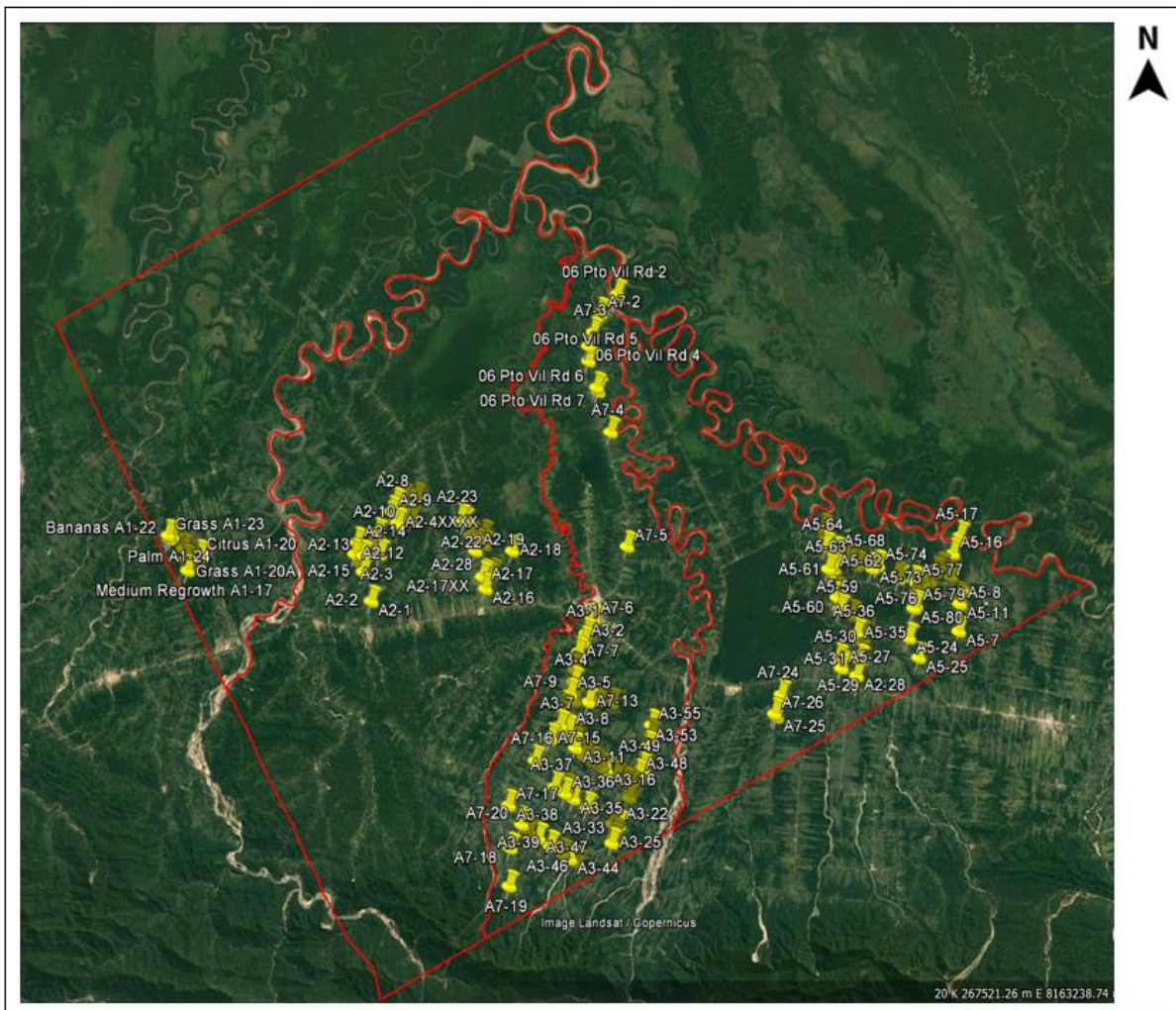
Figure 21: Ground Truth and Boundary of study area overlaid on top of Google Earth Imagery

4.1.2 ALOS-1 PALSAR imagery from Alaskan Satellite Facility (ASF)

The initial raw data obtained from ASF portal was converted to image file. The image in Figure 22 is in slant range geometry.
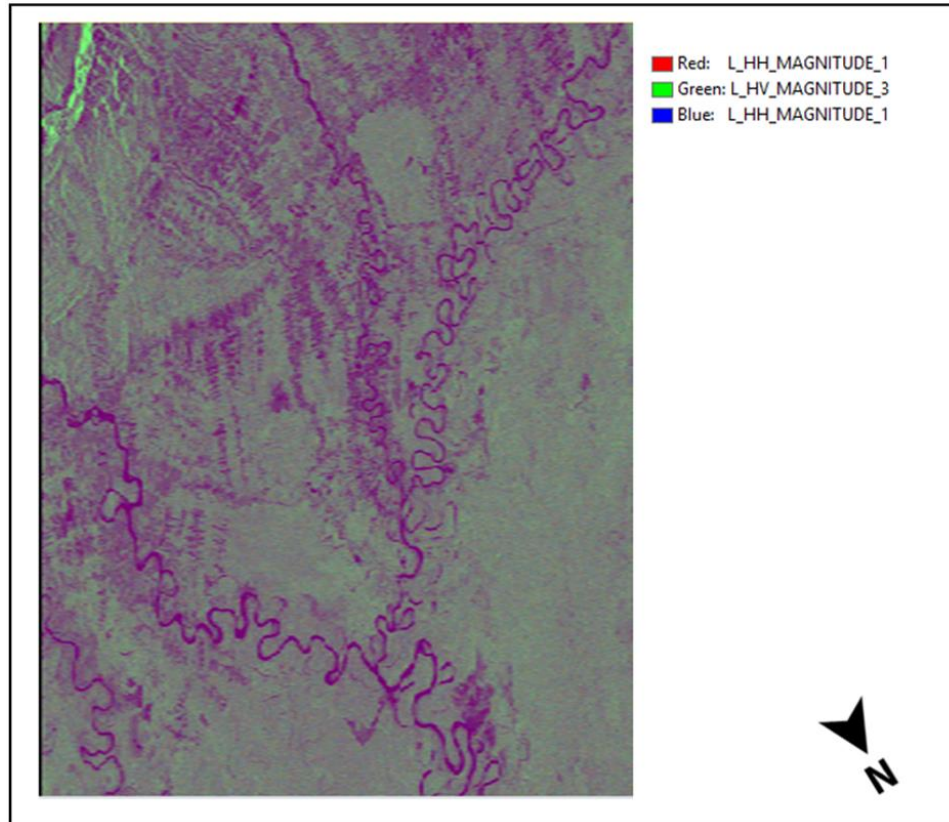
Figure 22: Geometrically distorted Imagery of ALOS PALSAR

4.1.3 Landsat-5 TM imagery of year 2007 (source: United States Geological Survey)

Landsat-5 TM imagery downloaded from USGS was already geometrically and atmospherically correction however in Figure 23, definite patterns of haze can be seen. More dominant hazy area fall towards the southern area of the imagery white are represented by white colour.
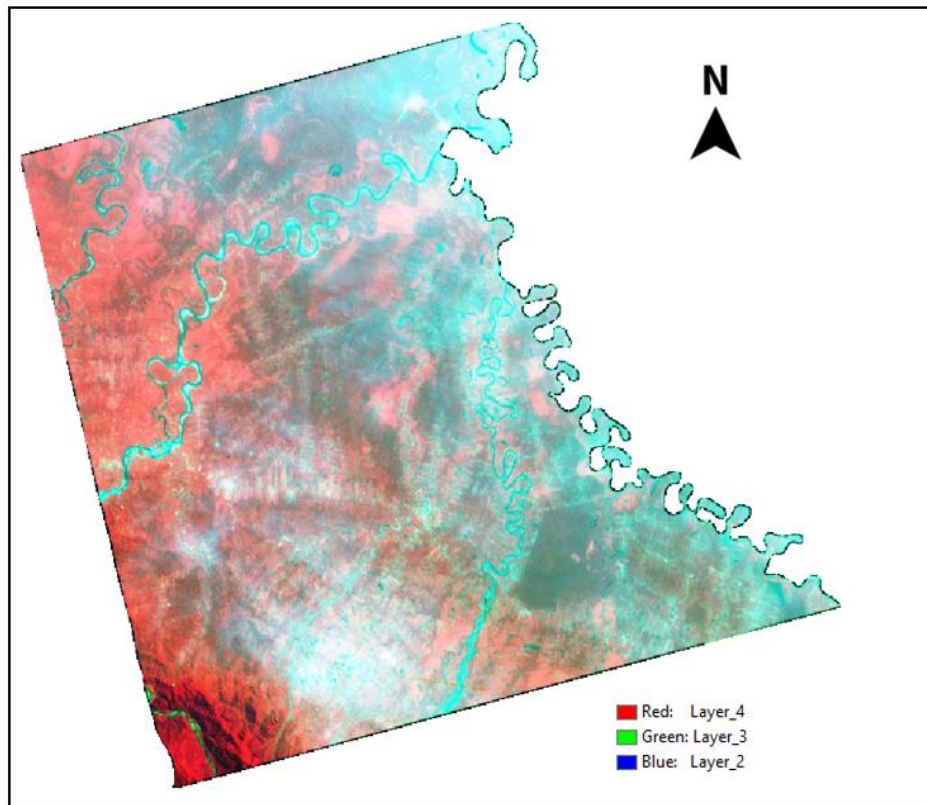
Figure 23: Landsat Image acquired from USGS

4.1.4 Sentinel 2a imagery of year 2016 (source: Copernicus Open Access Hub)

Sentinel 2a image was obtained from Copernicus open access hub and was just used for geometric correction of ALOS imagery (Figure 24).
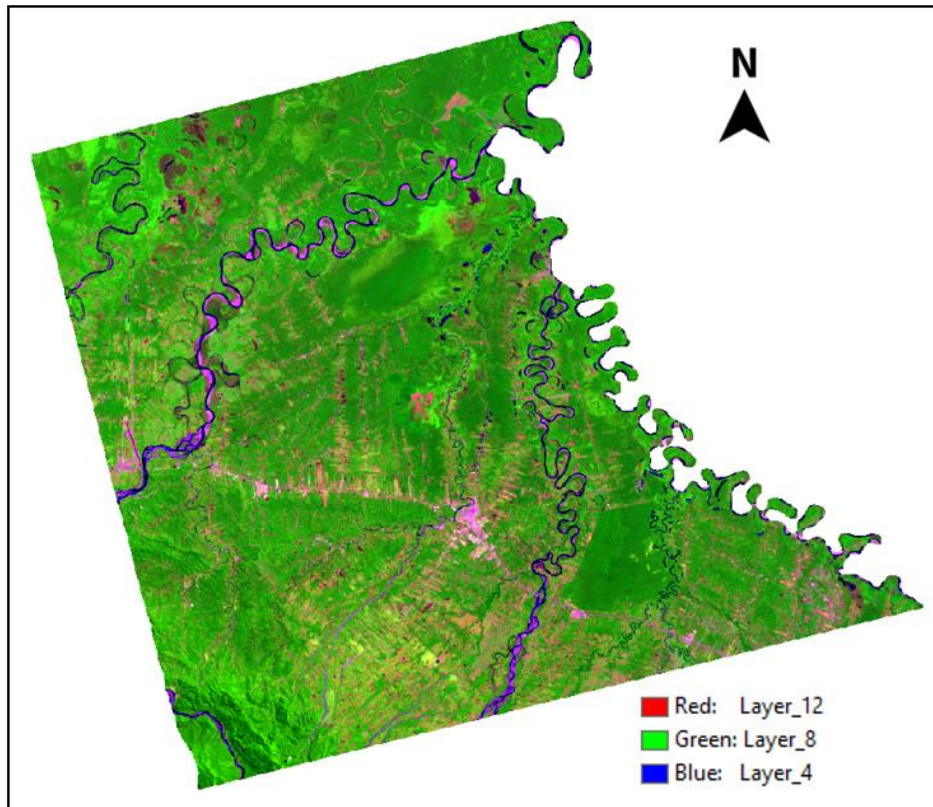
Figure 24: Sentinel 2a image acquired from Copernicus open access hub

4.2 Image Pre-processing for Landsat 5 TM

4.2.1 Haze Reduction

Haze reduction on Landsat 5 TM was done using haze reduction model in ERDAS Imagine. Even after applying haze reduction, there were significant amount of haze in the corrected image which can be seen in Figure 25.
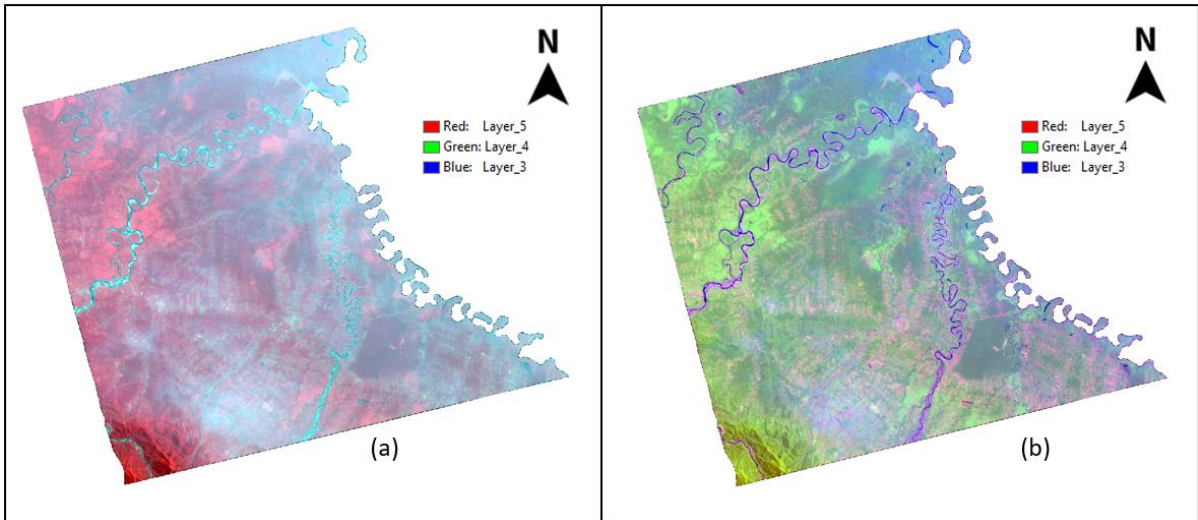
Figure 25: (a) Image before haze reduction and (b) Image after haze reduction

4.3 Image Pre-processing for ALOS-1 PALSAR

4.3.1 Image Ortho-rectification

Image ortho-rectification was performed to correct the geometry of SAR image. Slant range geometry of ALOS was converted to ground range geometry (Figure 26).
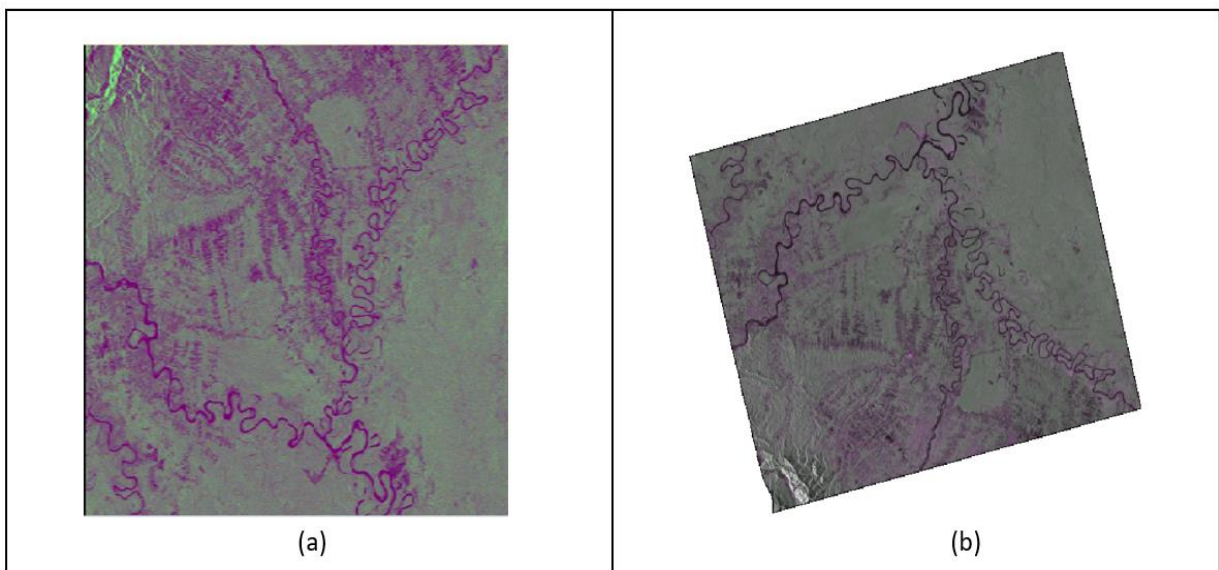
Figure 26: (a) Image with geometric distortion and (b) Image without geometric distortion

4.3.2 Speckle Removal

Speckle suppression was done in order to remove the noise while attempting to preserve radiometric and spatial resolution of the initial image. The result for speckle removal was a smooth and brighter image (Figure 27).
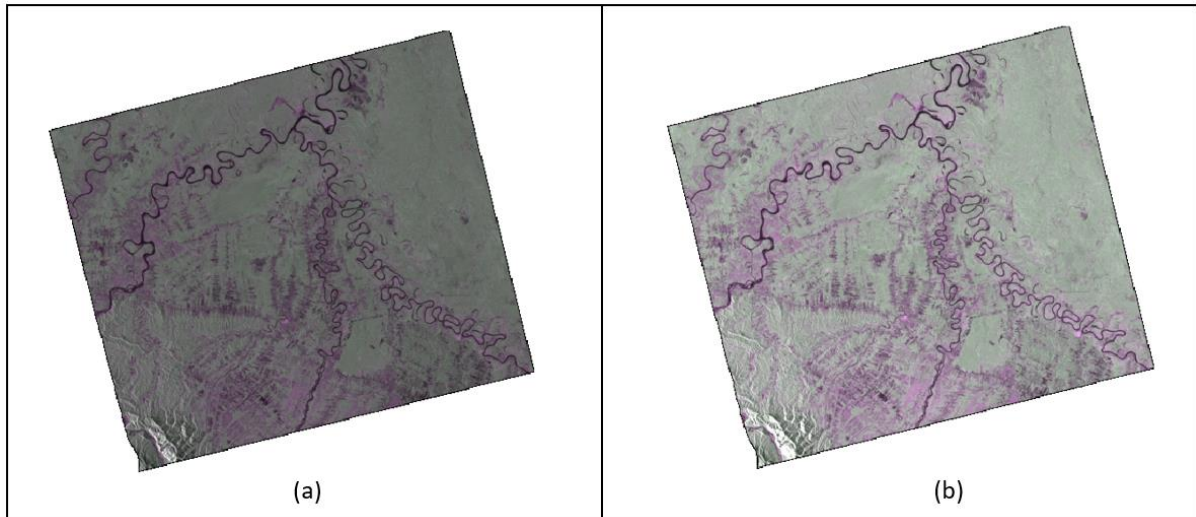
Figure 27: (a) Image with speckle and (b) Image after speckle suppression

In Figure 28, a small area of image was taken where the effect of radar speckle suppression was examined. The image after noise removal appeared brighter and even the smaller features that were dominated by speckle were more easily detectable.
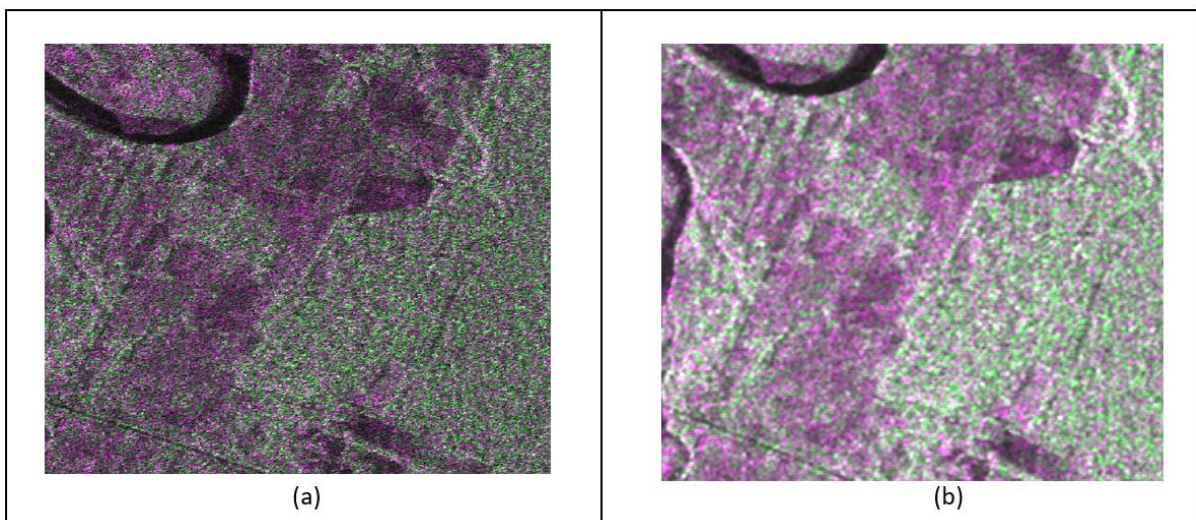
Figure 28 (a) Image with speckle and (b) Image after speckle suppression

4.3.3 Spectral Sub-setting

Spectral subset was done to remove the phase information for both HH and HV polarization. Only the magnitude data for co and cross polarization remain. Figure 29 shows the number of respective bands designated for ALOS imagery.
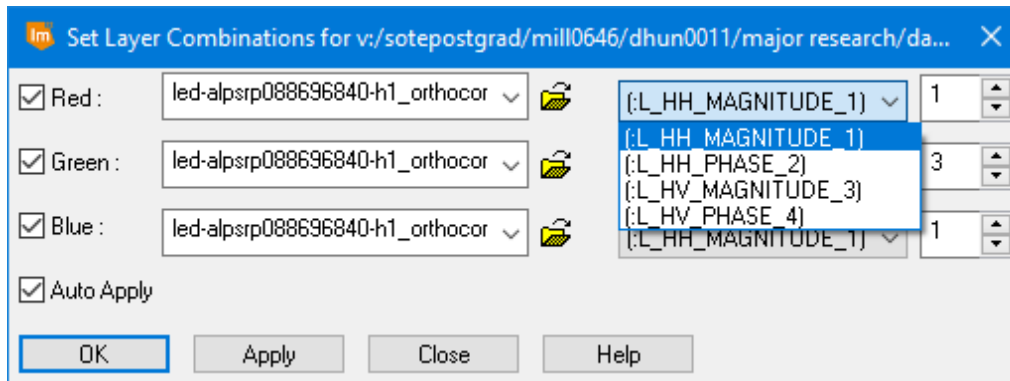
Figure 29: Band composition of ALOS before spectral subset.

After the spectral sub-setting, 2 bands were discarded (1. phase data for co-polarization and 2. Phase data for cross-polarization). Figure 30 shows the band composition for ALOS after spectral subset.
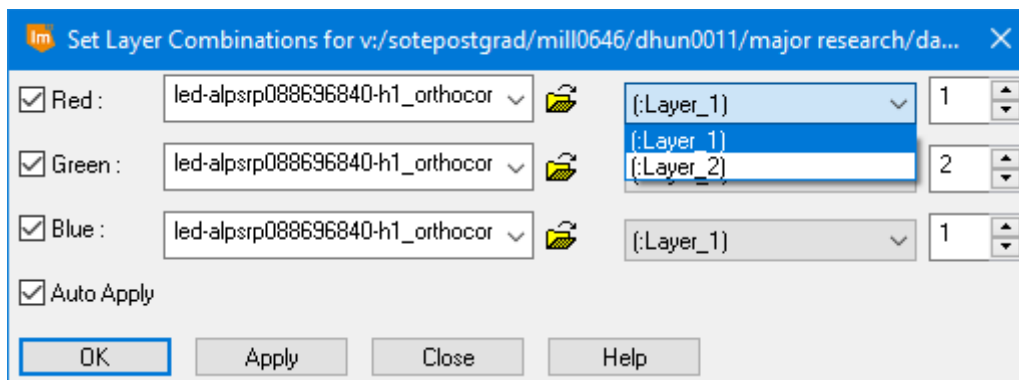
Figure 30: Band composition of ALOS after spectral subset.

4.3.4 Geometric Correction

Geometric correction was performed to ALOS imagery despite conducting ortho-rectification previously. Polynomial model was used with 28 GCPs for correction. Sentinel 2a imagery was used as

the reference imagery. The error obtained in X and Y directions are 13.3 metres and 12.1 metres respectively. The GCPs used in geometric correction of ALOS are presented in Table 9.

Table 9: GCPs used for geometric correction of ALOS image

| Point ID	X Input	Y Input	X Reference	Y Reference	X Residual	Y Residual	RMS Error
GCP #1	311040.069	8109416.129	311030.068	8109417.35	-9.207	5.364	10.656
GCP #2	301996.321	8115704.796	302015.238	8115689.001	16.03	-6.717	17.381
GCP #3	272187.277	8119622.591	272200.432	8119614.994	1.078	3.898	4.044
GCP #4	271257.74	8133108.848	271267.7	8133080.906	-4.772	-5.34	7.162
GCP #5	299036.607	8102212.252	299047.844	8102222.522	9.895	8.133	12.808
GCP #6	299499.111	8152067.661	299512.668	8152020.804	3.509	-7.814	8.565
GCP #7	325764.147	8151445.11	325746.607	8151429.685	-20.01	23.858	31.138
GCP #8	324031.257	8117082.346	324045.532	8117072.217	17.418	0.704	17.432
GCP #9	330313.207	8134372.796	330301.063	8134366.264	-10.289	18.771	21.406
GCP #10	324066.979	8141233.616	324068.049	8141185.528	-0.061	-17.321	17.321
GCP #11	279339.663	8112131.213	279322.598	8112125.39	-25.783	-0.321	25.785
GCP #12	276088.941	8108717.139	276086.232	8108725.642	-11.746	11.105	16.164
GCP #13	306795.716	8133494.968	306802.554	8133477.424	2.158	6.372	6.727
GCP #14	290356.709	8119121.999	290375.603	8119133.363	12.08	22.966	25.949
GCP #15	317055.001	8111465.056	317079.152	8111442.055	26.308	-17.016	31.331
GCP #16	287016.062	8122693.097	287035.302	8122679.212	10.845	0.556	10.859
GCP #17	295297.901	8132615.77	295321.058	8132580.285	15.365	-12.63	19.89
GCP #18	300609.386	8144895.65	300615.357	8144880.592	-2.496	18.113	18.284
GCP #19	303396.314	8145732.68	303406.534	8145708.573	2.401	9.825	10.115
GCP #20	279924.246	8147410.075	279919.874	8147358.69	-19.173	-16.74	25.452
GCP #21	265144.323	8143412.599	265182.895	8143373.132	20.28	-8.526	22
GCP #22	279609.206	8095510.17	279604.385	8095516.513	-10.512	-1.876	10.678
GCP #23	333914.704	8110892.415	333901.633	8110867.521	-6.02	-18.917	19.851
GCP #24	328199.709	8113796.674	328194.151	8113785.365	-0.651	-3.079	3.147
GCP #25	318877.634	8107598.312	318851.05	8107589.478	-23.238	-5.985	23.996
GCP #26	317742.728	8156720.577	317749.201	8156665.177	0.794	-12.012	12.038
GCP #27	331062.737	8118768.923	331063.693	8118761.128	5.798	4.628	7.418
					X	Y	Total

		Control Point		
	Error	13.3291	12.1068	18.0067

The ALOS images before and after geometric correction were overlapped with Sentinel 2a to visualize the effect of geometric correction. A sample area was chosen to see the before and after changes in the imagery that is represented in Figure 31. Swipe tool was used for visually confirming the change.
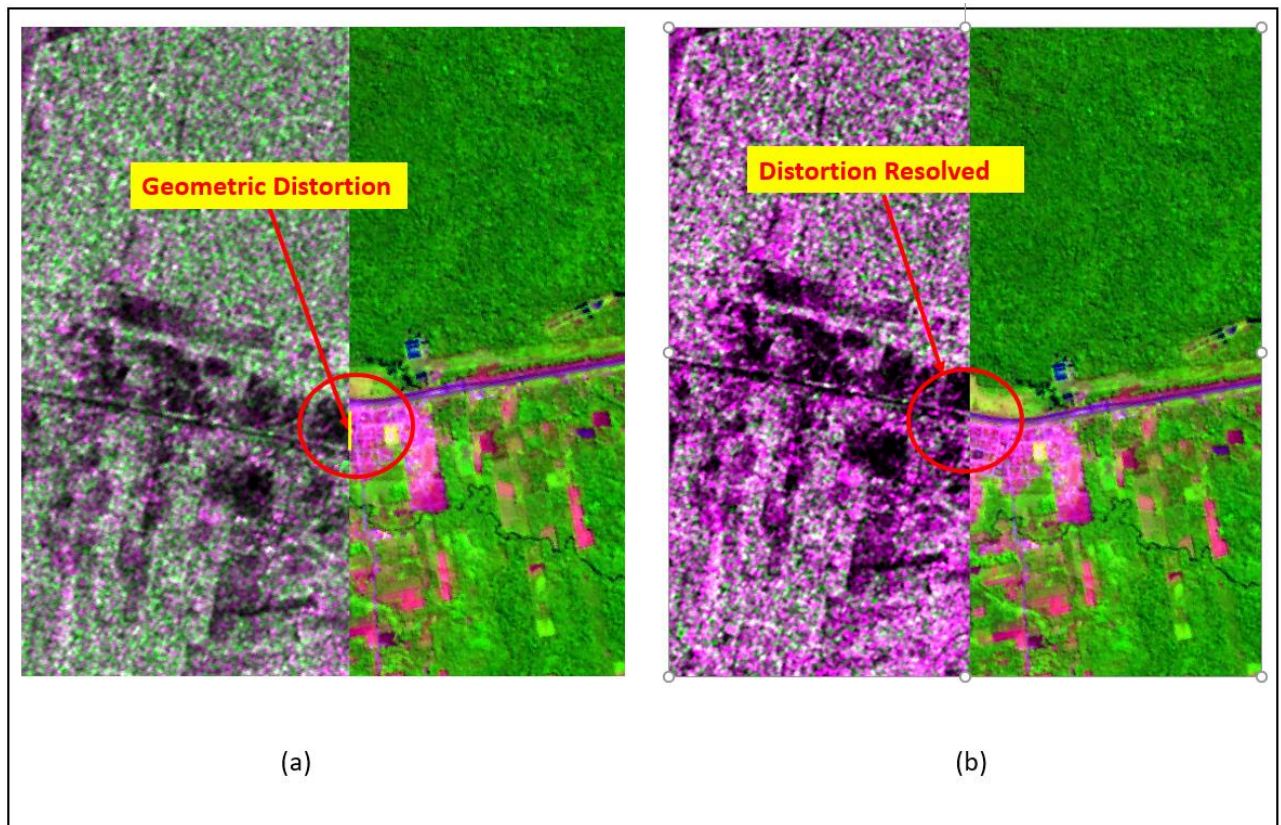
Figure 31: (a) ALOS image before geometric correction and (b) ALOS image after geometric correction

4.4 Digital Image Processing of Landsat 5 TM

4.4.1 Supervised Image Classification

Supervised Image Classification using MLC classifier was performed on the Landsat images. Two different supervised classifications were done - 1. By taking all the classes in account 2. By focusing only on Old Forest features. The list of classes that were used in this classifications are presented in Table 6 and 7.

The classified image had unclassified pixels as well as misclassified pixels all over the image. To reduce this problem, smoothing of classified image was done initially using majority filter followed by clump and sieve operations which has already been discussed in section 3.5. The final result of image classification after applying all the necessary smoothing operations is represented by Figures 33 and 34. Figure 33 represents the classified image using all 7 signature classes and Figure 34 represents the classified image obtained using 2 classes: Old Forest and Others.
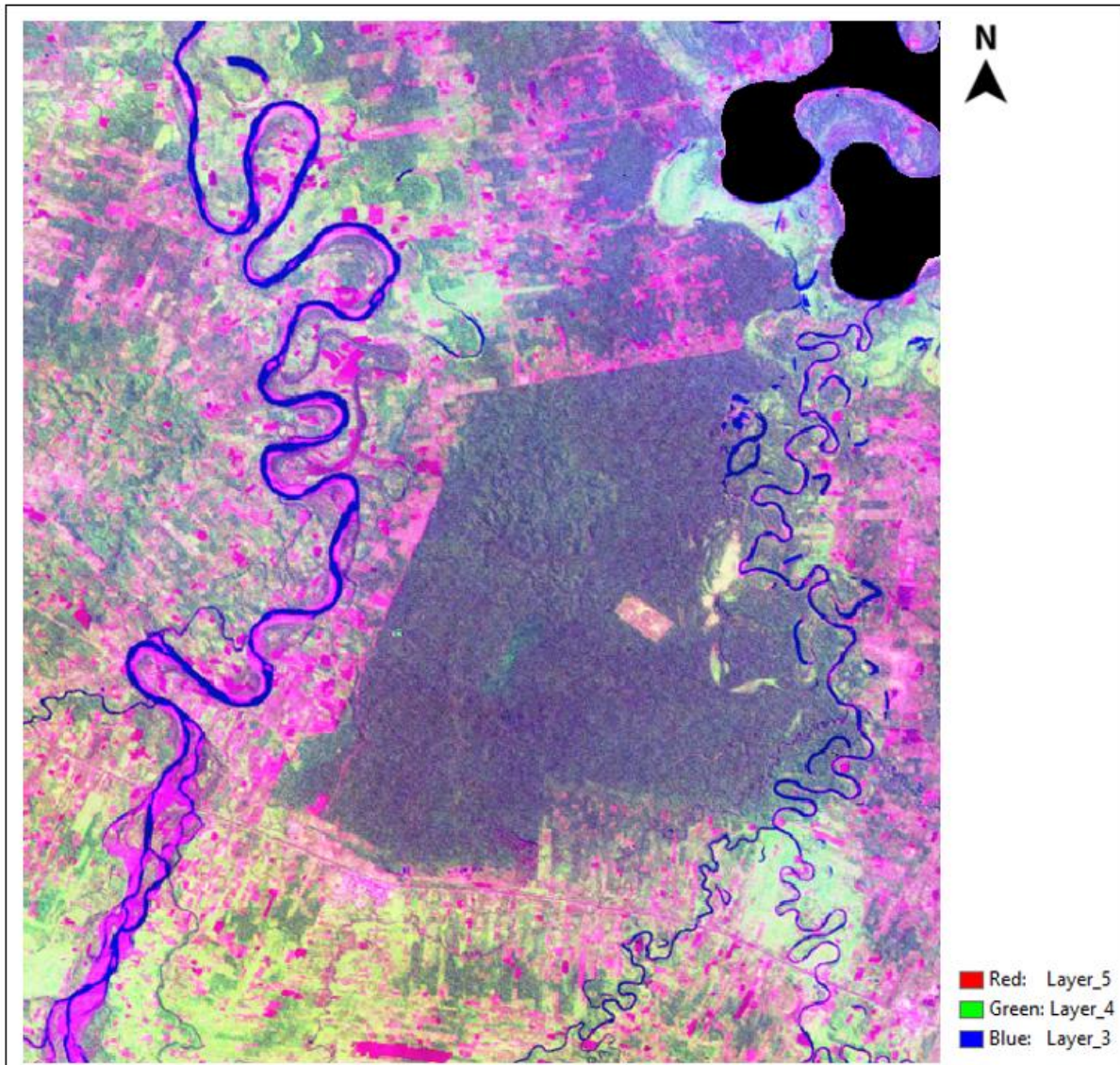
Figure 32: Original Landsat 5 TM Imagery

Supervised Classification of Landsat 5 TM

Legend:
- Unclassified (black)
- Regrowth (green)
- Banana (yellow)
- Bare Land (tan)
- Bare Land and Grass (pink)
- Pasture (gray)
- Old Forest (dark green)
- Water (blue)

0 0.5 1   2   3   4 Kilometers

Author: Abhishek Dhungel
Date : 8th October, 2018
Data Source : United States Geological Survey Earth Explorer

Reference System: WGS 1984 UTM Zone 20S

N
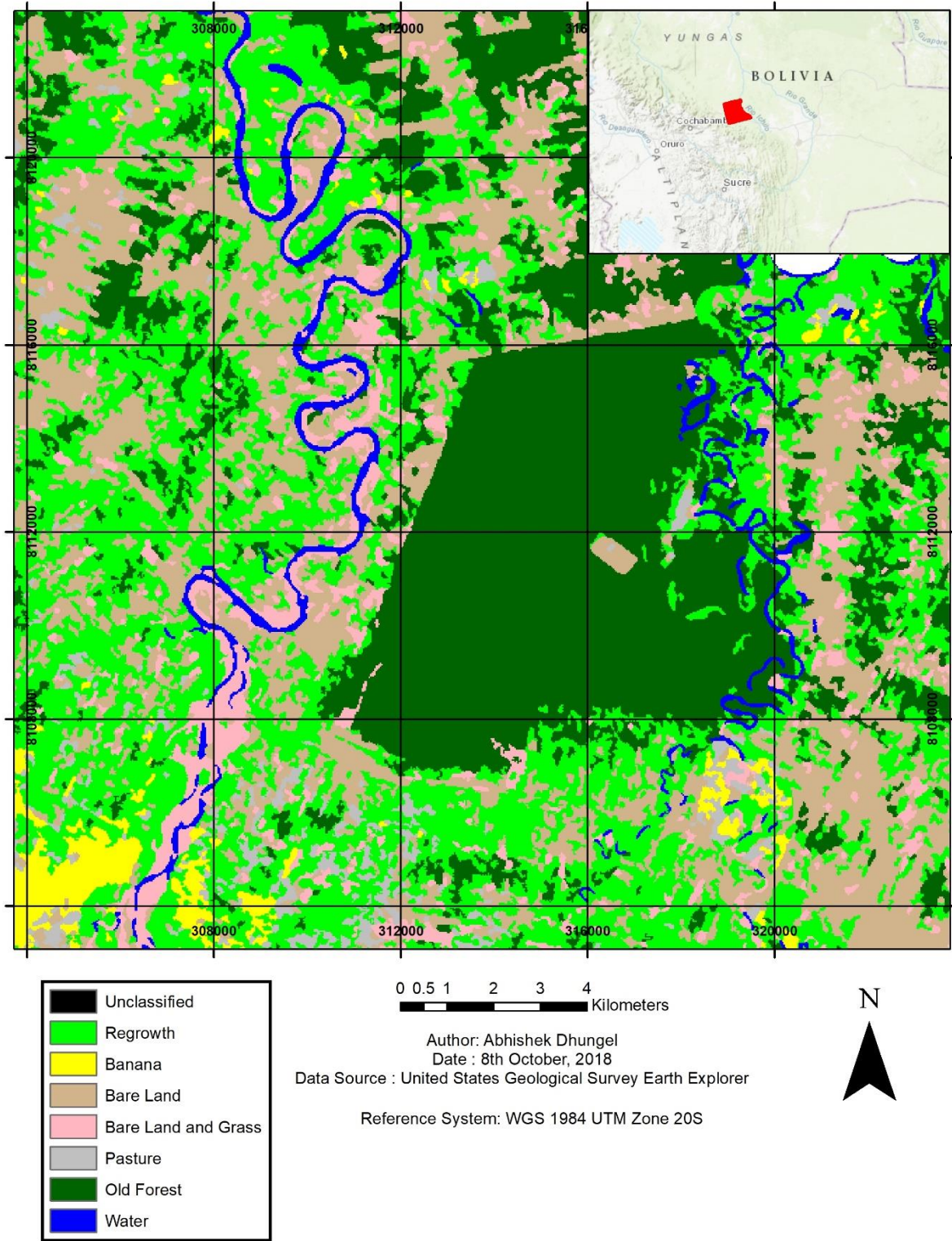
Figure 33: Supervised Classification using all 7 classes
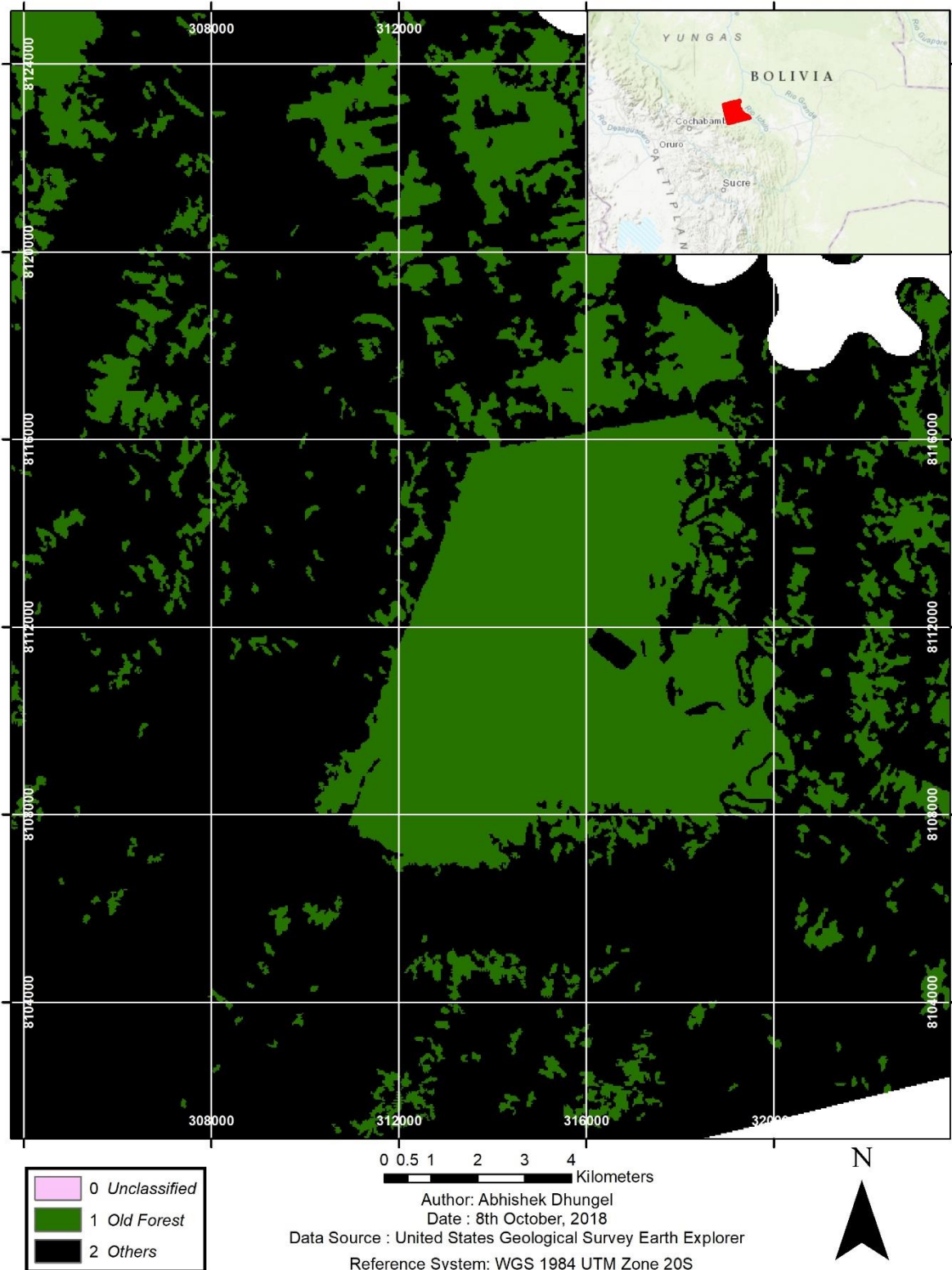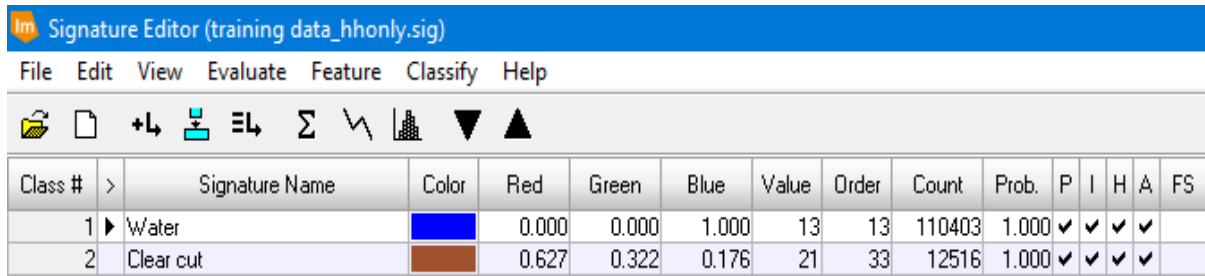
Figure 34: Supervised Classification using only 2 classes- Forest and Others

4.5 Digital Image Processing of ALOS-1 PALSAR

4.5.1 Supervised Image Classification

Supervised Image Classification was performed on ALOS imagery. Two classifications were performed utilising signatures form 2 signature editors.

The signatures used for both classifications are shown in Figure 35 and 36 respectively.
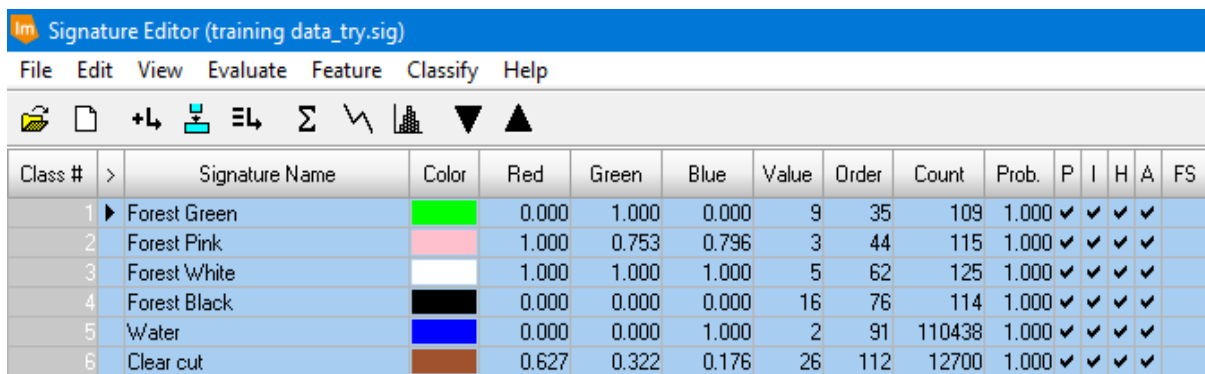
Figure 35: Signatures for Water and Clear-cut

Figure 36: Signatures for Forest, Water and Clear-cut

The supervised classified outputs using signature classes from Figure 37 and Figure 38 are below.
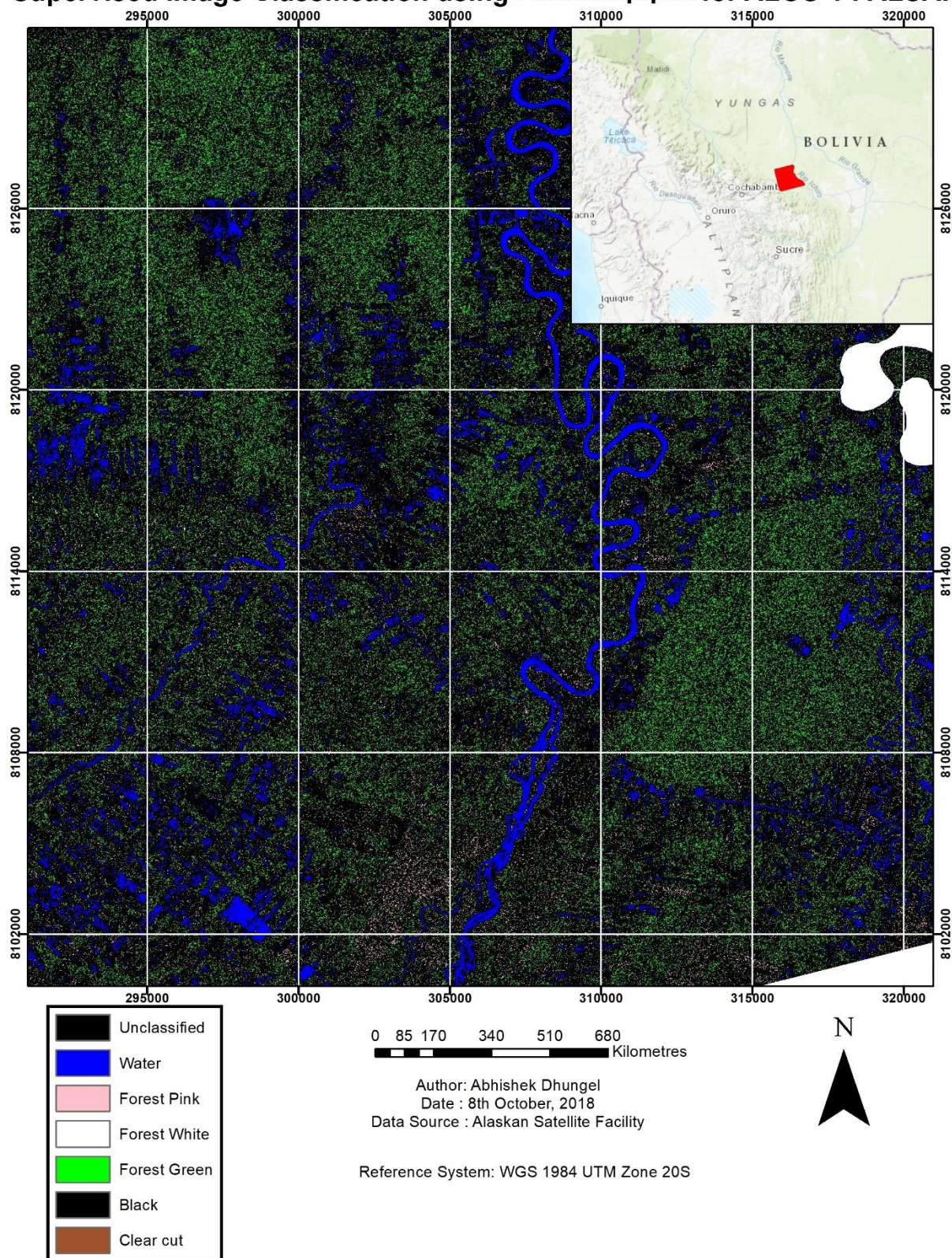
Figure 37: Pixel based classification of ALOS image using only clear-cut and river class
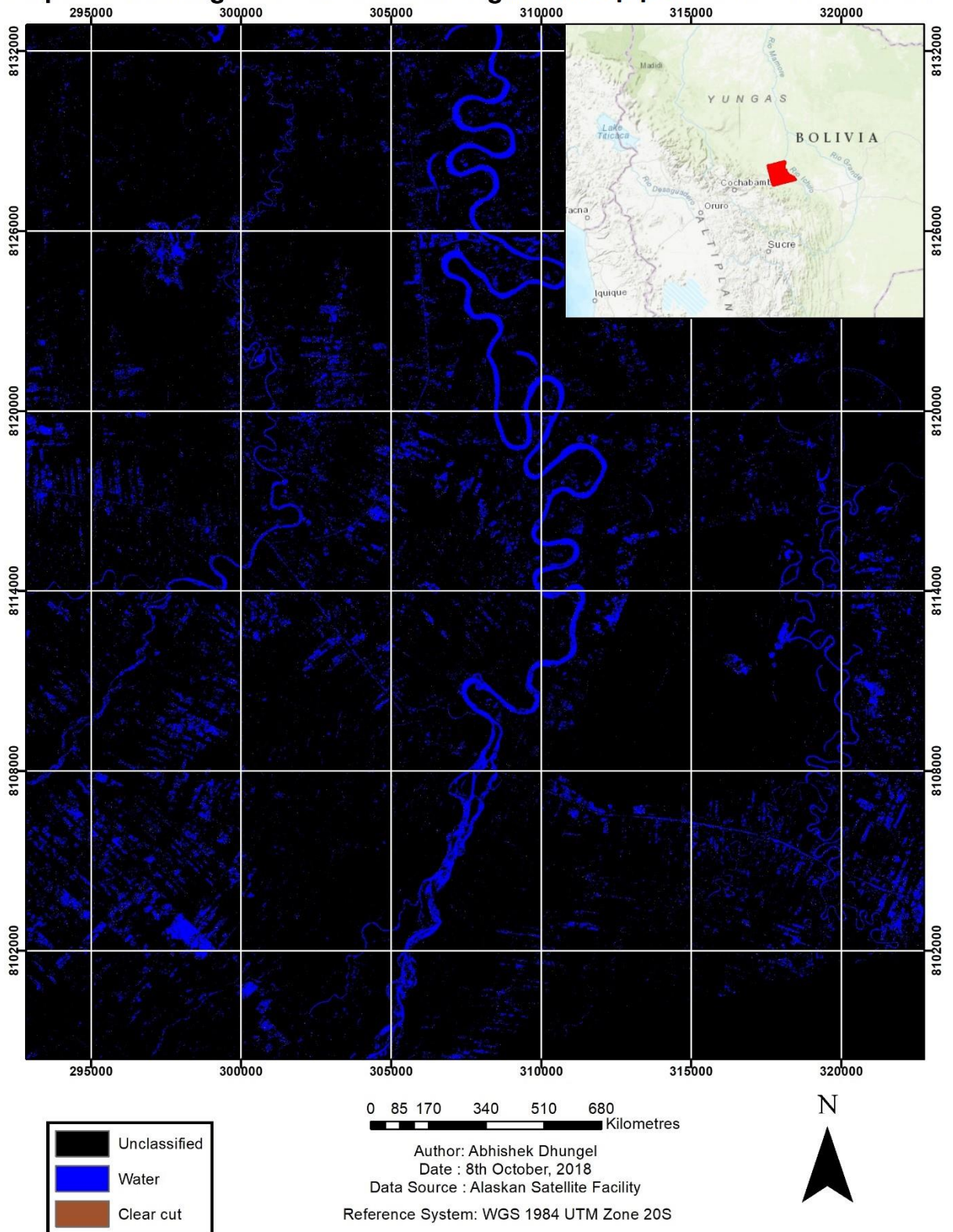
Figure 38: Pixel based classification of ALOS image using all possible signatures

4.5.2 Separability Calculation using Jefferies-Matusita (JM) Distance

JM distance was used to calculate the separability between the various samples. The distance value between each samples are shown in Figure 39 and Figure 40.
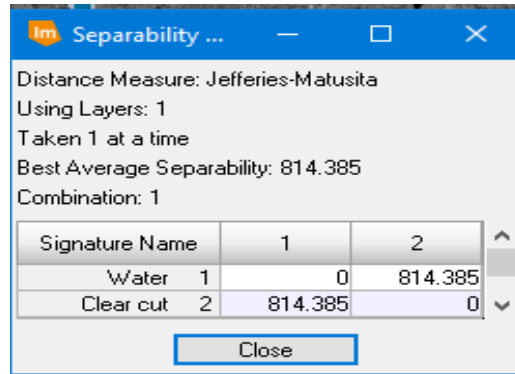
Figure 39: Value of separability between water and clear-cut using JM distance
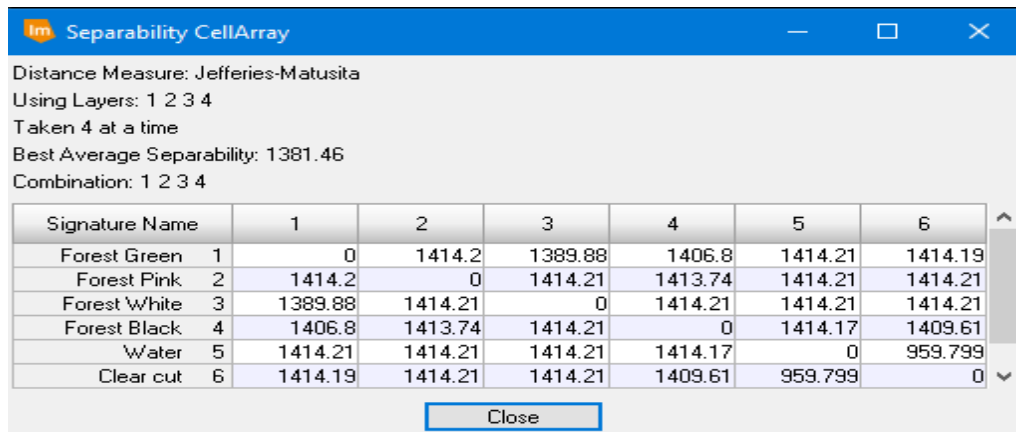
Figure 40: Value of separability between Forest (Green, Pink, White and Black), water and clear-cut using JM distance

4.5.3   Object Oriented Classification (OOC) via Machine Learning

The background to OOC has already been discussed in the section 3.9.3. Initially, FLS segmentation was applied to the imagery separating the images into number of fragmented polygons. Trial and error methods led to 26 different samples from which best looking segmentation was used. The selected segmentation showed potential in differentiating the features based on the creation of several objects

representing each features of the imagery. Some examples for FLS segmentation with varying of the parameters are shown in Figure 42.

A test area was selected where all the trial and error was performed (Figure 41). Creating a test area to save time as well as computational memory.
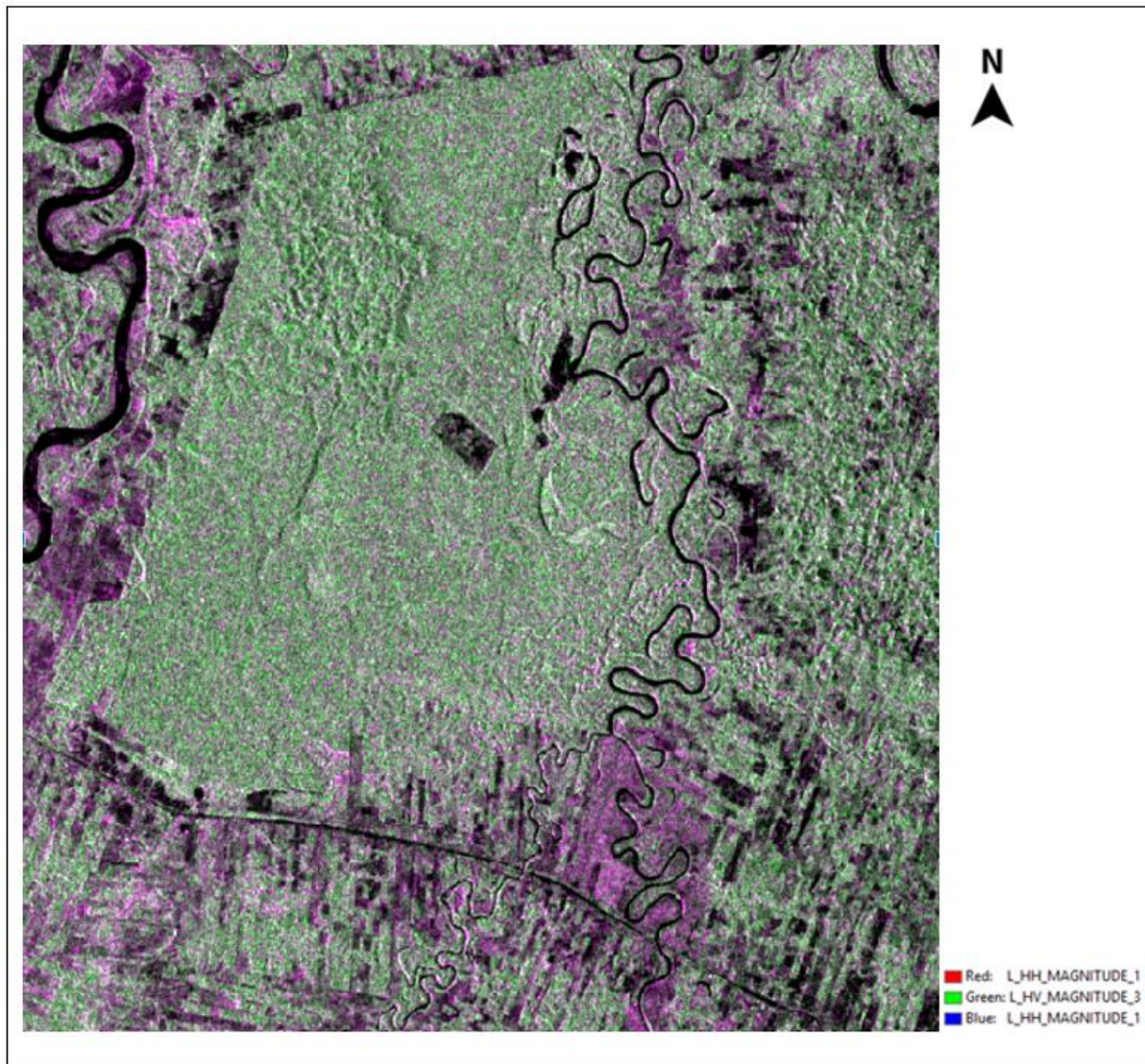
Figure 41: Test area for FLS Segmentation
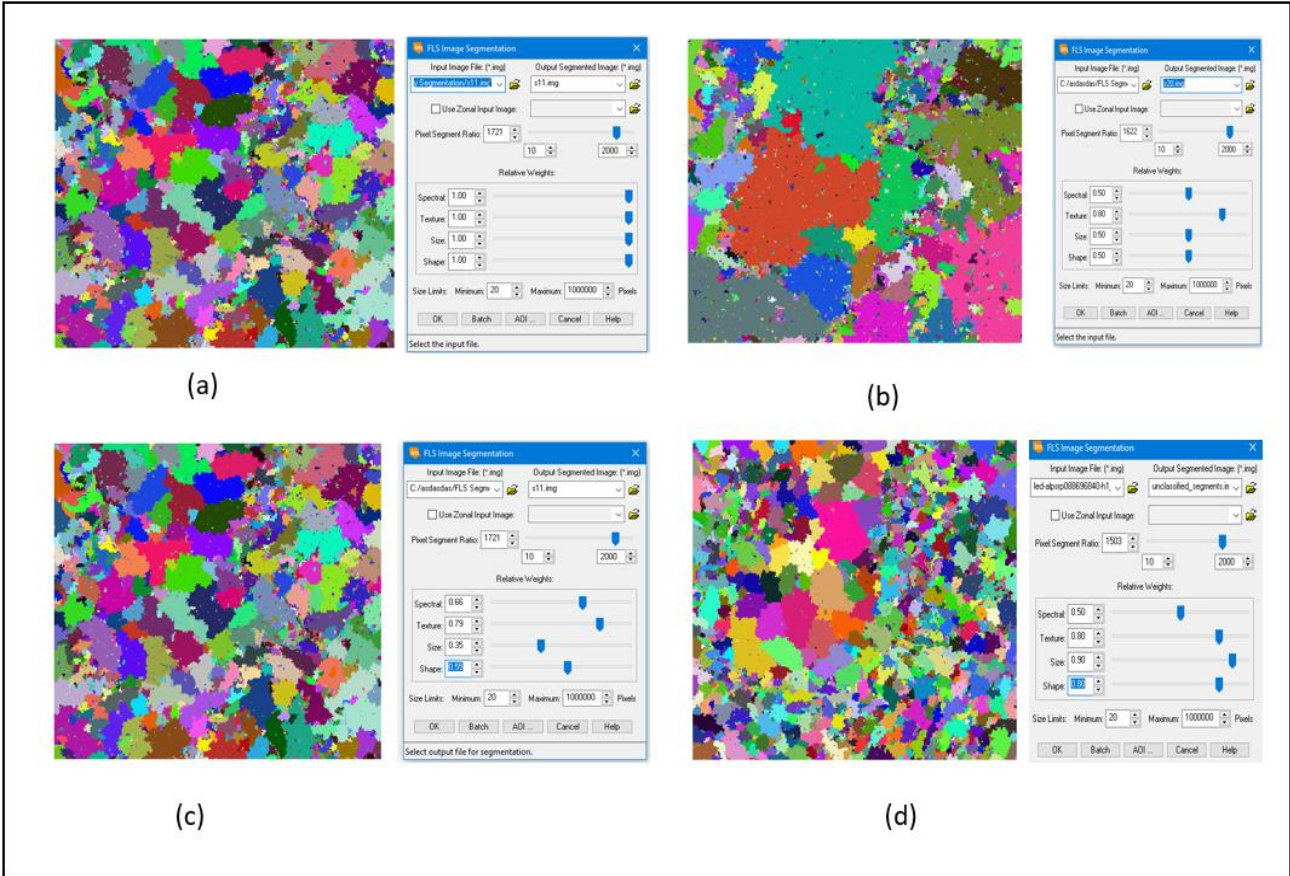
Figure 42: Four test samples of image segmentation

Out of above 4 segmentation samples, the most accurate looking segmentation was (d). The value for all the parameters of FLS Image Segmentation are:

- Pixel to Segment Ratio : 1503
- Relative Weight for Spectral : 0.5
- Relative Weight for Texture : 0.8
- Relative Weight for Size = 0.9
- Relative Weight for Shape = 0.8
- Minimum Pixel Size : 20
- Maximum Pixel Size: 1000000

Using this segmentation, machine learning was performed. Once machine learning was completed and classification was achieved, smoothing operations were applied which gave the final classification raster. After performing both classification as similar to section 3.4.1, the classification maps were generated. Figure 43 and Figure 44 represents the final classification maps for both the approaches.

Object Oriented Classification via Machine Learning for ALOS-1 PALSAR
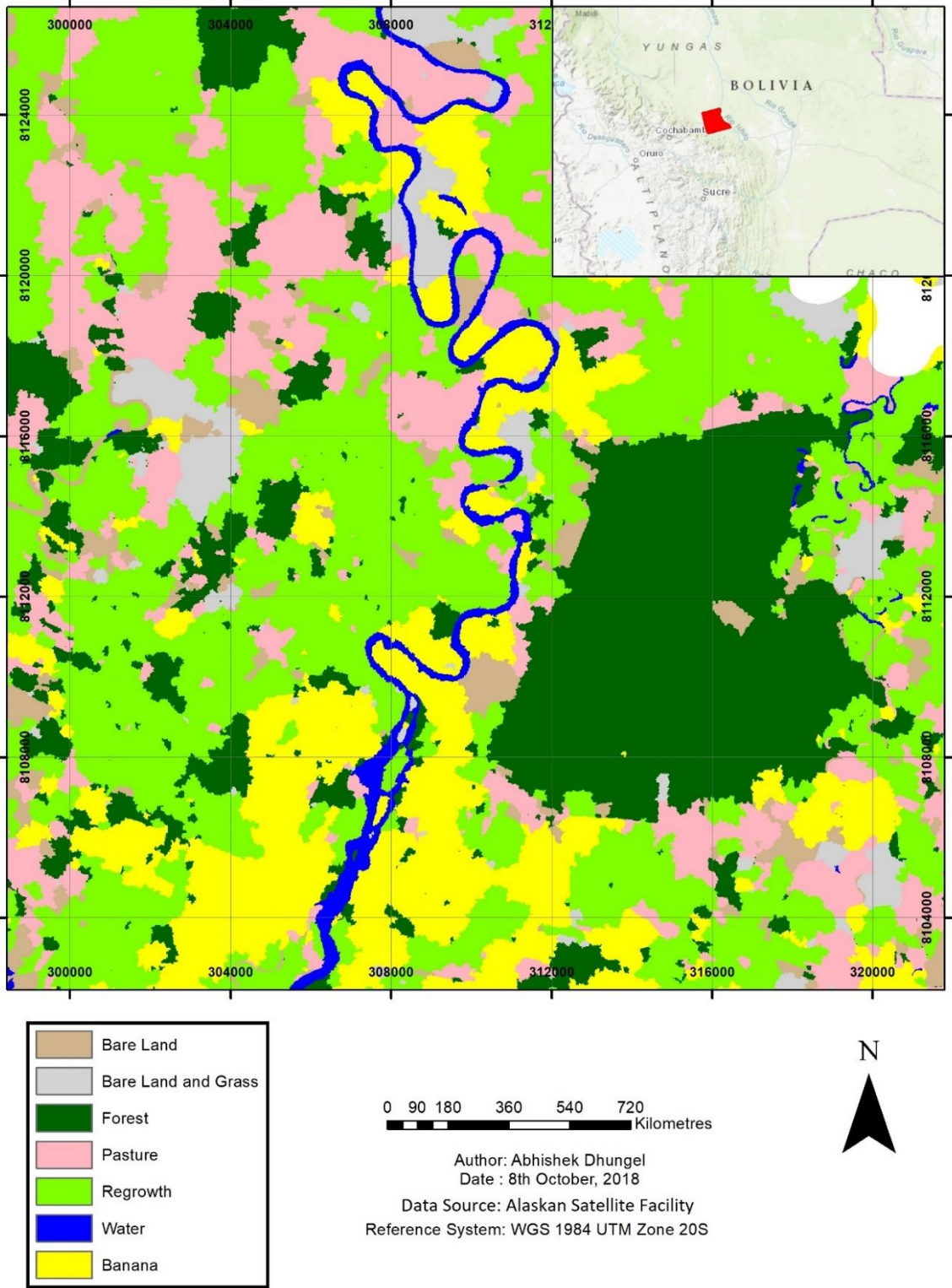
Figure 43: Image classification of ALOS imagery

Object Oriented Classification via Machine Learning for ALOS-1 PALSAR
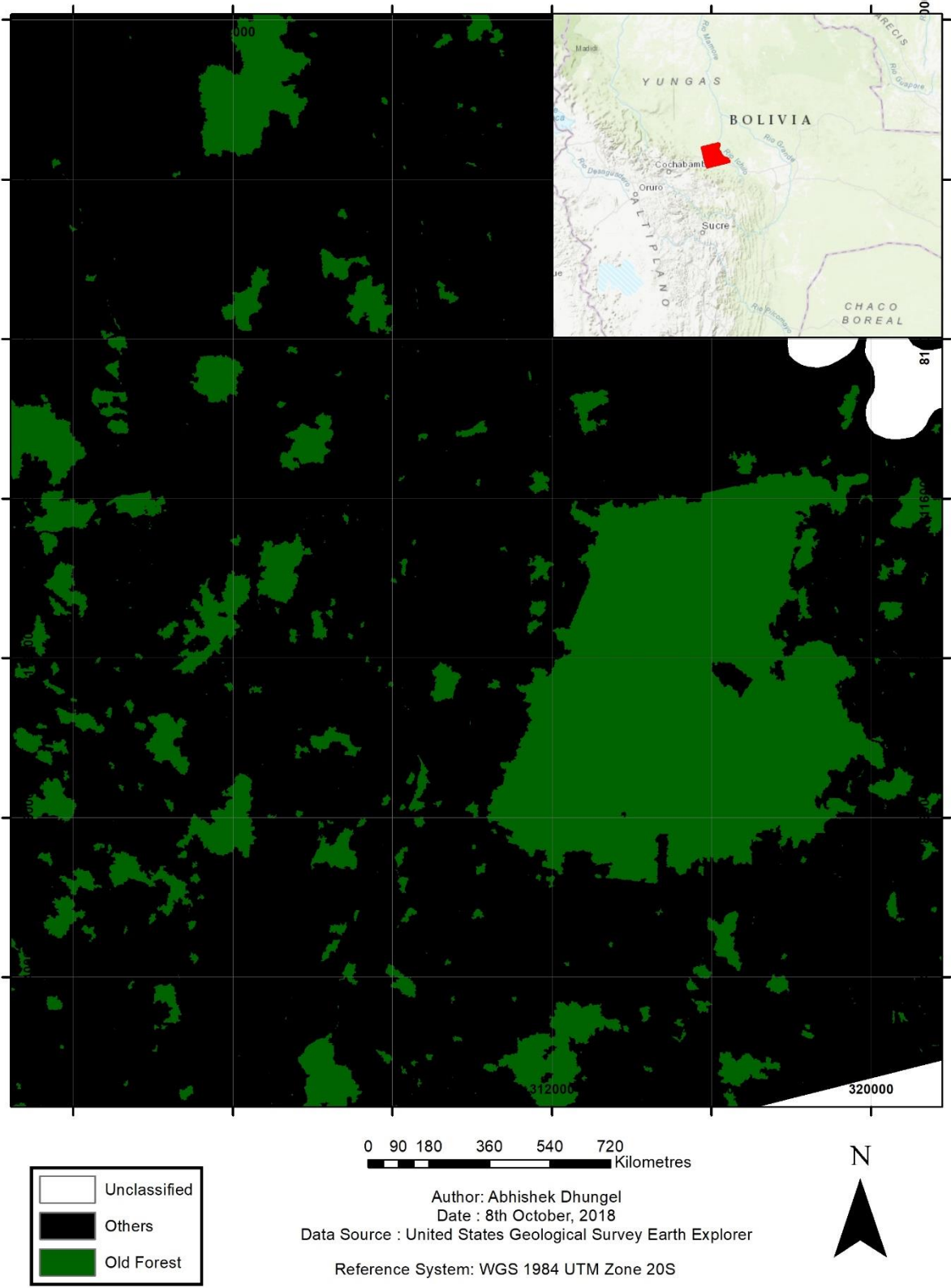
Figure 44: Image classification of ALOS imagery

4.6 Accuracy Assessment

After the classification of both Landsat and ALOS, accuracy assessment was performed. The same set of ground truth were taken as a measure of determining the accuracy in both the images.

Accuracy was initially calculated for both the classifications of Landsat TM 5 imagery and ALOS imagery. Tables 11, 13, 15 and table 17 gives insight to the omission and commission errors for the classified image and tables 10, 12, 14 and 16 present measures of misclassification.

Table 10: Error Matrix for Landsat when all the classes were taken into consideration

Classified Data	Regrowth	Banana	Bare Land	Bare Land and grass	Pasture	Old Forest	Water
Regrowth	131	2	4	0	6	1	0
Banana	8	41	0	0	0	0	0
Bare Land	59	8	150	1	5	1	1
Bare Land and G	6	0	1	43	2	0	1
Pasture	18	12	1	1	87	0	0
Old Forest	4	0	1	0	0	50	0
Water	0	0	0	0	0	0	17

Table 11: Accuracy Totals for Landsat when all the classes were taken into consideration

Class Name	Reference Totals	Classified Totals	Number Correct	Producers Accuracy	Users Accuracy	Kappa Value
Regrowth	226	144	131	57.96%	90.97%	0.8629
Banana	63	49	41	65.08%	83.67%	0.8196
Bare Land	157	225	150	95.54%	66.67%	0.563
Bare Land and G	45	53	43	95.56%	81.13%	0.7976
Pasture	100	119	87	87.00%	73.11%	0.6832
Old Forest	52	55	50	96.15%	90.91%	0.9013
Water	19	17	17	89.47%	100.00%	1

Overall Classification Accuracy =   78.40%   Overall Kappa Statistics = 0.7294

70

Accuracy assessment was done for the Landsat image classification raster in which the classification of Old Forest and Others features was done.

Table 12: Error Matrix for Landsat was presented which used 2 classes- Old Forest and Others

Classified Data	Background	Old Forest 1	Others 2	Row Total
Old Forest	0	49	5	54
Others	0	3	605	608
Column Total	0	52	610	662

Table 13: Accuracy Totals Landsat was presented which used 2 classes- Old Forest and Others

Class Name	Reference Totals	Classified Totals	Number Correct	Producers Accuracy	Users Accuracy	Kappa Value
Old Forest	52	54	49	94.23%	90.74%	0.8995
Others	610	608	605	99.18%	99.51%	0.9372
Totals	662	662	654			
Overall Classification Accuracy = 98.79%			Overall Kappa Statistics = 0.9180			

The accuracy assessment of ALOS-1 PALSAR was applied in the same way that followed Landsat with all 7 class objects.

Table 14: Error matrix for the classification of ALOS with all the classes included

Classified Data	Background	Regrowth	Banana	Bare Land	Bare Land and Grass	Pasture	Old Forest	Water
Regrowth	0	41	1	10	4	16	1	2
Banana	0	0	26	4	2	2	0	0
Bare Land	0	6	1	62	0	2	19	0
Bare Land and Grass	0	20	0	17	78	7	0	0

Pasture	0	53	8	10	0	144	6	0
Old Forest	0	0	0	0	0	0	17	0
Water	0	0	9	9	1	2	0	82
Column Total	0	120	45	112	85	173	43	84

Table 15: Accuracy Totals for the classification of ALOS with all the classes included

Class Name	Reference Totals	Classified Totals	Number Correct	Producers Accuracy	Kappa
Regrowth	120	75	41	34.17%	0.4463
Banana	45	34	26	57.78%	0.7475
Bare Land	112	90	62	55.36%	0.6255
Bare Land and Grass	85	122	78	91.76%	0.5862
Pasture					0.5283
Old Forest	43	17	17	39.53%	1
Water	84	103	82	97.62%	0.7665
Totals	662	662	450		
Overall Classification Accuracy =	67.98%	Overall Kappa Statistics = 0.6098			

Accuracy assessment of ALOS imagery was performed using just 2 class object i.e. Old Forest and other features.

Table 16: Error matrix for the classification of ALOS with only 2 class

Classified Data	Old Forest	Others	Row Total
Old Forest	66	24	90
Others	4	568	572
Column Total	70	592	662

Table 17: Accuracy Totals for the classification of ALOS with only 2 class

Class Name	Reference Totals	Classified Totals	Number Correct	Producers Accuracy	Users Accuracy	Kappa
Old Forest	70	90	66	94.29%	73.33%	0.7018
Others	592	572	568	95.95%	99.30%	0.9339
Totals	662	662	634			

Overall Classification Accuracy = 95.77 %   Overall Kappa Statistics = 0.8041

CHAPTER FIVE

DISCUSSION

This chapter presents a discussion of results and examines some key issues relating to the methods and results.

5.1. Image Pre-processing for Landsat 5 TM

5.1.1 Haze Reduction

Haze and cloud have always been a major problem in optical remote sensing (Kaufman and Sendra 1988). The image acquired from USGS EE-portal was already geometrically and atmospherically corrected. The image was free of illumination issues as well. Haze having low optical thickness (Crist and Cicone 1984; Kauth and Thomas 1976) is not considered when the image is atmospherically corrected. Due to this characteristic, a 'haze reduction model' was used based on the fourth component of TCT (Kauth and Thomas 1976).

Even after running the haze reduction model, the image still had significant effects of haze in it. The Landsat scene was acquired during mid-day when the illumination of the sun was at its maximum. This event might have escalated haze production in the atmosphere because of strong positive correlation between sun and haze (Kong et al., 2011). As the area of study is located in a tropical region, it might have relatively high humidity during image acquisition which may have triggered the formation of haze in the scene (Zhang et al., 2002). When TCT was performed, it sets a threshold value for haze reduction based on the numerical value of the fourth component of TCT. Any pixel value under the threshold is considered to be hazy in nature and is removed by the algorithm. In our case, thickness and density of the haze present in the atmosphere caused some pixel values to exceed the threshold set by the haze reduction algorithm. This caused some pixels even with atmospheric haze to be omitted by the algorithm and haze could still be seen in the image even after performing the haze reduction process. The haze reduction algorithm reduced approximately 5% of haze out of total 7%.

5.2 Image Pre-Processing for ALOS-1 PALSAR

5.2.1 Image Ortho-rectification

The acquired PALSAR was in slant range geometry. The range and azimuth resolution were compressed causing the geometry of the image to be distorted. Ortho rectification was done in order to convert the slant range geometry to ground range geometry. This is considered to be one of the most important process for SAR images pre-processing (Toutin 2004).

The ortho-rectified image was still geometrically distorted to some extent. This was caused due to the misalignment of pointing vectors of the ALOS-1 PALSAR itself (Shimada et al., 2009). This is a prominent error in most products produced by ALOS. This error was further diminished later using geometric correction.

5.2.2 Speckle Removal

The fluctuations in the phase of returning electromagnetic signals causes speckle in the resulting image (Bamler 2000). The presence of such speckles is always related to reduction in the appearance as well as the quality of SAR data (Ali et al. 2008). Adaptive filters have been developed to reduce and correct such speckles while not significantly compromising the radiometric and textural information of the SAR image (Bamler 2000). Gamma- map filter was chosen for speckle suppression based on the procedure follow by Sumantyo and Amini 2008 for quantitative and qualitative operation of ALOS PALSAR image. Speckle suppression was successfully conducted with significant reduction in speckle and noticeable increase in the SAR image quality.

5.2.3 Geometric Correction

SAR geocoded ellipsoid corrected (GEC) imagery is the resulting image from the ortho rectification process (Zhang et al., 2013). The problem of geometric distortion was due to rough geocoded reference which tend to decrease the usefulness of the SAR GEC image. Zhang et al (2013) suggested a geometric correction for preserving the usefulness of the corresponding geometric model. The polynomial model was used to correct this geometric distortion error. A total of 28 ground points was used to correct the error. The SAR imagery was corrected using 1st order polynomial. The resulted

75

image was geometrically corrected to a level of accuracy to make it comparable with the 30m spatial resolution Landsat image.

5.3. Digital Image Processing of Landsat 5 TM

5.3.1 Supervised Image Classification

Richards (1993) regards supervised image classification as a crucial approach in extracting feature information from remotely sensed data. Maximum likelihood Classification was used which assumes that multivariate normal distribution can define spectral class in the image. MLC is considered to be the most accurate classifier but is time consuming compared to parallelepiped (Richards, 2013). The classification turned out to be good when examined visually but statistical analysis was done under accuracy assessment. The problem with supervised classification was inaccuracy of training samples. There were numerous pixels that were misclassified under different classes. The confusion between Old Forest and Regrowth became a bigger issue during signature extraction which indeed lead to clash in classification between Old Forest and Regrowth (Figure 45). The difference in Pasture and Vegetation (Banana) in a 30metre resolution imagery was a greater challenge with both features reflecting almost same spectral reflectance (Figure 46). The classified image was then treated for anomalies.
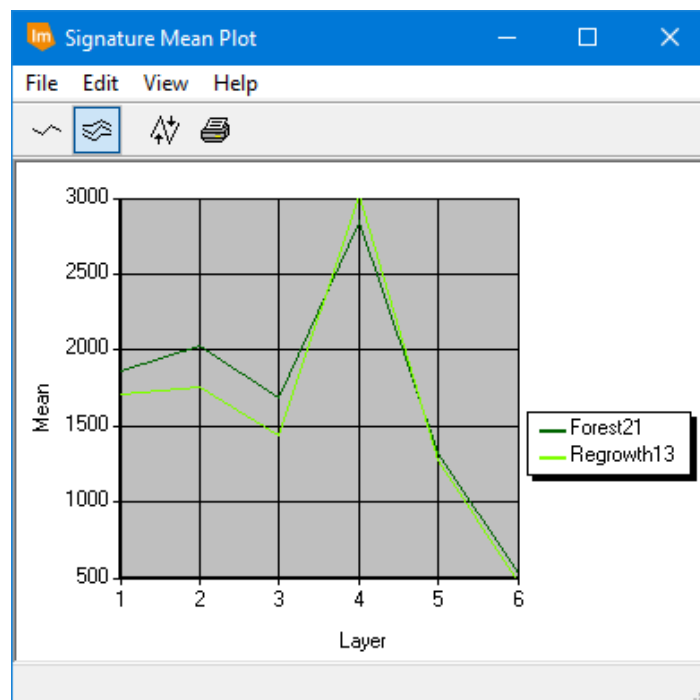
Figure 45: The mean spectral signatures of Old Forest and Regrowth
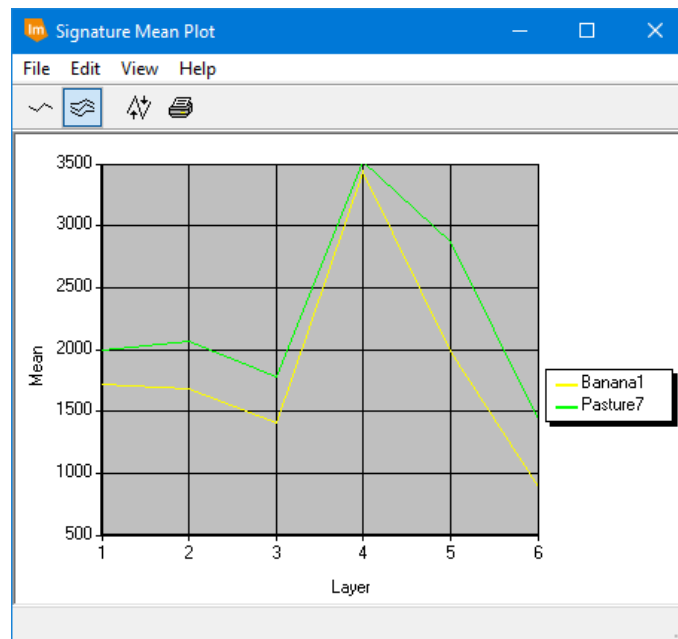
Figure 46: The mean spectral signatures of Banana and Pasture

5.4 Image post processing

5.4.1 Recode

The recode tool helps in combining signatures and producing a new image with distinct feature classes. It combines classes through recoding more than one existing class to the same new class value. After the classification, the obtained image had numerous signatures which had not been merged into the separate classes. Recoding was done by assigning the class number and combining those signature belonging bearing the same class number.

5.4.2 Majority Filter

Majority filter was the ideal choice for removing the misclassified pixels and smoothing the classification. In this research, neighborhood functions were used with function definition selected as Majority. All neighborhood definition 3 * 3, 5 * 5 and 7 * 7 were used to see the change in the classified image made by each neighborhood. At last, the output from using 3 * 3 was accepted since the use of 5 * 5 and 7 * 7 neighborhood window resulted in an overly smooth classification.

5.4.3 Clump and Sieve

The clump function identifies contagious group of pixels based on the majority filter output. The sieve function takes the clump function as an input and removes the contagious group of pixel based on the user defined threshold. Initially, clump function was used to the output raster of majority filter which selected the contagious group of pixels and these pixels were later removed using Sieve function. The combination of clump and sieve operations removed the contagious group of pixels and resulted in a finer and smoother classified raster.

5.5 Supervised Image Classification for ALOS -1 PALSAR

The same approach was used to that of Landsat for the initial part of the classification. The image appeared quite unusual compared with the 6-band sensor. Initially, visual analysis was done on the RADAR image and some strange things were noticed. The water feature and the clear-cut, both appeared black in the imagery whereas the forest feature was represented by not 1 but 4 different objects. After the two-classification based on the number of classes were done (Figure 35 and Figure 36), the results were not convincing as the classification between water and clear-cut resulted in a classification where both the objects were classified by a single color (blue) (Figure 37 and Figure 38). The major reason behind this problem must be the texture of water and clear-cut. Both these objects are smooth, so the classifier was unable to differentiate these objects as the classification in RADAR is based on the value of backscatter and certainly not on the "spectral" level. With different classifications leading towards same result, a conclusion was drawn stating that pixel-based classification was inappropriate for the classification of RADAR imagery.

5.6 Separability Calculation using Jeffries Matsusita (JM) distance

This method is based on the value of statistical distance between training samples (Richards, 2013). An indication of how similar or different the spectral signatures are from one another is made using this technique (Congalton, 1991a). It supports the choice to discard signatures that are not important in classification. Kavzonglu and Mather (2000) concluded JM distance yielded best result as a feature classification technique. In this research, Jefferies-Matusita distance was used as a measure of separability between various signatures.

The range of JM distance varies from 0 to 1.414 (0 to 1414, in ERDAS Imagine)(Congalton, 1991a). The lower limit value range of 0 to 1250 suggests that the signatures for classes are in fact for the same feature and they can be merged with one another while the upper limit value range from 1250 to 1400 suggest that the classes are very distinct from one another and should be treated as different classes (Kavzonglu and Mather, 2000).

With the value of JM distance being 814.385 (Figure 47) for water and clear-cut, the conclusion was drawn stating the fact that water and clear-cut are spectrally similar in the image and they need to be merged with each other to perform image classification. From Figure 48 the objects (Pink, Green, White and Black) that constitute forest are found to be "spectrally" dis-similar and cannot be merged into a single class. But the grouping of these "spectrally" dis-similar objects formed a pattern which can potentially be classified with classifier which are object oriented. This led to the conclusion that pixel-based classification is not suitable for RADAR image and another approach had to be implemented to fulfil the research criterions.
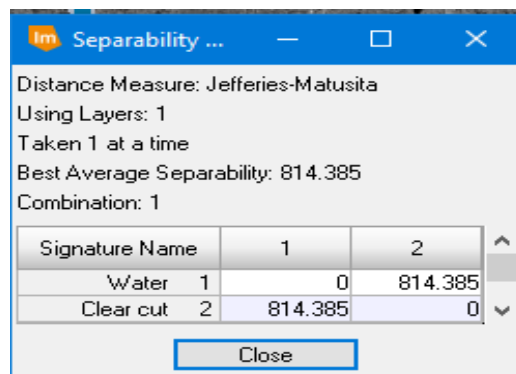
Figure 47: Value of separability between water and clear-cut using JM distance
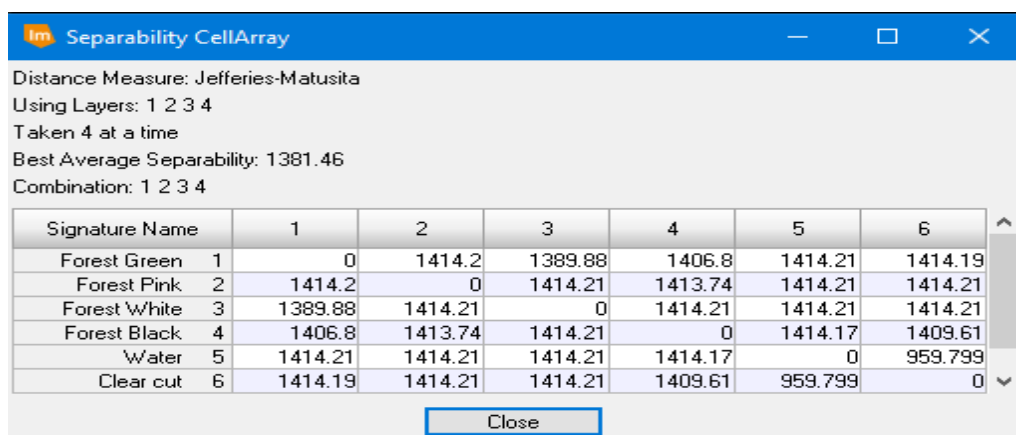
Figure 48: Value of separability between Forest (Green, Pink, White and Black), water and clear-cut using JM distance

79

5.7 Object Oriented Classification via machine learning

OOC is preferred while working with images of higher resolution and are based on image segmentation (Haila, 2002). OOC is useful in extracting useful information from the image and is solely depended upon the segments of the objects rather than pixel (Benz et al., 2004). The overall computation is done in two steps as mentioned in section 3.9.3.

In this study, initially Full Lambda Schedule (FLS) segmentation was done to create segments based on the locations and pixel values. FLS is a bottom up merging algorithm which takes spectral content and radiometric value of segments into consideration while merging decisions. There were 6 sets of parameters that needed to be provided in order to perform image segmentation. The parameters include – pixel to segment ratio, spectral weight, texture weight, size weight, shape weight and the size limits. No fixed set of segmentation parameters have been defined in any literature, therefore hit and trail method was applied to find the suitable set of parameters for this research. 26 different samples were created focusing on the specific area of image by creating an AOI. Out of 26 different set of parameters for FLS segmentation, most accurate looking segmentation was selected for classification. The values for the parameters of FLS segmentation that yielded best result among 26 samples is shown in Figure 42.

5.8 Accuracy Assessment

Accuracy assessment for Landsat and ALOS-1 PALSAR was done using the same set of ground truth. The accuracy report generated for each of the sensors have been compiled and tabulated. Result of accuracy assessment is analyzed using two matrices that were generated while computing the accuracy assessment report. The error matrix summaries the error in the classification for each of the signature class (Congalton and Green, 2008). The matrix of total accuracy is the measure of determining the omission error, commission error and overall accuracy by calculating the number of misclassified pixels (Blaschke and sensing, 2010, Congalton, 1991a).

Omission error is defined as a measure of loss of pixels from a class to other class in classification (Congalton, 1991a, Congalton and Green, 2008). Commission is defined as a measure of gain of pixels from another class to the host class (Jensen and Lulla, 1987). Overall Classification Accuracy is the measure of accuracy of the entire classification process and calculated by dividing the sum of number of pure classified pixels for each class by the sum of total number of pixels for each class (Blaschke and sensing, 2010, Congalton, 1991a).

Table 10 gives an insight to the error matrix generated when all 7 classes were taken for classification for Landsat. The diagonal value of error matrix signifies the total number of correctly classified pixels for each of the class. According to table 10, the amount of highly classified signatures for regrowth out of 221 samples was 131, banana is 41 out of 63, bare land was 150 out of 157, bare land and grass was 43 out of 45, pasture was 87 out of 100, old forest was 50 out of 52 and water was 17 out of 17. There is significant number of pixels lost for regrowth while performing classification. Out of 221 samples, 59 have been classified as bare land, 18 have been classified as pasture, 8 have been classified as banana and 6 have been classified as bare land and grass. The second class with the maximum sample loss is banana where out of 63 samples, 12 were classified as pasture, 2 were classified as bare land and 2 were classified as regrowth. The reason behind this vary loss of pixels must be the error while recording pure spectra which is due to the lack of higher resolution of the imagery. The training sample had many pixels with mixed signatures which resulted in the numerous loss of pixels from various classes during classification. Similarly, the class with the highest classification accuracy is water class with 100% that signifies there was neither gain nor loss while classification of water pixels. Likewise, omission and commission accuracies were calculated according to the gain or loss of samples between various classes.

The overall classification accuracy was achieved to be 78.40% which was accepted as the sensor used for classification was Landsat 5 TM with the spatial resolution of 30 metres. Phiri, Darius et al., (2017) concluded their study stating that pixel based classification resulted in 66% accuracy on Landsat ETM+. Similarly, Frohn et al. (2011) got the similar result where they acquired 78% accuracy from pixel based classification while classification different forest types. Zerrouki and Bouchaffra (2014) compared the accuracy between pixel-based approaches and OBIA approaches on Landsat images for mapping forest clearance which resulted in the OBIA with higher classification accuracy of 92.7% over pixel based approach with the accuracy of 78%. 30 metres of Landsat itself accounts for mixed classification even before image classification occurs. The kappa value for respective classes is an indicator of accuracy and agreement between observed accuracy and expected accuracy. It indicates the quality of classification within that specified class. Usually, the kappa value greater than 0.8 represents good accuracy while the value range between 0.4-0.80 represent medium acceptable accuracy but the kappa value less than 0.4 is considered as a poor classification (Richards, 2013).

From Table 11, it can be commented that Old Forest and Water have the highest quality of classification followed by Regrowth and Banana and Bare Land and Grass class with average classification and finally pasture and bare land with lowest quality of classification. The value of overall classification accuracy is not always the indicator for estimating the quality of classification, this value

should be supported with the quality estimator of kappa value. This is an average level of classification for a Landsat satellite.

For the supervised classification using only two classes- Old forest and others; out of 52 samples, 49 was classified as Forest itself with rest of 3 were assigned to others (Table 12). Similarly, out of 610 samples, 605 have been classified as Others and only 5 samples were classified as Forest. The overall accuracy for this classification turned out to be excellent with the value of 98.79% which was supported by overall kappa statistics value of 0.918 (Table 13). The kappa value near to 1 indicates highest quality on classification. Both the class - Old Forest and Others have a kappa value of 0.8995 and 0.9372 respectively which is the reason behind high accuracy classification.

After the accuracy assessment of Landsat, accuracy assessment of ALOS-1 PALSAR was done following the same procedure. Table 14 reflects the errors of sample distribution between 7 objects for ALOS. The result was quite interesting. In the error matrix, the object representing regrowth had the sample count of 41 out of 120 where 20 samples were classified as bare land and grass and 53 pixels were classified as pasture which is more than the sample count for regrowth itself. And the object with least count for misclassification was water where out of 84 samples, 2 were classified as regrowth and in total, 82 samples were classified as water itself. From table 14, a conclusion was drawn stating the fact that machine learning classification for classifying regrowth was a failure. This statement was validated when the producer's accuracy and the value of kappa was analyzed from table (15). Judging by the values of kappa and overall accuracy, the classification using objects-based classifier failed to prove its dominance over MLC for optical image processing.

Despite the low quality of classification as compared with to MLC, the forest has been 100 percent classified with the kappa value of 1. The classification for banana and water showed promising result with the kappa value of 0.7475 and 0.7665 (Table 17). The classification for bare land and bare land and grass were somewhat acceptable but the classification for pasture and regrowth proved to be of worst quality with pasture bearing the kappa value of 0.4463. The overall accuracy of 67.98 % was achieved for OOC via machine learning.

For OOC via machine learning for Forest and Other objects, the overall accuracy turned out to be 95.77% with overall kappa statistics value of 0.8041 (Table 17). But if judged according to the classification accuracy for individual objects, the classification for forest resulted only about 0.7018 kappa value which compared with the MLC proved to be of lower accuracy since the kappa value in case of MLC for forest was achieved to be 0.8995. From Table 16 and 17, it can be concluded that even though overall accuracy for OOC turned out to be less than optimal, the mapping of forest is possible using RADAR.

Therefore, with the analysis of accuracy assessment reports between supervised classification using MLC for Landsat 5 TM and OOC via machine learning for ALOS-1 PALSAR, optical sensor proved to have higher accuracy in mapping forest fragmentation in a tropical context.

5.9 Comparison of accuracies between optical and RADAR classified images

The classification of both optical and RADAR resulted in overall accuracies of 78.4% and 67.98% respectively. Table 18 illustrates the mapping accuracies for all the respective classes of Landsat and ALOS-1 PALSAR.

Table 18: Comparison of mapping accuracies for all classes

Classes	LANDSAT 5 TM Mapping Accuracy (%)	ALOS-1 PALSAR Mapping Accuracy (%)
Regrowth	54.81	26.62
Banana	57.75	49.1
Bare Land	64.66	44.3
Bare Land and Grass	78.2	60.46
Pasture	66	57.6
Old Forest	87.72	39.53
Water	89.47	78.1

As the accuracy assessment was performed, along with overall accuracy, mapping accuracy was also calculated for the sole reason to compare the accuracy of optical and RADAR methods to classify respective land cover classes. With the reference of Table 18, the highest mapping accuracy for Landsat was reflected in the classification of Water followed by Old Forest with the value of 89.47% and 87.72% respectively. Similarly for ALOS-1 PALSAR, the highest mapping accuracy was reflected in the classification of Water and Bare Land and Grass with the value of 78.1% and 60.46% respectively. There is a huge margin between the mapping accuracy of Old Forest between optical and RADAR. The reason behind low accuracy in RADAR is the use of FLS Image segmentation procedure as it is a combination of 6 different parameters with no fixed sets of values.

5.10 Limitations of the study

Even after the best efforts within the given time and available resources, the author still had to face the following limitations that has made impact on the overall outcome of the research. Such limitation should be minimized or eradicated in future research.

1. Spatial resolution

The low spatial resolution of 30m of Landsat-5 TM image resulted in a lot of mixed pixels during classification. This could be one of the reasons that caused the accuracy to be quite low. There has always been higher expectation from Landsat since it is a consistent data set for the study of land surface but the accuracy varies depending on the area of study and scope of the work. Higher resolution imageries from other commercial sensors such as Worldview, GeoEye, Ikonos etc. can be recommended, but they are relatively quite expensive.

2. Issue of clouds and haze

Due to the presence of cloud and haze, a masking effect over the images could be noticed in the images taken from Landsat-5 TM. This has led to small portions of the study area to be misclassified. Keeping this on mind, separate training samples had to be taken for the features under the effect of haze.

3. Inaccurate Ground Truth Data

Due to the decision in changing the year of the data acquisitions, a transition from a stronger set of ground truth data to a relatively lower accurate data had to be made. As the data was taken using a handheld GPS with a positional accuracy of approximately 3-10 metres, the data needed some editing which was done taking the field notes as a reference. Even after knowing the coordinates of the ground truth, the actual marks for various land-use / land cover was done in approximation since there was no availability of secondary source of data for year 2007 beside the field notes. This was unavoidable as the RADAR image for the year initially decided at the time of research inception could not be retrieved. This compromise has affected the classification process and the accuracy assessment part of the research. The fact that the Author has not physically been to the study area and ground truth information was the only reliable source of knowing what the actual landscape is, should not be underestimated.

4. Image Segmentation

    Image segmentation being a crucial operation for object orient classification, has a greater limitation. As there are no fixed sets of parameters for image segmentation to obtain optimum output, user has to perform hit and trail operation which may or may not provide better result since it depends on the radiometric properties of image pixels. There is no guarantee that the output of image segmentation is the most correct segmentation which makes it a rough estimator on how agreeable and disagreeable the segmentation actually is.

5. Issues with polarization

    As the RADAR image used during this research only had dual polarization of HH and HV. The major problem for the satellite RADAR is that it has only one dimension i.e. one frequency band or one or two polarizations These use of one dimensional operator cannot give adequate amount of information in order to accurately distinguish the ground feature at the time when the multi-temporal sensor are exploited. The lack of presence of full-polarization becomes a limitation to satellite RADAR.

CHAPTER SIX

CONCLUSION

This chapter concludes by returning to the research objectives mentioned in section 1.4 and continues by reviewing other important aspects that unveiled as the research proceeded. This chapter also discusses recommendations by the author for future references. The core emphasis is on the geospatial aspects of this research which was conducted under the motive of acquiring a master's degree in the field of Geospatial Information Science.

6.1 Research Aims:

This research helped to answer following research question:
Which sensor—optical or RADAR, can provide better mapping accuracy in mapping of tropical forest fragmentation?

The following objectives were proposed to achieve the research aim:
a. Analysing issues and complexity in using optical remote sensing for tropical forest fragmentation monitoring
b. Reviewing the feasibility of RADAR operations in tropical domains.
c. Performing image classification on both optical and RADAR imagery and comparing the classification accuracies between RADAR and optical classified imagery.

The overall aim and objectives of the research were met. Chapter 4 illustrates how the overall accuracy of optical imagery was superior to that of RADAR imagery in context of mapping forest fragmentation in a tropical context, despite the fact that mapping of forest fragmentation was also possible using RADAR. Chapter 5 discusses how the accuracy assessment helped answer the research question. In terms of the objectives, objectives a. was met through extensive literature review in order to identify the issues and complexity that arises in using optical remote sensing instruments. These issues were resolved using different mathematical corrections which were selected based on their capability to balance the reduction in overall issues as well as their ability to conserve image quality. The second objective was also met through carefully analysing the complexities involved in using a RADAR image to map forest fragmentation and trying to minimize the issues through the help of reviewing previous research works. Chapters 3 and 4 respectively contain the methods involved and

the outcome of performing image classification on both optical and RADAR imagery. Chapter 5 discussed the overall accuracies of both the classification methods with the help of ground truth data provided by Professor Andrew Millington.

After completion of this research, we can be certain that the mapping of forest fragmentation is possible with the help of remote sensing. The research confirms the potential of both optical and RADAR sensors for mapping tropical forest fragmentation with reasonably high levels of overall accuracy. The research also proves that object oriented classification applied to RADAR imagery is a suitable alternative to the use of optical imagery. The problem with optical system is the presence of cloud during image acquisition because of their shorter wavelengths and passive nature. The use of RADAR has always overcome this drawback of cloud coverage with their longer wavelength and higher penetrating strength. Besides resulting in considerate amount of overall accuracy, both the sensor have proved their worth in mapping tropical forest fragmentation with the overall accuracy of 98.79% and 95.77% with the kappa value of 0.918 and 0.8041 respectively for classifying Old Forest and other classes. The overall accuracy for optical sensor can be improved with the use of more accurate optical sensor and the data acquisition without cloud whereas for RADAR, the overall accuracy can be improved if the object based classification is performed using an alternative approach rather than FLS image segmentation.

6.2 Recommendations:

6.2.1 Spatial resolution of the imagery

The 30m Landsat pixel size for analysing forest fragmentation and for land use study can be viewed as a major reason for the substandard overall accuracy of the classifications. A much finer spatial resolution image could have potentially increased the overall classification accuracy for both the optical and RADAR imagery. Landsat being a 30 m resolution sensor, it is bound to have mixed pixel before even starting any processing. Higher spatial resolution bands help identifying features more quickly and more effectively which in term will increase the accuracy of image interpretation and image processing.

6.2.2 Spectral Resolution of the imagery

The six bands of Landsat-5 TM used in this research showed some issues regarding mixed spectral classes. Using images from sensors that give higher spectral resolution such as Sentinel, MODIS etc. could help solve this problem. Using Sentinel will also ensure that temporal and spatial resolutions are also higher. Clearly MODIS provides improved spectral and temporal resolutions but far poorer spatial

resolution. As the spatial resolution of Landsat is 30 metre, there are possibilities of having multiple features inside a single cell. As each feature reflect different spectral radiance, the combination of various signatures inside a single cell will surely result in the misinterpretation and misclassification of features.

6.2.3 Use of Multi band Synthetic Aperture Radar (SAR)

Multiple high frequency bands are used to balance bands of high range resolution with higher penetrating power with low frequency bands in multi band SAR (Domg and Milne, 2001). As optical system always had the problem with haze and clouds, the choice of RADAR for land use application is the ideal choice. The major problem for the satellite RADAR is that it has only one dimension i.e. one frequency band or one or two polarizations (Ali et al., 2008). These use of one dimensional operator cannot give adequate amount of information in order to accurately distinguish the ground feature at the time when the multi-temporal sensor are exploited (Evans et al., 2010). It is found that the use of both frequencies band; L and C are very effective for information extraction especially in the agricultural landscapes which can measure the finer detail of the data (Ali et al., 2008, Domg and Milne, 2001). So the combination of C band SAR (e.g. Sentinel 1) with L Band SAR (e.g. ALOS 2) may provide better discrimination in future work.

6.2.4 Alternate approach to Object-Oriented Classification

This research concluded that, the forest fragmentation can be mapped using satellite RADAR with some promising result besides having lesser overall accuracy to optical sensor. The accuracy of RADAR sensor can be increase if object oriented classification is performed applying alternatives techniques other than image segmentation as FLS image segmentation is a rather robust approach which does not always guarantee the accurate result. More accurate methods like Neural Network, Fuzzy Logic, AdaBoost etc. have proven to result in much accurate and smoother classification.

6.2.5 Combination of optical and RADAR data

Optical and RADAR both proved to be useful in mapping tropical forest fragmentation besides having different sets of algorithms for image processing. The result from both the sensors showed some quality result in classifying some features despite having relatively lower overall accuracies. Moreover, the result of these two distinct approaches can be combined together which might provide additional information to the study of features on the ground which seemed less likely through a single sensor alone. In order to combine these two methods, two condition should be fulfilled – 1. The acquisition

of images for both methods should be roughly on same point of time and 2. The images should be co-registered.

REFERENCES

ALI, S. M., JAVED, M. Y., KHATTAK, N. S. & MOHSIN, A. 2008. Despeckling of synthetic aperture radar images using inner product spaces in undecimated wavelet domain.

ALMEIDA-FILHO, R., ROSENQVIST, A., SHIMABUKURO, Y. E. & DOS SANTOS, J. R. 2005. Evaluation and perspectives of using multitemporal L-band SAR data to monitor deforestation in the Brazilian Amazo/spl circ/nia. *IEEE Geoscience and Remote Sensing Letters,* 2**,** 409-412.

BAMLER, R. 2000. Principles of synthetic aperture radar. *Surveys in Geophysics,* 21**,** 147-157.

BECK, L. R., LOBITZ, B. M. & WOOD, B. L. J. E. I. D. 2000. Remote sensing and human health: new sensors and new opportunities. 6**,** 217.

BENZ, U. C., HOFMANN, P., WILLHAUCK, G., LINGENFELDER, I., HEYNEN, M. J. I. J. O. P. & SENSING, R. 2004. Multi-resolution, object-oriented fuzzy analysis of remote sensing data for GIS-ready information. 58**,** 239-258.

BLASCHKE, T. J. I. J. O. P. & SENSING, R. 2010. Object based image analysis for remote sensing. 65**,** 2-16.

BONAN, G. B. 2008. Forests and climate change: forcings, feedbacks, and the climate benefits of forests. *science,* 320**,** 1444-1449.

COLLINGHAM, Y. C. & HUNTLEY, B. 2000. Impacts of habitat fragmentation and patch size upon migration rates. *Ecological Applications,* 10**,** 131-144.

CONGALTON, R. G. 1991a. A review of assessing the accuracy of classifications of remotely sensed data. *Remote sensing of environment,* 37**,** 35-46.

CONGALTON, R. G. & GREEN, K. 2008. *Assessing the accuracy of remotely sensed data: principles and practices*, CRC press.

CONGALTON, R. G. J. R. S. O. E. 1991b. A review of assessing the accuracy of classifications of remotely sensed data. 37**,** 35-46.

CORNFORTH, W. A., FATOYINBO, T. E., FREEMANTLE, T. P. & PETTORELLI, N. J. R. S. 2013. Advanced land observing satellite phased array type L-band SAR (ALOS PALSAR) to inform the conservation of mangroves: Sundarbans as a case study. 5**,** 224-237.

CRIST, E. P. & CICONE, R. C. 1984. A physically-based transformation of Thematic Mapper data---The TM Tasseled Cap. *IEEE Transactions on Geoscience and Remote sensing***,** 256-263.

DOMG, Y. & MILNE, A. K. 2001. Toward edge sharpening: a SAR speckle filtering algorithm. *IEEE Transactions on Geoscience and Remote Sensing,* 39**,** 851-863.

DONG, J., XIAO, X., SHELDON, S., BIRADAR, C., ZHANG, G., DUONG, N. D., HAZARIKA, M., WIKANTIKA, K., TAKEUHCI, W. & MOORE III, B. J. P. O. 2014. A 50-m forest cover map in Southeast Asia from ALOS/PALSAR and its application on forest fragmentation assessment. 9**,** e85801.

DONOGHUE, D. N. 2000. Remote sensing: Sensors and applications. *Progress in Physical Geography,* 24**,** 407-414.

DRUSCH, M., DEL BELLO, U., CARLIER, S., COLIN, O., FERNANDEZ, V., GASCON, F., HOERSCH, B., ISOLA, C., LABERINTI, P. & MARTIMORT, P. J. R. S. O. E. 2012. Sentinel-2: ESA's optical high-resolution mission for GMES operational services. 120**,** 25-36.

DU, Y., GUINDON, B. & CIHLAR, J. 2002. Haze detection and removal in high resolution satellite image with wavelet analysis. *IEEE Transactions on Geoscience and Remote Sensing,* 40**,** 210-217.

EVANS, T. L., COSTA, M., TELMER, K. & SILVA, T. S. 2010. Using ALOS/PALSAR and RADARSAT-2 to map land cover and seasonal inundation in the Brazilian Pantanal.

IEEE Journal of Selected Topics in Applied Earth Observations and Remote Sensing, 3**,** 560-575.

FAHRIG, L. 2003. Effects of habitat fragmentation on biodiversity. *Annual review of ecology, evolution, and systematics,* 34**,** 487-515.

FEARNSIDE, P. M. 2005. Deforestation in Brazilian Amazonia: history, rates, and consequences. *Conservation biology,* 19**,** 680-688.

FREEMAN, P. H. & FOX, R. 1994. *Satellite mapping of tropical forest cover and deforestation: A review with recommendations for USAID*, Environment and Natural Resources Information Center, DATEX Arlington, VA.

FROHN, R., AUTREY, B., LANE, C. & REIF, M. 2011. Segmentation and object-oriented classification of wetlands in a karst Florida landscape using multi-season Landsat-7 ETM+ imagery. *International Journal of Remote Sensing,* 32**,** 1471-1489.

FROST, V. S., STILES, J. A., SHANMUGAN, K. S. & HOLTZMAN, J. C. 1982. A model for radar images and its application to adaptive digital filtering of multiplicative noise. *IEEE Transactions on Pattern Analysis & Machine Intelligence***,** 157-166.

GAO, F., HILKER, T., ZHU, X., ANDERSON, M., MASEK, J., WANG, P., YANG, Y. J. I. G. & MAGAZINE, R. S. 2015. Fusing Landsat and MODIS data for vegetation monitoring. 3**,** 47-60.

GOETZ, S. J., BACCINI, A., LAPORTE, N. T., JOHNS, T., WALKER, W., KELLNDORFER, J., HOUGHTON, R. A. & SUN, M. 2009. Mapping and monitoring carbon stocks with satellite observations: a comparison of methods. *Carbon balance and management,* 4**,** 2.

HAILA, Y. 2002. A conceptual genealogy of fragmentation research: from island biogeography to landscape ecology. *Ecological applications,* 12**,** 321-334.

HANSEN, M. C., ROY, D. P., LINDQUIST, E., ADUSEI, B., JUSTICE, C. O. & ALTSTATT, A. 2008. A method for integrating MODIS and Landsat data for systematic monitoring of forest cover and change in the Congo Basin. *Remote Sensing of Environment,* 112**,** 2495-2513.

HOUGHTON, R., HALL, F. & GOETZ, S. J. 2009. Importance of biomass in the global carbon cycle. *Journal of Geophysical Research: Biogeosciences,* 114.

HOUGHTON, R. A. 1991. Tropical deforestation and atmospheric carbon dioxide. *Tropical Forests and Climate.* Springer.

HUANG, G., GUO, J., LV, J., XIAO, Z., ZHAO, Z. & QIU, C. Algorithms and experiment on SAR image orthorectification based on polynomial rectification and height displacement correction. Proceedings of Geo-Imagery Bridging Continents, XXth ISPRS Congress, Istanbul, 2004.

HYDE, P., DUBAYAH, R., WALKER, W., BLAIR, J. B., HOFTON, M. & HUNSAKER, C. 2006. Mapping forest structure for wildlife habitat analysis using multi-sensor (LiDAR, SAR/InSAR, ETM+, Quickbird) synergy. *Remote Sensing of Environment,* 102**,** 63-73.

IRONS, J. R., DWYER, J. L. & BARSI, J. A. 2012. The next Landsat satellite: The Landsat data continuity mission. *Remote Sensing of Environment,* 122**,** 11-21.

JENSEN, J. R. & LULLA, K. 1987. Introductory digital image processing: a remote sensing perspective.

JEZEK, K. C. J. A. O. G. 1999. Glaciological properties of the Antarctic ice sheet from RADARSAT-1 synthetic aperture radar imagery. 29**,** 286-290.

JHA, C., GOPARAJU, L., TRIPATHI, A., GHARAI, B., RAGHUBANSHI, A. & SINGH, J. 2005. Forest fragmentation and its impact on species diversity: an analysis using remote sensing and GIS. *Biodiversity & Conservation,* 14**,** 1681-1698.

JOSEPH, G. 2005. *Fundamentals of remote sensing*, Universities press.

KAUFMAN, Y. J. & SENDRA, C. 1988. Algorithm for automatic atmospheric corrections to visible and near-IR satellite imagery. *International Journal of Remote Sensing,* 9**,** 1357-1381.

KAUPPI, P. E., AUSUBEL, J. H., FANG, J., MATHER, A. S., SEDJO, R. A. & WAGGONER, P. E. 2006. Returning forests analyzed with the forest identity. *Proceedings of the National Academy of Sciences,* 103**,** 17574-17579.

KAUTH, R. J. & THOMAS, G. The tasselled cap--a graphic description of the spectral-temporal development of agricultural crops as seen by Landsat. LARS Symposia, 1976. 159.

KEENAN, R. J., REAMS, G. A., ACHARD, F., DE FREITAS, J. V., GRAINGER, A. & LINDQUIST, E. 2015. Dynamics of global forest area: Results from the FAO Global Forest Resources Assessment 2015. *Forest Ecology and Management,* 352**,** 9-20.

KONG, X., QIAN, Y. & ZHANG, A. Haze and cloud cover recognition and removal for serial Landsat images. MIPPR 2011: Remote Sensing Image Processing, Geographic Information Systems, and Other Applications, 2011. International Society for Optics and Photonics, 80061K.

LAMBIN, E. F. 1999. Monitoring forest degradation in tropical regions by remote sensing: some methodological issues. *Global ecology and biogeography,* 8**,** 191-198.

LANLY, J. 1981. Los recursos forestales de la America tropical. *FAO Informe Trcnico,* 1.

LAURANCE, W. F. & BIERREGAARD, R. O. 1997. *Tropical forest remnants: ecology, management, and conservation of fragmented communities*, University of Chicago Press.

LAURANCE, W. F., LAURANCE, S. G. & DELAMONICA, P. 1998. Tropical forest fragmentation and greenhouse gas emissions. *Forest Ecology and Management,* 110**,** 173-180.

LEE, J.-S. 1980. Digital image enhancement and noise filtering by use of local statistics. *IEEE Transactions on Pattern Analysis & Machine Intelligence*, 165-168.

LEE, J.-S. & POTTIER, E. 2009. *Polarimetric radar imaging: from basics to applications*, CRC press.

LIANG, S., FANG, H. & CHEN, M. 2001. Atmospheric correction of Landsat ETM+ land surface imagery. I. Methods. *IEEE Transactions on geoscience and remote sensing,* 39**,** 2490-2498.

LILLESAND, T., KIEFER, R. W. & CHIPMAN, J. 2014. *Remote sensing and image interpretation*, John Wiley & Sons.

LINDENMAYER, D. B. & FRANKLIN, J. F. 2002. *Conserving forest biodiversity: a comprehensive multiscaled approach*, Island press.

LIU, L. Z. J. S. J. & HENRIK, J. H. H. K. A Review: Remote Sensing Sensors.

LOPES, A., NEZRY, E., TOUZI, R. & LAUR, H. Maximum a posteriori speckle filtering and first order texture models in SAR images. Geoscience and Remote Sensing Symposium, 1990. IGARSS'90.'Remote Sensing Science for the Nineties'., 10th Annual International, 1990a. Ieee, 2409-2412.

LOPES, A., TOUZI, R. & NEZRY, E. 1990b. Adaptive speckle filters and scene heterogeneity. *IEEE transactions on Geoscience and Remote Sensing,* 28**,** 992-1000.

LOVELAND, T. R. & DWYER, J. L. 2012. Landsat: Building a strong future. *Remote Sensing of Environment,* 122**,** 22-29.

LU, D. & WENG, Q. 2007. A survey of image classification methods and techniques for improving classification performance. *International journal of Remote sensing,* 28**,** 823-870.

MAKARAU, A., RICHTER, R., MULLER, R. & REINARTZ, P. 2014. Haze detection and removal in remotely sensed multispectral imagery. *IEEE Transactions on Geoscience and Remote Sensing,* 52**,** 5895-5905.

MALINGREAU, J.-P. 1991. Remote sensing for tropical forest monitoring: an overview. *Remote Sensing and Geographic Information Systems for Resource Management in Developing Countries. Kluwer, Dordrecht/The Netherlands*.

MARGONO, B. A., TURUBANOVA, S., ZHURAVLEVA, I., POTAPOV, P., TYUKAVINA, A., BACCINI, A., GOETZ, S. & HANSEN, M. C. 2012. Mapping and monitoring
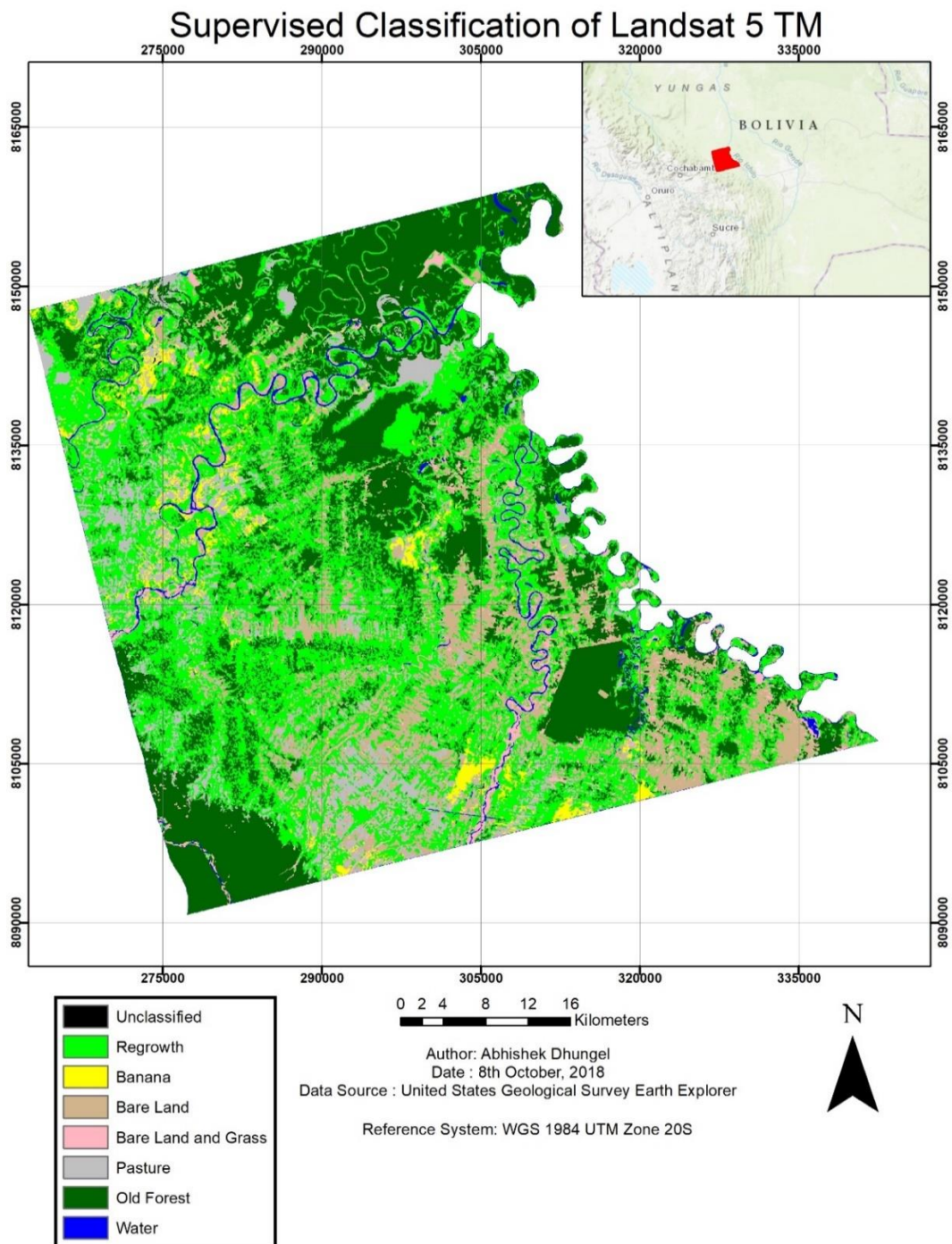
deforestation and forest degradation in Sumatra (Indonesia) using Landsat time series data sets from 1990 to 2010. *Environmental Research Letters,* 7**,** 034010.

MIETTINEN, J., SHI, C. & LIEW, S. C. 2011. Deforestation rates in insular Southeast Asia between 2000 and 2010. *Global Change Biology,* 17**,** 2261-2270.

MILLINGTON, A. C., VELEZ-LIENDO, X. M. & BRADLEY, A. V. 2003. Scale dependence in multitemporal mapping of forest fragmentation in Bolivia: implications for explaining temporal trends in landscape ecology and applications to biodiversity conservation. *ISPRS Journal of photogrammetry and remote sensing,* 57**,** 289-299.

MORALES, W. Q. J. T. W. B. E. O. R., ETHNICITY, & NATIONALISM 2015. Bolivia. 1-7.

MORANIEC, M. 2011. Landsat: An Earth-Observing Trailblazer. *ArticlesEarthObservationEarthzi ne, IEEE*.

MORO, G. D. & HALOUNOVA, L. 2007. Haze removal for high-resolution satellite data: a case study. *International Journal of Remote Sensing,* 28**,** 2187-2205.

MÜLLER, R., MÜLLER, D., SCHIERHORN, F. & GEROLD, G. 2011. Spatiotemporal modeling of the expansion of mechanized agriculture in the Bolivian lowland forests. *Applied Geography,* 31**,** 631-640.

MYERS, N., MITTERMEIER, R. A., MITTERMEIER, C. G., DA FONSECA, G. A. & KENT, J. 2000. Biodiversity hotspots for conservation priorities. *Nature,* 403**,** 853.

NOSS, R. F. & COOPERRIDER, A. 1994. *Saving nature's legacy: protecting and restoring biodiversity*, Island Press.

NOVACK, T., ESCH, T., KUX, H. & STILLA, U. 2011. Machine learning comparison between WorldView-2 and QuickBird-2-simulated imagery regarding object-based urban land cover classification. *remote sensing,* 3**,** 2263-2282.

OLIVER, C. & QUEGAN, S. 2004. *Understanding synthetic aperture radar images*, SciTech Publishing.

OLIVERA, O. & LEWIS, T. 2004. *Cochabamba!: water war in Bolivia*, South End Press.

PACHECO, P. 2002. Deforestation and forest degradation in lowland Bolivia. *Deforestation and land use in the Amazon***,** 66-94.

PACHECO, P. 2006. Agricultural expansion and deforestation in lowland Bolivia: the import substitution versus the structural adjustment model. *Land Use Policy,* 23**,** 205-225.

PHIRI, D. & MORGENROTH, J. 2017. Developments in Landsat land cover classification methods: A review. *Remote Sensing,* 9**,** 967.

POHL, C. & VAN GENDEREN, J. L. 1998. Review article multisensor image fusion in remote sensing: concepts, methods and applications. *International journal of remote sensing,* 19**,** 823-854.

RAUSTE, Y., LONNQVIST, A., MOLINIER, M., HENRY, J.-B. & HEME, T. Ortho-rectification and terrain correction of polarimetric SAR data applied in the ALOS/Palsar context. Geoscience and Remote Sensing Symposium, 2007. IGARSS 2007. IEEE International, 2007. IEEE, 1618-1621.

REES, W. G. & PELLIKA, P. 2010. Principles of remote sensing. *Remote Sensing of Glaciers. London*.

RICHARDS, J. A. 2013. Supervised classification techniques. *Remote Sensing Digital Image Analysis.* Springer.

ROSENQVIST, A., SHIMADA, M., ITO, N., WATANABE, M. J. I. T. O. G. & SENSING, R. 2007. ALOS PALSAR: A pathfinder mission for global-scale monitoring of the environment. 45, 3307-3316.

ROY, D. P., WULDER, M., LOVELAND, T. R., WOODCOCK, C., ALLEN, R., ANDERSON, M., HELDER, D., IRONS, J., JOHNSON, D. & KENNEDY, R. 2014. Landsat-8: Science and product vision for terrestrial global change research. *Remote sensing of Environment,* 145**,** 154-172.

ROY, P., BEHERA, M. & SRIVASTAV, S. 2017. Satellite Remote Sensing: Sensors, Applications and Techniques. Springer.

SAATCHI, S. S., SOARES, J. V. & ALVES, D. S. J. R. S. O. E. 1997. Mapping deforestation and land use in Amazon rainforest by using SIR-C imagery. 59, 191-202.

SAEVARSSON, B. B., SVEINSSON, J. R. & BENEDIKTSSON, J. A. Combined wavelet and curvelet denoising of SAR images. Geoscience and Remote Sensing Symposium, 2004. IGARSS'04. Proceedings. 2004 IEEE International, 2004. IEEE, 4235-4238.

SÁNCHEZ-AZOFEIFA, G. A., HARRISS, R. C. & SKOLE, D. L. 2001. Deforestation in Costa Rica: a quantitative analysis using remote sensing imagery 1. *Biotropica,* 33**,** 378-384.

SHEN, H., LI, H., QIAN, Y., ZHANG, L. & YUAN, Q. 2014. An effective thin cloud removal procedure for visible remote sensing images. *ISPRS Journal of Photogrammetry and Remote Sensing,* 96**,** 224-235.

SHIMADA, M., ISOGUCHI, O., TADONO, T. & ISONO, K. 2009. PALSAR radiometric and geometric calibration. *IEEE Transactions on Geoscience and Remote Sensing,* 47**,** 3915-3932.

SHORT, N. M. 1976. Mission to Earth: Landsat Views the World.

SIEGERT, F. & HOFFMANN, A. A. 2000. The 1998 forest fires in East Kalimantan (Indonesia): a quantitative evaluation using high resolution, multitemporal ERS-2 SAR images and NOAA-AVHRR hotspot data. *Remote Sensing of Environment,* 72**,** 64-77.

SKOLE, D. & TUCKER, C. 1993. Tropical deforestation and habitat fragmentation in the Amazon: satellite data from 1978 to 1988. *Science,* 260**,** 1905-1910.

STEARMAN, A. M. 1985. *Camba and Kolla: migration and development in Santa Cruz, Bolivia*, University Press of Florida.

STEININGER, M. K., TUCKER, C. J., TOWNSHEND, J. R., KILLEEN, T. J., DESCH, A., BELL, V. & ERSTS, P. 2001. Tropical deforestation in the Bolivian Amazon. *Environmental conservation,* 28**,** 127-134.

SUMANTYO, J. T. S. & AMINI, J. 2008. A model for removal of speckle noise in SAR images (ALOS PALSAR). *Canadian Journal of Remote Sensing,* 34**,** 503-515.

TAUBERT, F., FISCHER, R., GROENEVELD, J., LEHMANN, S., MÜLLER, M. S., RÖDIG, E., WIEGAND, T. & HUTH, A. 2018. Global patterns of tropical forest fragmentation. *Nature,* 554**,** 519.

TEJADA, G., DALLA-NORA, E., CORDOBA, D., LAFORTEZZA, R., OVANDO, A., ASSIS, T. & AGUIAR, A. P. 2016. Deforestation scenarios for the Bolivian lowlands. *Environmental research,* 144**,** 49-63.

TOUTIN, T. 2004. Geometric processing of remote sensing images: models, algorithms and methods. *International journal of remote sensing,* 25**,** 1893-1924.

TUCKER, R. P. & RICHARDS, J. F. 1983. Global deforestation and the nineteenth-century world economy.

WALTER, V. J. I. J. O. P. & SENSING, R. 2004. Object-based classification of remote sensing data for change detection. 58**,** 225-238.

WATCH, G. F. 2002. Global forest watch. *World Resources Institute, Washington, DC Available from http://www. globalforestwatch. org (accessed March 2002)*.

WILCOVE, D. S., MCLELLAN, C. H. & DOBSON, A. P. 1986. Habitat fragmentation in the temperate zone. *Conservation biology,* 6**,** 237-256.

WILLIAMS, D. L., GOWARD, S. & ARVIDSON, T. 2006. Landsat. *Photogrammetric Engineering & Remote Sensing,* 72**,** 1171-1178.

WILLIAMS, M. 2000. Dark ages and dark areas: global deforestation in the deep past. *Journal of historical geography,* 26**,** 28-46.

YAACOBI, G., ZIV, Y. & ROSENZWEIG, M. L. 2007. Habitat fragmentation may not matter to species diversity. *Proceedings of the Royal Society of London B: Biological Sciences,* 274**,** 2409-2412.

ZERROUKI, N. & BOUCHAFFRA, D. Pixel-based or Object-based: Which approach is more appropriate for remote sensing image classification? Systems, Man and Cybernetics (SMC), 2014 IEEE International Conference on, 2014. IEEE, 864-869.

ZHANG, G., LI, Z., ZHU, X. & FEI, W. 2013. Geometric model for high-resolution SAR-GEC images. *International Journal of Image and Data Fusion,* 4**,** 159-170.
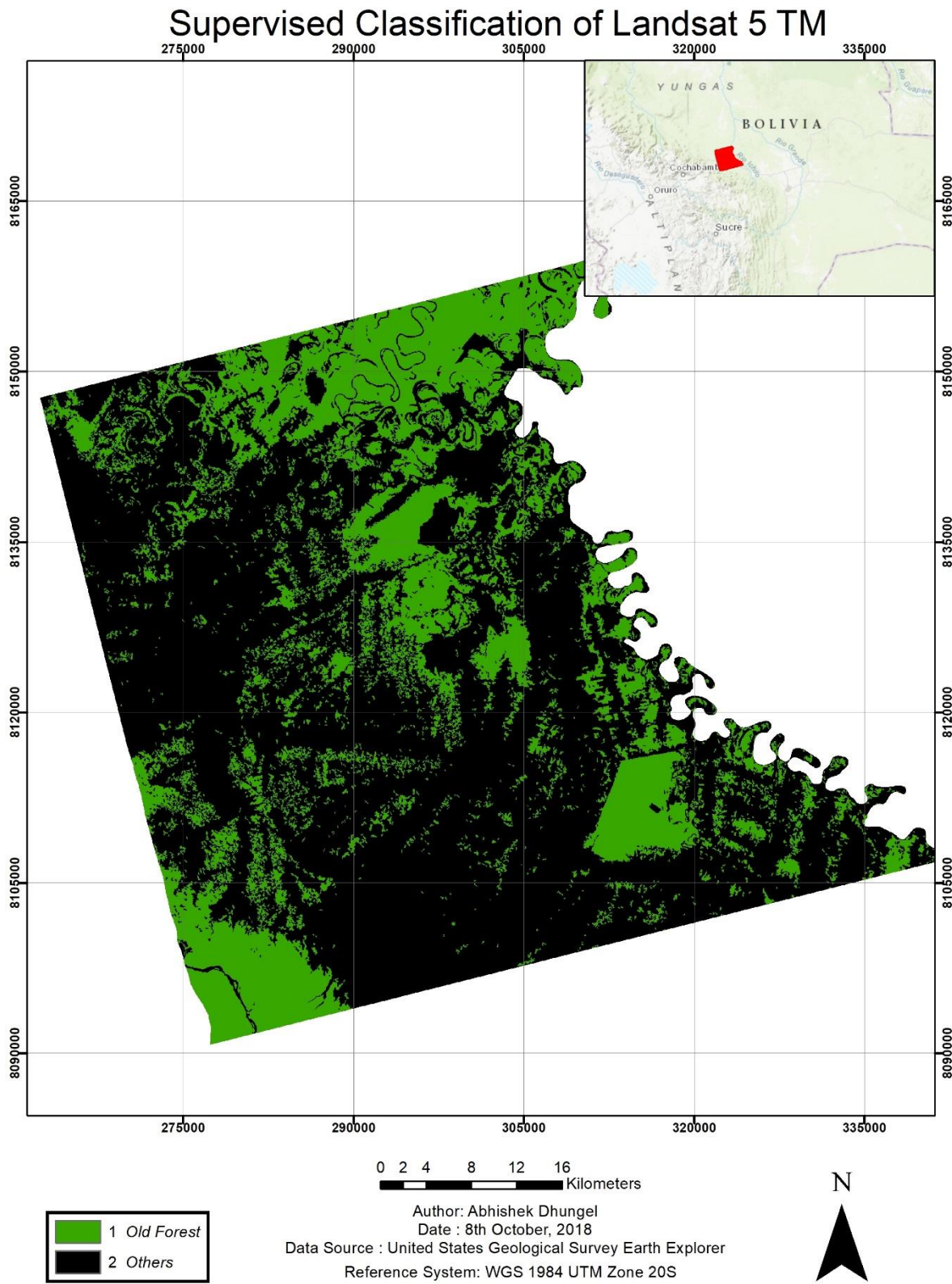
ZHANG, Y., GUINDON, B. & CIHLAR, J. 2002. An image transform to characterize and compensate for spatial variations in thin cloud contamination of Landsat images. *Remote Sensing of Environment,* 82**,** 173-187.

APPENDICES

Appendix (a): Map of Supervised Classification of Landsat 5 TM for all 7 signature classes

Supervised Classification of Landsat 5 TM

Legend:
- Unclassified
- Regrowth
- Banana
- Bare Land
- Bare Land and Grass
- Pasture
- Old Forest
- Water

0 2 4 8 12 16 Kilometers

N

Author: Abhishek Dhungel
Date : 8th October, 2018
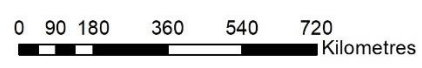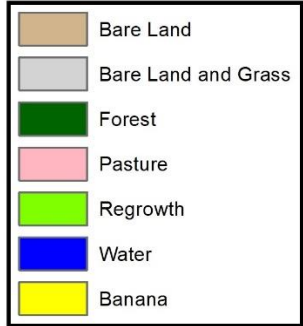Data Source : United States Geological Survey Earth Explorer

Reference System: WGS 1984 UTM Zone 20S

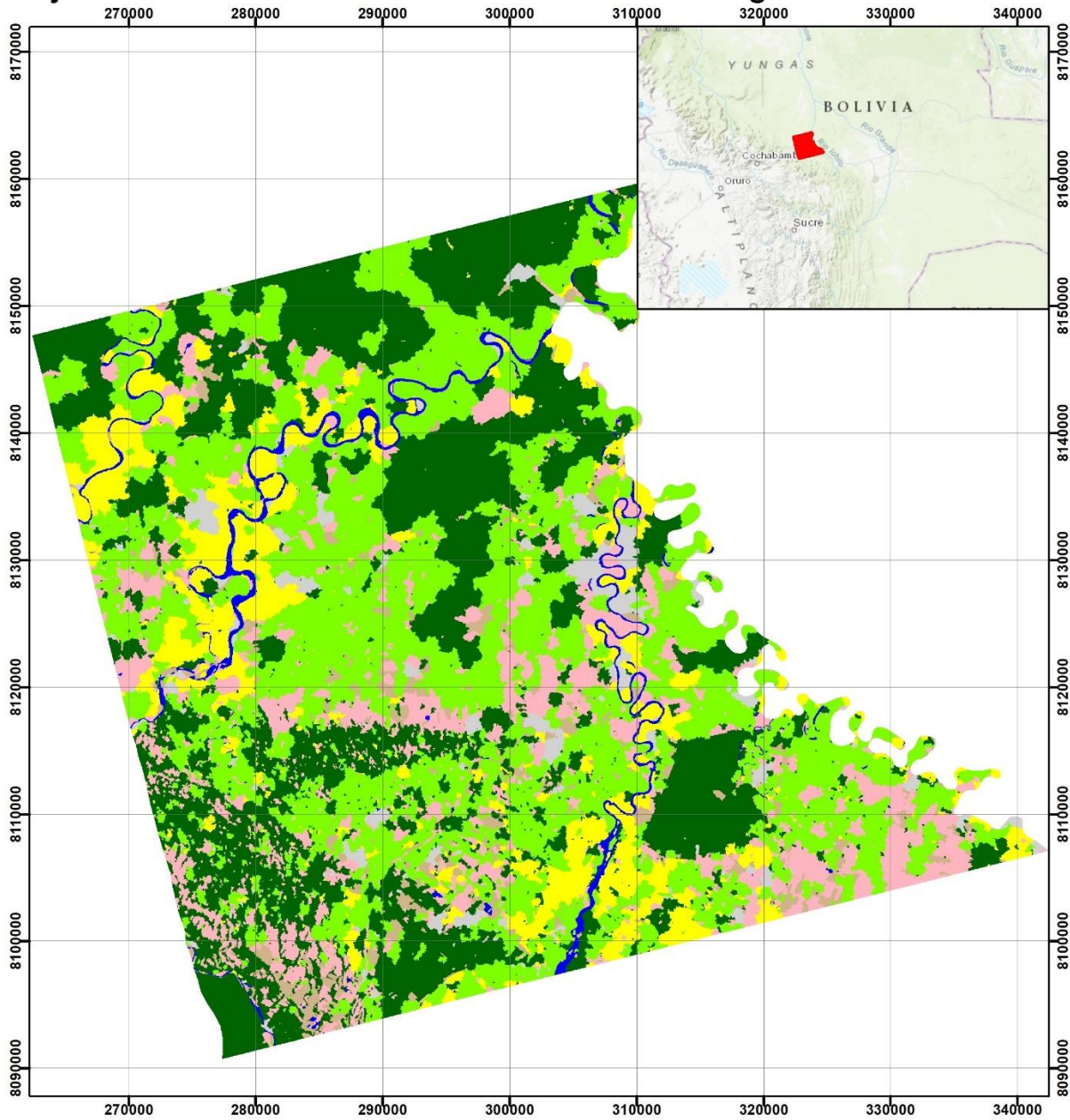**Appendix (b): Map of Supervised Classification of Landsat 5 TM for 2 classes (Old Forest and Others)**

Supervised Classification of Landsat 5 TM

1 Old Forest
2 Others

0 2 4 8 12 16 Kilometers

Author: Abhishek Dhungel
Date : 8th October, 2018
Data Source : United States Geological Survey Earth Explorer
Reference System: WGS 1984 UTM Zone 20S

N

Appendix (c): Map of Object-Oriented Classification of ALOS-1 PALSAR for all 7 classes

Object Oriented Classification via Machine Learning for ALOS-1 PALSAR

Legend:
- Bare Land
- Bare Land and Grass
- Forest
- Pasture
- Regrowth
- Water
- Banana

0 90 180   360   540   720
Kilometres

Author: Abhishek Dhungel
Date : 8th October, 2018
Data Source : Alaskan Satellite Facility
Reference System: WGS 1984 UTM Zone 20S

N

Appendix (d): Map of Object-Oriented Classification of ALOS-1 PALSAR for only 2 classes (Old Forest and Others)

Object Oriented Classification via Machine Learning for ALOS-1 PALSAR

Unclassified
Others
Old Forest

0 85 170   340   510   680
Kilometres

Author: Abhishek Dhungel
Date : 8th October, 2018
Data Source: Alaskan Satellite Facility
Reference System: WGS 1984 UTM Zone 20S

N